

Magnetohydrodynamic Instabilities in Shearing, Rotating, Stratified Winds and Disks

Woong-Tae Kim and Eve C. Ostriker

Department of Astronomy, University of Maryland, College Park, MD 20742

kimwt@astro.umd.edu, ostriker@astro.umd.edu

ABSTRACT

We investigate shear and buoyancy instabilities in radially stratified, magnetized, cylindrical flows, for application to magnetocentrifugally driven winds - such as those from protostars - and to magnetized accretion disks. Our motivation is to characterize the susceptibility of cold MHD disk winds to growing internal perturbations, and to understand the relation of wind instabilities to known accretion disk instabilities. Using four different linear analysis techniques, we identify and study nine principal types of unstable or overstable disturbances, providing numerical and analytic solutions for growth rates for a wide range of parameters.

When magnetic fields are predominantly *toroidal*, as in protostellar winds far from their source, we find the system is susceptible to growth of five different kinds of perturbations: axisymmetric fundamental and toroidal resonance modes, axisymmetric and non-axisymmetric toroidal buoyancy modes, and non-axisymmetric magnetorotational modes. Winds having a sufficiently steep field gradient ($d \ln B / d \ln R < -0.75$ for a purely toroidal-field case) are globally unstable to the long wavelength fundamental mode concentrated at small radii; these promote the establishment of narrow dense jets in the centers of wider winds. Long-wavelength outer-wind modes are all stable for power-law wind equilibria. The toroidal buoyancy instabilities promote small-scale radial mixing provided the equilibrium has nonzero magnetic forces. For low-temperature toroidal- \mathbf{B} winds, both axisymmetric and non-axisymmetric magnetorotational instabilities have very low growth rates. The stabilization of buoyancy instabilities by shear and of magnetorotational instabilities by compressibility may be important in allowing cold MHD winds to propagate over vast distances in space.

When magnetic fields are predominantly *poloidal*, as may occur in protostellar winds close to their source or in astrophysical disks, we find the system is susceptible to four additional growing modes: axisymmetric magnetorotational (Balbus-Hawley), axisymmetric poloidal buoyancy, non-axisymmetric geometric buoyancy, and poloidal resonance modes. The well-known axisymmetric Balbus-Hawley mode has the fastest

growth rate. When the magnetic field is nonuniform, the axisymmetric poloidal buoyancy mode promotes radial mixing on small scales. The geometric poloidal buoyancy mode requires high m , thus is readily stabilized by shear.

Previous work on magnetorotational instabilities has concentrated on near-incompressible systems (accretion disks or stellar interiors). We extend this analysis to allow for compressibility (important in winds). We introduce a “coherent wavelet” technique (a WKB temporal approximation), and derive closed-form analytic expressions for instantaneous instability criteria, growth rates, and net amplification factors for generalized non-axisymmetric magnetorotational instabilities in compressible flows with both poloidal and toroidal fields. We confirm that these are in excellent agreement with the results of shearing-sheet temporal integrations, and that “locally-axisymmetric” perturbations have the largest amplifications only provided $(\mathbf{k} \cdot \mathbf{v}_A)/\Omega \lesssim 1$.

Subject headings: accretion, accretion disks — ISM: dynamics — ISM: jets and outflows — ISM: magnetic fields — MHD — stars: pre-main-sequence

1. Introduction

The ubiquity of energetic molecular outflows and atomic jets from young stellar objects (YSOs) ranging from deeply embedded infrared sources to classical T Tauri stars suggests that they are an inescapable by-product of star formation (e.g., Richer et al. 2000, and references therein). Winds from YSO disks play an important role in shedding angular momentum carried by inflowing material, thereby permitting further accretion in order for the central objects to attain stellar dimensions (Hartmann & MacGregor 1982; Pudritz & Norman 1986; Shu et al. 1988). These winds may also have strong effects on the dynamical evolution of the parent cloud by providing a source of turbulent energy (Norman & Silk 1980), and may help to determine the final masses of stars by reversing the infall of surrounding gas (Shu, Adams, & Lizano 1987). Therefore, understanding the physics of protostellar winds is of essential importance to the theory of star formation.

Among the various scenarios regarding the origin and nature of the protostellar winds, the most promising is magnetohydrodynamic (MHD) models in which winds are driven by the interaction of the centrifugal force with open magnetic fields threading rapidly rotating disks. These magnetocentrifugally driven wind models can account for observed high mass and momentum losses (Lada 1985; Bachiller 1996) and the kinematic and structural characteristics of bipolar molecular outflows in general (Li & Shu 1996), as well as in specific cases (e.g., HH111, cf. Nagar et al. 1997). It is, however, still controversial whether the wind originates only from a small magnetosphere-disk interaction region near the central star (Shu et al. 1994, 2000), or whether it emanates from an extended region of the disk (following the seminal model of Blandford & Payne 1982; see, e.g., Königl & Pudritz 2000).

Although the role of magnetic fields in driving protostellar winds is by now well established

(at least theoretically), their complementary role in governing the stability properties of winds is less well explored. In addition, azimuthal and vertical shear within winds may also affect their stability properties. Questions of wind stability are potentially important for both large scale and small-scale phenomena. These include understanding the role of magnetic fields and velocity shear in (a) helping winds to propagate over enormous distances (up to a factor $\sim 10^6$ in dynamic range) through the ISM in parsec-scale giant HH flows (Reipurth, Bally, & Devine 1997); (b) creating bright HH “knots” spaced throughout optical jets (Hartigan et al. 2000); (c) governing the angular extent of the emergent wind and establishing the momentum distribution for driving molecular outflows; and (d) converting large-scale ordered flow energy to jet heating through small-scale instabilities. In addition, it is important to study the dynamical properties of large classes of theoretical wind solutions to test whether they are stable equilibria which can represent real astronomical systems, or whether they are unstable equilibria which should rarely be observed in nature because they evolve rapidly into other configurations.

Previous studies of time-dependent behavior in steadily-input MHD winds have focussed primarily on the Kelvin-Helmholtz instabilities driven by the interaction of the wind surface layer with the ambient medium (see, e.g., the studies of Appl & Camenzind 1992; Hardee et al. 1992; Rosen et al. 1999, and references therein). Generally, heavy jets containing strong toroidal fields are relatively resistant to these instabilities. In addition to “driven” instabilities resulting from boundary conditions, winds may also be subject to “free” instabilities in their interiors. Whether a given wind solution is internally unstable must depend on the velocity shear, magnetic geometry, and internal stratification. One route to studying internal wind instabilities is via time-dependent numerical simulations of winds. Although such studies (e.g., Ouyed & Pudritz 1997, and references therein) have yielded intriguing results on the development of episodic knots in MHD winds, the computational demands in carrying out simulations precludes extensive exploration of parameter space, large spatial dynamic range, or very long-term integration. In addition, some of the time-dependent internal features found in simulations may be introduced by particular choices of inflow boundary conditions that are inconsistent with a steady-state flow, rather than occurring as a result of intrinsic instability of the wind.

Due to the importance of gaseous accretion disks in a wide variety of astrophysical systems, major attention has focussed on disk dynamics, and, in particular, the role of instability-driven turbulence in angular momentum transport (see, e.g., Balbus & Hawley 1998; Stone et al. 2000, for reviews). Saturated magnetorotational instabilities (hereafter MRIs; Balbus & Hawley 1991, 1992; Hawley & Balbus 1991; Hawley, Gammie, & Balbus 1995) represent perhaps the most important local dynamical process affecting disk evolution. Magnetized disk winds share many generic properties with disks, so it is interesting to investigate the potential importance of MRIs in winds.

In this work, we investigate the internal stability of rotating, magnetized protostellar winds to (primarily) local shear and buoyancy modes. We also extend previous studies of local MRIs in accretion disks. The fundamental difference between “wind” and “disk” systems in our idealized models is in the absence or presence of gravity as a confining force. These systems may also be

distinguished by the geometry of the magnetic field, with toroidally-dominant fields expected in the wind case, but either poloidal or toroidal fields possible for the disk case. Our most general analysis and results apply to cold flows, but we also perform separate calculations (see §7) including thermal effects which specialize to local analysis of MRIs.

Whether a wind originates from a narrow boundary layer or an extended radial region, the radial expansion of the flow will lead to shear in the azimuthal velocity field of the asymptotic state. The total specific angular momentum of the flow, $J = R(v_\phi - B_{\text{pol}}B_\phi/(4\pi\rho v_{\text{pol}}))$, is conserved along streamlines (where B_{pol} , B_ϕ and v_{pol} , v_ϕ are the poloidal, toroidal components of the magnetic field and the flow velocity). If the Alfvén mach number $M_A \equiv v_{\text{pol}}/v_{A,\text{pol}} \gg 1$, the kinetic part dominates the specific angular momentum and $v_\phi \approx J/R$. Thus, the angular velocity $\Omega = v_\phi/R \approx J/R^2$ in the asymptotic wind will have a gradient $d\ln\Omega/d\ln R = d\ln J/d\ln R - 2$. If the wind comes from a boundary layer, then $d\ln J/d\ln R$ may be small; if the wind originates from a large region with self-similar scalings, then $d\ln J/d\ln R = 1/2$. In either case, $d\ln\Omega/d\ln R$ is expected to be a negative, order-unity quantity for wind systems. For thin disk systems (i.e., negligible pressure support), a Keplerian radial profile $d\ln\Omega/d\ln R = -3/2$ is expected if the central mass is dominant. For the analysis of this paper (except where noted otherwise), we adopt $d\ln\Omega/d\ln R = -3/2$ for both “wind” and “disk” systems, but our qualitative results are insensitive to this assumption. As discussed below, order-unity radial logarithmic gradients may also be expected in the magnetic field strengths; we allow for a range of magnetic gradients.

Significant shear may also exist in the poloidal velocities of jets if they originate from an extended radial region. The asymptotic outflow speed v_{0z} generally scales linearly with the rotational speed at the footpoint R_{foot} of the streamline, so that

$$\frac{\partial \ln v_{0z}}{\partial \ln R} = \frac{\partial \ln v_{0z}}{\partial \ln v_{\text{foot}}} \frac{\partial \ln v_{\text{foot}}}{\partial \ln R_{\text{foot}}} \frac{\partial \ln R_{\text{foot}}}{\partial \ln R} \sim -\frac{1}{2} \frac{\partial \ln R_{\text{foot}}}{\partial \ln R}.$$

If the range of footpoint radii is small compared to the range of asymptotic radii (as for a wind from a boundary layer), then $|\partial \ln v_{0z}/\partial \ln R| \ll 1$; if the radial ranges are comparable, then $\partial \ln v_{0z}/\partial \ln R$ is negative and order unity. For disks, the vertical velocity shear is negligible. We allow for a range of vertical shear rates in the present analysis.

Our analysis consists of developing and solving sets of linearized MHD equations for several general classes of background flows. Both axisymmetric and non-axisymmetric disturbances are explored. Even in linearized form, MHD problems present considerable technical challenges. Thus, instead of attacking sophisticated sets of steady-state wind solutions, for many specific examples we will take as an unperturbed configuration one of the power-law cylindrical equilibrium solutions recently identified by Ostriker (1997) as asymptotic states of self-similar disk winds. These have density $\rho \propto R^{-q}$, $\mathbf{B} \propto R^{-(1+q)/2}$, $\mathbf{v} \propto R^{-1/2}$, and sound speed $c_s = 0$. Although these adopted initial configurations are relatively simple, they retain general asymptotic characteristics of MHD disk winds in the sense that they have both azimuthal and vertical magnetic field and velocity components with arbitrary ratios, and all the physical variables have radial gradients. These gradients may also be thought of as representing local scalings within a more complex overall

stratification. We also include models without vertical motion but with significant equilibrium gravity to study stability in magnetized astrophysical disks. In our analysis of MRIs, we use equilibria with uniform \mathbf{B} , ρ , and $c_s \neq 0$, and take $\Omega \propto R^{-a}$ with arbitrary a .

Because the systems we are studying contain significant azimuthal shear, an arbitrary initial spatial planform is not maintained indefinitely. When $\Omega' \neq 0$ and the azimuthal wavenumber $m \neq 0$ (and/or when $v'_{0z} \neq 0$ and the vertical wavenumber $k_z \neq 0$; the prime represents a differentiation with respect to R), spatial wavefunctions may become increasingly radially corrugated in time due to the kinematic shearing of the wavefronts imposed in the initial conditions. If we describe the radial spatial wavefunction in terms of the amplitudes of Fourier coefficients with radial wavenumbers k_R , this corresponds at late times to a secular increase in the amplitudes of large- k_R terms and decrease in the amplitudes of small- k_R terms. As we shall show, all the disturbances we identify are stabilized at sufficiently large k_R . Thus, if $m\Omega'$ and/or $k_z v'_{0z} \neq 0$, the net amplification factor for any arbitrary initial disturbance is limited by the rate of kinematic growth of radial corrugation compared to the growth rate of any dynamically-driven instabilities.

In previous work, two complementary analytical methods have been used to study small-amplitude disturbances in shearing astrophysical systems. One approach adopts the “shearing-sheet” formalism, and integrates the local, time-dependent, linearized wave equations directly to obtain the evolutionary behavior of shearing wavelets treated as an initial-value problem (Goldreich & Lynden-Bell 1965; Julian & Toomre 1966; Balbus & Hawley 1992). An alternative analytical approach uses WKB techniques to derive dispersion relations for spatial Fourier modes, superpositions of which represent local wavefunctions (e.g., Shu 1974, 1992; Ryu & Goodman 1992; Terquem & Papaloizou 1996). This paper includes analyses using both approaches, and also introduces a hybrid technique which we term a “coherent wavelet” analysis. We adopt the “modal” strategy in order to identify characteristic instantaneous growth rates and physical mechanisms for a wide variety of spatial disturbances. By considering the time over which a spatial pattern is altered by shear, we can estimate the net amplification factor of a given initial modal disturbance. We use the shearing-sheet formalism for studying magnetorotational instabilities, which are cut off at relatively small values of Rk_R/m (whereas the modal analysis applies to large Rk_R/m), and also for studying buoyancy instabilities in the high- m regime where modes are short-lived. We show that the results obtained from the shearing-sheet integrations in both cases are in excellent agreement with the predictions of a coherent wavelet analysis, in which time-dependent growth rates $\gamma(t)$ are computed by time-localizing the shearing-sheet equations and solving an analytic dispersion relation.

The organization of this paper is as follows: We begin by studying instabilities in cold, magnetized winds. In §2, the basic MHD equations and the specific adopted wind equilibria are described. In §3, we analyze the stability of winds to the simplest perturbation with $k_z = m = 0$, where k_z and m are respectively the vertical and azimuthal wavenumbers of the perturbation. We term these the “fundamental modes”; we present solutions for stable and unstable global modes under the assumption of free Lagrangian boundary conditions. The modal analysis and general local dispersion

relation for cold flows with arbitrary k_z and m are presented in §4. We present numerical solutions of the dispersion relation for both axisymmetric and non-axisymmetric perturbations in §5. In §6, we classify the unstable or overstable modes and provide the physical interpretation for each mode. Next, we include (variable) thermal pressure terms to compare the susceptibility of cold winds vs. warm disks to shear instabilities. In §7 we analyze the axisymmetric Balbus-Hawley instability of poloidal fields and the non-axisymmetric MRI of toroidal fields, discuss the respective instability mechanisms, and provide the corresponding instability criteria. Here, we use the coherent wavelet technique to compute growth rates, and compare with direct shearing-sheet integrations. The generalized instability criteria and net amplification factors for the magnetorotational disturbances with both toroidal and poloidal background fields are also derived. Finally in §8, we summarize and discuss conclusions of the present work.

2. Basic Equations and Cylindrical Equilibrium for Cold Wind

We begin with the ideal MHD equations

$$\frac{\partial \rho}{\partial t} + \nabla \cdot (\rho \mathbf{v}) = 0, \quad (1)$$

$$\frac{\partial \mathbf{v}}{\partial t} + \mathbf{v} \cdot \nabla \mathbf{v} = \frac{1}{4\pi\rho} (\nabla \times \mathbf{B}) \times \mathbf{B} - \frac{\nabla P}{\rho} - \nabla \Phi_G, \quad (2)$$

$$\frac{\partial \mathbf{B}}{\partial t} = \nabla \times (\mathbf{v} \times \mathbf{B}), \quad (3)$$

and

$$\nabla \cdot \mathbf{B} = 0, \quad (4)$$

where ρ is the density, \mathbf{v} is the fluid velocity, \mathbf{B} is the magnetic field, P is the thermal pressure, and $-\nabla \Phi_G \equiv -\mathbf{g}$ is the gravitational force due to a central object. We ignore self-gravity in the flow.

We now consider cold, magnetized cylindrical flows. Since the flow velocity in disk winds is always supersonic except in the vicinity of the disk where the material is lifted by the thermal pressure (Blandford & Payne 1982), the thermal pressure term in eq. (2) can generally be neglected compared to magnetic stress. Except for investigations of generalized MRIs (§7), we shall drop the thermal pressure term. We adopt standard cylindrical coordinates (R, ϕ, z) .

By assuming that $v_R = B_R = 0$ and all variables are independent of z , we have a general equilibrium condition from eq. (2)

$$\Omega^2 R \equiv \frac{v_\phi^2}{R} = \frac{1}{4\pi\rho} \left(\frac{B_\phi^2}{R} + \mathbf{B} \cdot \mathbf{B}' \right) + g_R, \quad (5)$$

where a prime denotes differentiation with respect to R . At a large distance from the origin, the gravitational force due to the central source can also be ignored on the grounds that magnetic and

centrifugal forces far exceed it. In this case, the magnetic hoop stress acting inward is the only force that balances the outward centrifugal force and outward magnetic pressure gradient force (under the assumption that the magnetic field strength decreases outward).

As an initial equilibrium configuration of the wind, for specific cases we will adopt the asymptotic solutions for cylindrically symmetric axial flows presented by Ostriker (1997). All variables have power-law dependences on R : $\rho \propto R^{-q}$, $B_\phi \propto B_z \propto R^{-(1+q)/2}$, and $v_\phi \propto v_z \propto R^{-1/2}$. We define the local pitch angle i of the magnetic fields as $i \equiv \tan^{-1}(B_z/B_\phi)$. Neglecting g_R in eq. (5), radial momentum balance requires

$$v_\phi^2 = \frac{v_A^2}{2} (\cos 2i - q), \quad (6)$$

where v_A is the local Alfvén speed defined by

$$v_A^2 \equiv v_{A\phi}^2 + v_{Az}^2 \quad \text{with} \quad v_{A\phi} \equiv \frac{B_\phi}{\sqrt{4\pi\rho}} \quad \text{and} \quad v_{Az} \equiv \frac{B_z}{\sqrt{4\pi\rho}}.$$

It is obvious from eq. (6) that there would be no such power-law solutions if $q > 1$. This is because when $q > 1$, the magnetic field has so steep a gradient that the corresponding pressure force always exceeds the tension. Therefore, to ensure force balance and cylindrical collimation in winds with power-law profiles, the magnetic field strength must decline with R more slowly than R^{-1} .

We can define an angular velocity $\Omega_f \equiv \Omega - v_{\text{pol}}B_\phi/(RB_{\text{pol}})$ as that of a rotating frame in which the flow of winds is parallel to the local field line. Ω_f is the rotation rate of the magnetic field lines thought of as rigid wires. In such a frame, the family of solutions can be completely described in terms of scaled values of the specific angular momentum j , the Bernoulli constant e , and q , where

$$j \equiv \frac{\Omega}{\Omega_f} \left(1 - \frac{(v_{A\phi}/R\Omega)^2}{1 - \Omega_f/\Omega} \right) \quad \text{and} \quad e \equiv \frac{1}{(R\Omega_f)^2} \left(\frac{1}{2} \mathbf{v}^2 + \Phi_G - R^2 \Omega_f \Omega \right),$$

(Ostriker 1997). The condition for a super-Alfvénic outflow velocity requires $0 < j \leq 1$. Generally speaking, the pitch angle i does not depend on q , although one can parameterize i in terms of q , e , and j . However, for flows originating from a Kepler-rotating disk, angular momentum and energy conservation requirements limit the range of i available to an equilibrium (asymptotic) magnetic field configuration. Utilizing eqs. (15) to (23) of Ostriker (1997) one can show that the maximum, over all permitted values of e and j , pitch angle i_{max} is given by

$$\tan^2 i_{\text{max}} = \left(\frac{4}{3+q} \right)^2 - 1, \quad (7)$$

which is attained when $e = 0$ and $j = 1$. If $j > 1$, the streamline never reaches the Alfvén radius.

3. Fundamental Mode

3.1. Dynamical Equations

We first consider the response of the equilibrium state when small, axisymmetric perturbations with an infinite wavelength along a vertical direction are imposed. We term the waves with $k_z = 0$ and $m = 0$ the “fundamental modes” analogous to eigenfunctions of oscillations without any node. Let the subscripts 0 and 1 denote the equilibrium and perturbed states, respectively. Linearizing the set of the dynamical equations (1) to (4), we may write

$$\frac{\partial \rho_1}{\partial t} = -\frac{1}{R} \frac{\partial}{\partial R} (R \rho_0 v_{1R}), \quad (8)$$

$$\frac{\partial v_{1R}}{\partial t} = 2\Omega v_{1\phi} - \frac{1}{4\pi\rho_0} \left\{ \frac{2B_{0\phi}B_{1\phi}}{R} + \frac{\partial}{\partial R} (\mathbf{B}_0 \cdot \mathbf{B}_1) - \frac{\rho_1}{\rho_0} \left(\frac{B_{0\phi}^2}{R} + \mathbf{B}_0 \cdot \mathbf{B}'_0 \right) \right\}, \quad (9)$$

$$\frac{\partial v_{1\phi}}{\partial t} = -\frac{\kappa^2}{2\Omega} v_{1R}, \quad (10)$$

$$\frac{\partial v_{1z}}{\partial t} = -v'_{0z} v_{1R}, \quad (11)$$

$$\frac{\partial B_{1\phi}}{\partial t} = -\frac{\partial}{\partial R} (B_{0\phi} v_{1R}), \quad (12)$$

$$\frac{\partial B_{1z}}{\partial t} = -\frac{1}{R} \frac{\partial}{\partial R} (R B_{0z} v_{1R}), \quad (13)$$

and $B_{1R} = 0$. In eq. (10), κ stands for the epicycle frequency

$$\kappa^2 \equiv \frac{1}{R^3} \frac{d}{dR} (R^4 \Omega^2).$$

Combining the perturbed equations (8)–(13) and eliminating all other variables in favor of the perturbed radial velocity v_{1R} , one obtains the wave equation

$$\begin{aligned} \frac{1}{v_A^2} \frac{\partial^2 v_{1R}}{\partial t^2} &= \frac{\partial^2 v_{1R}}{\partial R^2} + \frac{d \ln (R B_0^2)}{dR} \frac{\partial v_{1R}}{\partial R} \\ &- \left[\frac{\kappa^2}{v_A^2} + \frac{1}{R^2} \left(1 + \cos^2 i \frac{d \ln \rho_0}{d \ln R} \right) - \frac{\rho_0}{R B_0^2} \frac{d}{dR} \left(\frac{R}{\rho_0} \mathbf{B}_0 \cdot \mathbf{B}'_0 \right) \right] v_{1R}. \end{aligned} \quad (14a)$$

For power-law profiles, this becomes

$$\frac{1}{v_A^2} \frac{\partial^2 v_{1R}}{\partial t^2} = \frac{\partial^2 v_{1R}}{\partial R^2} - \frac{q}{R} \frac{\partial v_{1R}}{\partial R} - \left[\frac{\kappa^2}{v_A^2} + \frac{1}{R^2} \left(\frac{1-q}{2} - q \cos^2 i \right) \right] v_{1R}. \quad (14b)$$

To transform eqs. (14) to the Schrödinger form, we define a new independent variable Ψ through

$$v_{1R} = \frac{\Psi(R)}{\sqrt{R B_0^2}} e^{i\omega t}; \quad \text{or} \quad v_{1R} = R^{q/2} \Psi(R) e^{i\omega t} \quad (15)$$

for the power-law case. Then, we have

$$\frac{d^2\Psi}{dR^2} + K^2(R)\Psi = 0, \quad (16)$$

with $K(R)$ defined by

$$K^2(R) \equiv \frac{\omega^2 - \kappa^2}{v_A^2} - \frac{3}{4R^2} - \frac{d \ln \rho_0}{dR} \left(\frac{\cos^2 i}{R} + \frac{\mathbf{B}_0 \cdot \mathbf{B}'_0}{B_0^2} \right) + \left(\frac{\mathbf{B}_0 \cdot \mathbf{B}'_0}{B_0^2} \right)^2, \quad (17a)$$

or

$$K^2(R) \equiv \frac{\omega^2 - \kappa^2}{v_A^2} - \frac{1}{R^2} \left(\frac{1}{2} + \frac{q^2}{4} - q \cos^2 i \right) \quad (17b)$$

for the power-law case. Local (WKB) solutions to eq. (16) have $\Psi \sim e^{i \int k_R dR}$ with $Rk_R \gg 1$ and $dk_R/dR \ll k_R^2$. In this case, $\Psi'' \rightarrow -k_R^2 \Psi$, and we can use $K^2(R) = k_R^2$ to write a local dispersion relation

$$\omega^2 = v_A^2 k_R^2, \quad (18)$$

which corresponds to MHD fast modes propagating along the radial direction. When $|\omega|^2$ is comparable to or smaller than v_A^2/R^2 , however, modes are not localized, and solutions must be sought as a global problem subject to boundary conditions.

3.2. Global Analysis for the Fundamental Modes

In the previous section we showed that there is no short wavelength (local) unstable fundamental mode with $k_z = m = 0$ in self-similar MHD disk winds. Here, we present the results of a global normal-mode analysis performed with carefully chosen boundary conditions, and adopting the power-law equilibrium. Define the dimensionless radial variable $r \equiv R/R_e$, and dimensionless parameters $\alpha \equiv (q - 1) \cos^2 i + q(2 - q)/4$ and $\sigma^2 \equiv \omega^2 R_e^2 / v_A^2(R_e)$, with R_e being the position of the unperturbed outer edge of the wind. Then eq. (16) can be cast into the form

$$\frac{d^2\Psi}{dr^2} + \left(\frac{\alpha}{r^2} + \sigma^2 r \right) \Psi = 0. \quad (19)$$

It is not difficult to show that the general solutions of eq. (19) are

$$\Psi = \begin{cases} A\sqrt{r}J_\nu(2\sigma r^{3/2}/3) + B\sqrt{r}Y_\nu(2\sigma r^{3/2}/3), & \text{if } \sigma^2 > 0, \end{cases} \quad (20a)$$

$$\Psi = \begin{cases} C\sqrt{r}I_\nu(2|\sigma|r^{3/2}/3) + D\sqrt{r}K_\nu(2|\sigma|r^{3/2}/3), & \text{if } \sigma^2 < 0, \end{cases} \quad (20b)$$

with $3\nu \equiv \sqrt{1 - 4\alpha} = \sqrt{(1 - q)^2 + 4(1 - q) \cos^2 i}$. In eqs. (20), J_ν , Y_ν , and I_ν , K_ν are the ordinary and modified Bessel functions of the 1st and 2nd kinds, respectively, and the coefficients A, B, C , and D are constants to be determined from imposed boundary conditions.

Let us consider the case of a free Lagrangian boundary at which the total pressure due to initial and perturbed fields balances with a fixed external pressure at both inner and outer edges, which is equal to the unperturbed magnetic pressure. If the total pressure at an edge of an outflow is different from the external pressure, the boundary itself will move until a new balance exists. To first order, this condition of constant pressure at the boundary is written

$$\frac{1}{2} \frac{dB_0^2}{dR} \frac{\partial R_b}{\partial t} + \mathbf{B}_0 \cdot \frac{\partial \mathbf{B}_1}{\partial t} = 0, \quad (21)$$

where R_b is the location of the perturbed boundary. The first term of eq. (21) represents the change in the total pressure due to the boundary movement, while the second term arises from perturbed magnetic pressure itself. All quantities are evaluated at the unperturbed boundary position. Using eqs. (12), (13), and (15), and using $\partial R_b/\partial t = v_{1R}$ at boundaries, we find the desired boundary conditions are

$$\frac{d\Psi}{dr} + \frac{q/2 + \sin^2 i}{r} \Psi = 0, \quad \text{at } r = r_i \text{ and } 1, \quad (22)$$

where $r_i \equiv R_i/R_e$ is the normalized distance of an inner boundary from the axis. Together with the boundary conditions (22), eq. (19) forms a Sturm-Liouville system. By employing the variational principle one can show that σ^2 is real and that $\sigma^2(\Psi)$ is stationary subject to an arbitrary variation of Ψ .

When $\sigma^2 > 0$ (stable modes), the oscillatory properties of J_ν and Y_ν guarantee the existence of discrete eigenvalues σ_n with n denoting the number of nodes in the corresponding eigenfunction Ψ_n . The resulting eigenvalues for $r_i = 10^{-1}$ and 10^{-4} , and $0 < i < i_{\max}(q)$ are plotted in Fig. 1. Only a few cases with small n are shown. Eigenvalues associated with different i 's fill each shaded area completely. When $r_i = 10^{-4}$, eigenfunctions which link inner and outer boundaries have to extend across enormous changes in density and magnetic field strengths. In this case, $B/A \ll 1$ and eigenvalues become rather insensitive to the local properties such as q and i . When $r_i = 10^{-1}$, however, the wind mimics a slender hollow cylinder. The variation in density and field strengths over radius is slight, causing eigenvalues to be sensitive to i and q . In addition, the narrow width of the wind changes the number of nodes in eigenfunctions. When $q > 0.5$, for example, the eigenfunctions with $r_i = 10^{-1}$ have almost the same eigenvalues as, but one more node than, the $r_i = 10^{-4}$ case, as seen in Fig. 1.

When $r_i \ll 1$ and $\sigma^2 \gg 1$, the asymptotic solutions to eqs. (20a) and (22) gives $\sigma_n = 3\pi n/2 + 3\pi(2\nu + 1)/8$. These are plotted with dotted lines in Fig. 1b, and show good agreement with the values calculated without any assumption (even for $n = 0$). The case with $q = 0.5$ and $i = 0$ is special, because the slope of the eigenfunction at the inner boundary is $-1/4$, which automatically satisfies the boundary condition (22). In this case the asymptotic eigenvalues are $\sigma_n = 3\pi n/2$, drawn as filled circles in Fig. 1b. Eigenvalues have no upper bound as $n \rightarrow \infty$, which is a general property of solutions to a Sturm-Liouville equation (Morse & Feshbach 1953).

Now consider the unstable global solutions with $\sigma^2 < 0$. Let ψ_1 and ψ_2 be the two linearly independent solutions of Ψ : $\psi_1 \equiv \sqrt{r}I_\nu(2|\sigma|r^{3/2}/3)$ and $\psi_2 \equiv \sqrt{r}K_\nu(2|\sigma|r^{3/2}/3)$ such that $\Psi =$

$C\psi_1 + D\psi_2$. Because ψ_1 is a monotonically increasing function of r (i.e., $\psi_1, \psi_1' > 0$ always) and Ψ must have a negative logarithmic slope at the inner and outer boundaries (cf. eq. [22]), ψ_1 alone can not constitute eigenfunctions for global modes. In addition, since ψ_1 increases exponentially for a large value of $|\sigma|r^{3/2}$, while $\psi_2, \psi_2' \rightarrow 0$, the outer free Lagrangian boundary condition requires $C/D \rightarrow 0$. Although C is not strictly zero when $|\sigma|$ has a relatively small value, the contribution of ψ_1 to global solutions near the inner boundary is negligibly small. Thus, unstable eigenvalues, if they exist, are essentially determined by the inner boundary condition imposed on ψ_2 .

As we move inward from the outer boundary, ψ_2 rapidly increases asymptoting to

$$\psi_2 \sim r^{(1-3\nu)/2} \left[1 - \frac{\pi\nu|\sigma|^{2\nu}}{3^{2\nu} \sin(\pi\nu)\Gamma^2(\nu+1)} r^{3\nu} + \dots \right], \quad (23)$$

for $r \ll 1$ (cf. Abramowitz & Stegun 1965), where $\Gamma(\nu+1)$ is a Gamma function. In fact, $(1-3\nu)/2$ is the maximum logarithmic slope $\psi_2(r)$ can ever attain. From the inner boundary constraint (22), the existence of unstable global solutions is guaranteed if $(1-3\nu)/2 > -(q/2 + \sin^2 i)$, or, equivalently

$$q > 1 - \frac{(1 + \sin^2 i)^2}{2}, \quad (24)$$

is satisfied. Eq. (24) is the global instability criterion for the fundamental modes of self-similar, cold, magnetized winds, subject to the free boundary conditions expressed by eq. (22). By putting $C = 0$ and neglecting higher order terms in ψ_2 , we derive from eqs. (22) and (23) the approximate, analytic expression for the eigenvalues of the global instability

$$|\sigma|r_i^{3/2} = \frac{|\omega|R_i}{v_A(R_i)} = 3 \left[\frac{\sin(\pi\nu)\Gamma^2(\nu+1)}{\pi\nu} \frac{(1-3\nu+q+2\sin^2 i)}{(1+3\nu+q+2\sin^2 i)} \right]^{1/2\nu}, \quad (25)$$

which again shows that $|\sigma|$ has a positive real value if eq. (24) holds.

In Fig. 2 we plot the approximate growth rates for unstable modes from eq. (25) as dotted lines, as well as the exact growth rates numerically computed for $r_i = 10^{-4}$ (thin solid lines) and for $r_i = 0.1$ (dashed lines). The curves shown are for $i = 0^\circ, 5^\circ, \dots, 35^\circ, 40^\circ$ from right to left, and the uppermost thick lines are for i_{\max} calculated from eq. (7). Note that varying the width of outflow via r_i yields very little change in the plotted solutions: r_i -dependence of the growth rates appears mainly through the product $|\sigma|r_i^{3/2}$. Eq. (25) gives accurate growth rates for relatively small values of $|\sigma|r_i^{3/2}$, while its estimates deviate up to $\sim 16\%$ from the exact values as $|\sigma|r_i^{3/2}$ becomes larger. In this case we need to include next order terms in ψ_2 (cf. eq. [23]) to obtain more accurate results. For a given set of equilibrium parameters, we note that whereas there exist an infinite set of stable eigenmodes, there is (at most) a unique unstable eigenmode. Noting $|\omega| \equiv |\sigma|v_A(R_e)/R_e = |\sigma|r_i^{3/2}v_A(R_i)/R_i$, we expect from Fig. 2 that the system is typically globally unstable within ~ 5 crossing times of Alfvén waves at the inner boundary.

Once the ratios of the coefficients and the eigenfrequencies are found for the fundamental modes, one can easily construct radial solutions for the perturbed variables: $\rho_1, v_{1R}, v_{1\phi}$, and $B_{1\phi}$.

These are plotted in Fig. 3 for $i = 0^\circ$ and $r_i = 10^{-3}$. Fig. 3a corresponds to a stable case with $q = 0.4$ and $\sigma_0 = 2.42$, while Fig. 3b depicts an unstable case with $q = 0.6$ and $|\sigma|r_i^{3/2} = 0.11$. Although normalization is arbitrary, we note that for the unstable modes, the negative radial velocity case drives the entire system into a more stable configuration (with lower magnetic energy) when the equilibrium magnetic field is predominantly toroidal. This can be shown as follows: Let δM , δE_B , and $\delta\Phi_B$ denote the mass, magnetic energy, and toroidal magnetic flux per unit height in a local flux tube. Then we have $\delta E_B = (\pi/2)(\delta\Phi_B/\delta M)^2\delta M\rho R^2$. For a given flux tube, δM and $\delta\Phi_B/\delta M$ are constant in time and $\delta M > 0$. Thus, $\text{sgn } d(\delta E_B)/dt = \text{sgn } d(\rho R^2)/dt = \text{sgn } [\rho_0 R^2(v_{1R}/R - \partial v_{1R}/\partial R)]$ from the equation of continuity. If v_{1R}/R dominates $\partial v_{1R}/\partial R$ and $v_{1R} < 0$, then $\text{sgn } d(\delta E_B)/dt < 0$; magnetic energy decreases with time, meaning that the system evolves into a more stable state. Thus we scale $v_{1R}/v_{0\phi} = 1$ at $r = 1$ for Fig. 3a and $v_{1R}/v_{0\phi} = -1$ at $r = r_i$ for Fig. 3b, respectively. Note that stable eigenfunctions have their largest amplitude near the outer boundary, while the inner, high density region is nearly static during oscillation. Unstable eigenfunctions, on the other hand, are almost zero except in the region close to the inner boundary. The respective inner-region vs. outer-region predominance of unstable vs. stable eigenfunctions reflects the respective characteristic frequencies as well: the inner-wind unstable modes grow at large rates comparable to Alfvén frequencies in the interior, whereas outer-wind stable modes oscillate at low frequencies comparable to the Alfvén frequencies in the exterior.

We remark that there is no globally unstable fundamental mode when one adopts rigid boundaries with $\Psi(r) = 0$ at both $r = r_i$ and $r = 1$, instead of the free Lagrangian boundaries, since both ψ_1 and ψ_2 are monotonic functions of R . If $\Psi'(r) = 0$ is imposed at both boundaries (cf. Dubrulle & Knobloch 1993), however, we still have unstable fundamental modes with a different instability criterion¹ and different growth rates.

We discuss the significance of fundamental modes to protostellar outflows in §8.3.

4. Local Analysis for Cold Winds

We now consider general non-axisymmetric Eulerian perturbations with small amplitudes. Neglecting the effects of thermal pressure and external gravity due to a central object, we linearize eqs. (1)~(4)

$$\frac{d\rho_1}{dt} = -\frac{1}{R}\frac{\partial}{\partial R}(R\rho_0v_{1R}) - \frac{1}{R}\frac{\partial}{\partial\phi}(\rho_0v_{1\phi}) - \frac{\partial}{\partial z}(\rho_0v_{1z}), \quad (26)$$

$$\frac{dv_{1R}}{dt} = 2\Omega v_{1\phi} + \frac{1}{4\pi\rho_0} \left[-\frac{2B_{0\phi}B_{1\phi}}{R} + \frac{B_{0\phi}}{R}\frac{\partial B_{1R}}{\partial\phi} + B_{0z}\frac{\partial B_{1R}}{\partial z} - \frac{\partial}{\partial R}(\mathbf{B}_0 \cdot \mathbf{B}_1) + \frac{\rho_1}{\rho_0} \left(\frac{B_{0\phi}^2}{R} + \mathbf{B}_0 \cdot \mathbf{B}'_0 \right) \right], \quad (27)$$

$$\frac{dv_{1\phi}}{dt} = -\frac{\kappa^2}{2\Omega}v_{1R} + \frac{1}{4\pi\rho_0} \left[\left(B'_{0\phi} + \frac{B_{0\phi}}{R} \right) B_{1R} + B_{0z} \left(\frac{\partial B_{1\phi}}{\partial z} - \frac{1}{R}\frac{\partial B_{1z}}{\partial\phi} \right) \right], \quad (28)$$

¹In this case, eq. (24) would become $(1 - 3\nu)/4 = \alpha > 0$, corresponding to $R^2(K^2(R) - \omega^2/v_A^2) > 0$.

$$\frac{dv_{1z}}{dt} = -v'_{0z}v_{1R} + \frac{1}{4\pi\rho_0} \left[B'_{0z}B_{1R} + B_{0\phi} \left(\frac{1}{R} \frac{\partial B_{1z}}{\partial \phi} - \frac{\partial B_{1\phi}}{\partial z} \right) \right], \quad (29)$$

$$\frac{dB_{1R}}{dt} = \frac{B_{0\phi}}{R} \frac{\partial v_{1R}}{\partial \phi} + B_{0z} \frac{\partial v_{1R}}{\partial z}, \quad (30)$$

$$\frac{dB_{1\phi}}{dt} = R\Omega' B_{1R} - \frac{\partial}{\partial R}(B_{0\phi}v_{1R}) + B_{0z} \frac{\partial v_{1\phi}}{\partial z} - B_{0\phi} \frac{\partial v_{1z}}{\partial z}, \quad (31)$$

$$\frac{dB_{1z}}{dt} = v'_{0z}B_{1R} - \frac{1}{R} \frac{\partial}{\partial R}(RB_{0z}v_{1R}) + \frac{B_{0\phi}}{R} \frac{\partial v_{1z}}{\partial \phi} - \frac{B_{0z}}{R} \frac{\partial v_{1\phi}}{\partial \phi}, \quad (32)$$

where the Lagrangian time derivative is denoted by

$$\frac{d}{dt} \equiv \frac{\partial}{\partial t} + \Omega(R) \frac{\partial}{\partial \phi} + v_{0z} \frac{\partial}{\partial z}, \quad (33)$$

and again the subscripts 0 and 1 indicate the equilibrium and perturbation variables, respectively.

Since all the coefficients of the perturbed variables in eqs. (26)~(32) do not depend on the coordinates ϕ and z , we may look for solutions having sinusoidal dependence on ϕ and z . Furthermore, if there exist any normal modes, we can write eigenfunctions in the form

$$\chi_1(R, \phi, z, t) = \chi_1(R) e^{i(m\phi + k_z z - \omega t)}, \quad (34)$$

where χ_1 refers to any physical variable of perturbations. Substituting eq. (34) into the set of eqs. (26)~(32) and eliminating all other variables in terms of the radial Lagrangian displacement $\xi_R \equiv -v_{1R}/i\tilde{\omega}$ with a Doppler shifted frequency

$$\tilde{\omega} \equiv \omega - m\Omega - k_z v_{0z},$$

we obtain the second order differential equation

$$\frac{d^2 \xi_R}{dR^2} + \frac{d}{dR} \ln \left(RB_0^2 \frac{\tilde{\omega}_A^2}{\tilde{\omega}_F^2} \right) \frac{d\xi_R}{dR} + \frac{H(R)}{\tilde{\omega}_A^2} \xi_R = 0, \quad (35)$$

where

$$\begin{aligned} H(R) &\equiv \tilde{\omega}_F^2 \left\{ \frac{\tilde{\omega}_A^2 - \kappa^2}{v_A^2} - F_B \frac{d \ln \rho_0}{dR} - \frac{1}{R^2} + \frac{1}{RB_0^2} \frac{d}{dR} (R\mathbf{B}_0 \cdot \mathbf{B}'_0) \right\} \\ &- 4\Omega \left\{ \tilde{\omega} \left(\frac{m}{R} F_B + \frac{B_{0z}}{RB_0} G_+ \right) + \Omega k^2 \frac{B_{0z}^2}{B_0^2} - v_A^2 k^2 F_B \frac{B_{0\phi}(\mathbf{k} \cdot \mathbf{B}_0)}{\tilde{\omega} B_0^2} \right\} \\ &- \left(\frac{d}{dR} \ln \frac{\tilde{\omega}_F^2}{RB_0^2} - \frac{d}{dR} \right) \left\{ v_A^2 F_B G_-^2 + 2\Omega G_- \tilde{\omega} \frac{B_{0z}}{B_0} + \frac{v_A^2}{R} G_+ G_- \right\} \\ &- v_A^2 \left\{ k^2 F_B^2 \frac{\tilde{\omega}_A^2}{\tilde{\omega}^2} + \frac{2}{R} F_B G_+ G_- + \frac{G_+^2}{R^2} \right\}, \end{aligned} \quad (36a)$$

with

$$F_B \equiv \frac{1}{B_0^2} \left(\frac{B_{0\phi}^2}{R} + \mathbf{B}_0 \cdot \mathbf{B}'_0 \right), \quad G_{\pm} \equiv \frac{1}{B_0} \left(\frac{m}{R} B_{0z} \pm k_z B_{0\phi} \right), \quad (36b)$$

$$\tilde{\omega}_A^2 \equiv \tilde{\omega}^2 - v_A^2(\mathbf{k} \cdot \mathbf{b}_0)^2, \quad \tilde{\omega}_F^2 \equiv \tilde{\omega}^2 - v_A^2 k^2, \quad \text{and} \quad \mathbf{k} \equiv (0, \frac{m}{R}, k_z).$$

Here, F_B represents the equilibrium magnetic force, and $\tilde{\omega}_A$ and $\tilde{\omega}_F$ are frequencies connected to the Alfvénic and fast magnetosonic modes in cold MHD fluids, respectively. $\mathbf{b}_0 \equiv \mathbf{B}_0/|\mathbf{B}_0|$ is the unit vector along an equilibrium field direction, and finally \mathbf{k} is a vector wavenumber. When $m = k_z = 0$, only the terms in the first bracket in the definition of $H(R)$ do not vanish, recovering the radial wave equation (eq. [16], [17a]) for the fundamental mode.

The second order differential equation (35) has a singularity at $\tilde{\omega}_A^2 = 0$, but if we treat a fully general problem including the thermal effects of compressible gas, we will find another singularity (a so called cusp singularity) at the positions where Doppler shifted frequencies of traveling waves match with slow MHD wave frequencies of the medium (cf. Roberts 1985). For an incompressible medium, $\tilde{\omega}_A^2 = 0$ singularities are often referred to as shear Alfvén singularities where because of resonances the characteristics of waves propagating radially would be modified to be either absorbed into or amplified by background medium, if considered as a boundary value problem (Ross et al. 1982; Curry & Pudritz 1996). As pointed out by Appert et al. (1974), the locations with $\tilde{\omega}_F^2 = 0$ in eq. (35) are not singularities; these cut-off points in our local analyses appear as resonance waves with frequencies having relatively small imaginary parts, suggesting potential attenuation or amplification of amplitudes.

To remove the second term in eq. (35) we further define

$$\xi_R \equiv \Psi \left(RB_0^2 \frac{\tilde{\omega}_A^2}{\tilde{\omega}_F^2} \right)^{-1/2}. \quad (37)$$

Then eq. (35) is reduced to the standard Schrödinger form of eq. (16), with generalized $K^2(R)$ defined by

$$K^2(R) \equiv \frac{H(R)}{\tilde{\omega}_A^2} - \frac{1}{2} \frac{d^2}{dR^2} \ln \left(RB_0^2 \frac{\tilde{\omega}_A^2}{\tilde{\omega}_F^2} \right) - \frac{1}{4} \left[\frac{d}{dR} \ln \left(RB_0^2 \frac{\tilde{\omega}_A^2}{\tilde{\omega}_F^2} \right) \right]^2. \quad (38)$$

Generally speaking, $K(R)$ is a function of R for fixed values of m , k_z , and ω . However, we can still consider the behavior in a local sense near some fixed R_o , such that K is close to $K(R_o)$. This is mathematically formalized as described in Lin et al. (1993) and Terquem & Papaloizou (1996). Let us consider in the nonuniform background the spatially localized wave packet of the form

$$\Psi = \psi(R - R_o) e^{ik_R(R - R_o)} + O\left(\frac{1}{k_R}\right),$$

where $\psi(r)$ is a function which is non-zero only in a small neighborhood of $r \equiv R - R_o = 0$. The scale over which $\psi(r)$ varies significantly must tend to zero as $k_R \rightarrow \infty$, but no faster than k_R^{-1} . Then, to leading order, $d^2\Psi/dR^2 \approx -k_R^2\Psi$, and the solution $k_R^2 = K^2(R, \tilde{\omega}, m, k_z)$ of the Schrödinger equation yields a local dispersion relation with the right hand side evaluated at a reference point R_o , provided k_R is limited to a sufficiently large value (i.e., $R_o k_R \gg 1$). We may invert this dispersion relation to find $\tilde{\omega} = W(m, k_z, k_R, R)$, so that k_R now plays the role of an independent parameter

and the dispersion relation yields the Doppler-shifted frequency $\tilde{\omega}$ of a wave near a position R_o having local wavevector \mathbf{k} . This is equivalent to a standard WKB approximation in the radial direction.

Solution of the local dispersion relation near R_o yields

$$\omega = W(m, k_z, k_R, R_o) + m\Omega(R_o) + k_z v_{0z}(R_o) + \mathcal{O}(r), \quad (39)$$

where the $\mathcal{O}(r)$ term is $(m\Omega'(R_o) + k_z v'_{0z}(R_o))r$. Defining $dk_R/dR \equiv -(\partial W/\partial R)/(\partial W/\partial k_R) \sim k_R/R$, the WKB condition $|dk_R/dR| \ll k_R^2$ will be satisfied for $k_R R \gg 1$. For normal mode solutions, the $\mathcal{O}(r)$ term in ω must provide a negligible contribution to the phase; this requires that we must have $|m\Omega'(R_o) + k_z v'_{0z}(R_o)|t \ll k_R$. For axisymmetric modes with negligible vertical shear, this is always satisfied. However, for $m \neq 0$ disturbances, or flows with non-negligible $k_z v'_{0z}$, spatially localized wavepackets maintain a characteristic radial wavenumber for only a limited time, altering their spatial pattern because of the background shear. For a wavepacket with initial wavenumber $k_R(0)$, the radial wavenumber at time t becomes, upon inclusion of $-t$ times the $\mathcal{O}(r)$ term in ω in the phase,

$$k_R(t) = k_R(0) - (m\Omega' + k_z v'_{0z})t. \quad (40)$$

Thus, for example, with $k_z = 0$, the pitch $\tan p \equiv m/Rk_R$ of a spiral pattern changes by a fraction $\epsilon = |dk_R|/k_R$ over time $t = \epsilon k_R/|m\Omega'|$. If $Rk_R \gg m$, the pattern changes slowly compared to the orbit time. Among nonaxisymmetric disturbances, the wavepackets with low m/Rk_R have the largest temporal range for which they remain close to normal modes of the system. In the following two sections, we present solutions for the growth rates of unstable disturbances determined from a local modal analysis (i.e., producing solutions $\tilde{\omega} = W(\mathbf{k}, R_o)$), with the understanding that when $|m\Omega' + k_z v'_{0z}| \neq 0$, the modal growth (i.e., $\sim e^{|\tilde{\omega}|t}$) with fixed pattern holds only for a limited time. In assessing the potential of the non-axisymmetric instabilities we shall identify to affect flow dynamics, we will consider their total amplification over times $< k_R R/m\Omega$, for which the spatial pattern changes little.

For simplicity let us define dimensionless variables

$$\sigma \equiv \tilde{\omega} R_o/v_A(R_o), \quad x_z \equiv k_z R_o, \quad x_R \equiv k_R R_o, \quad \kappa \equiv R_o \kappa_o/v_A(R_o),$$

$$\Omega \equiv R_o \Omega_o/v_A(R_o), \quad \text{and} \quad \zeta \equiv R_o v'_{0z}(R_o)/v_A(R_o).$$

Here, ζ measures the amount of shear in the vertical velocity of the winds, and the “o” subscripts in the equilibrium epicyclic and rotation frequencies denote evaluation at the reference point R_o . We adopt the power-law equilibria of §2. We now organize the terms in eq. (38) finally to get a 12th-degree polynomial

$$0 = \sigma^{12} + \sum_{j=0}^{10} f_j(q, i, x_R, x_z, m, \Omega, \zeta) \sigma^j. \quad (41)$$

The functional dependences of the coefficient f_j 's on the parameters are so complicated that it is not illuminating to write down the whole expression here. We may obtain more simplified forms

for f_j 's by sorting out terms and taking the limit of $x_R \gg 1$. Because there are various interesting modes which demand different regimes of parameters, however, we keep all the terms as the general local dispersion relation (with x_R large) and compute numerical growth rates by solving eq. (41) for σ as a function of the other variables. We present these numerical results in §5. In §6, we will classify individual (either unstable or overstable) modes and provide their limiting dispersion relations.

Terquem & Papaloizou (1996) considered only incompressible modes, for disk applications where thermal pressure is considerable, by taking a divergence-free displacement vector as a perturbation eigenvector, thus obtaining a 4th-order polynomial. Our dispersion relation, for applications to supersonic MHD winds in which thermal pressure is negligible hence motions are compressible, contains information about all possible, either oscillating or unstable, modes of cold MHD winds.

5. Numerical Solutions of Modal Dispersion Relation

The derived dispersion relation (41) is a 12th-order polynomial with real coefficients, indicating that solutions appear as complex conjugate pairs. Solutions having non-zero real and imaginary parts are overstable modes, and solutions with vanishing real parts are unstable modes. In this section, we present both types of solutions which are consistent with the local analysis by fixing $x_R = 10$. As we shall show, both higher values of x_R (more spatially localized) and lower values of x_R (less spatially localized) give qualitatively the same family of solutions as with $x_R = 10$.

5.1. Axisymmetric Modes of Instabilities

First, we consider the axisymmetric case with $m = 0$. For 4 selected sets of parameters, we plot the real and imaginary parts of the unstable and overstable modes in Fig. 4. A Keplerian rotation gradient with $\kappa^2 = \Omega^2$ is assumed and vertical shear is neglected except in $\tilde{\omega}$. We take Ω as arbitrary rather than using the relation (6), by allowing that the gravitational force from a central object also contributes to the equilibrium rotation velocity. Then, from eq. (5), the normalized angular velocity becomes

$$\Omega^2 = \kappa^2 = \cos^2 i - \frac{1+q}{2} + G_R, \quad (42)$$

where $G_R \equiv g_R(R_o)R_o/v_A^2(R_o) > 0$ is the normalized gravitational acceleration. Note that for $1+q > 0$ (i.e., magnetic fields decreasing outward), equilibrium solutions with i approaching 90° require non-zero gravity (because hoop stresses do not confine a primarily-poloidal flow). Also note that as G_R strengthens, the initial equilibrium is maintained by the balance between centrifugal and gravitational forces, implying that the magnetic force is negligible.

The behavior of the solutions shown in Fig. 4 (and similar behavior for other parameters) allows us to identify 4 different axisymmetric mode families: a toroidal resonance mode (TR),

an axisymmetric toroidal buoyancy mode (ATB), a poloidal buoyancy mode (PB), and a Balbus-Hawley (BH) mode. One (TR) of these is an overstable mode and the others (ATB, PB, and BH) are purely growing modes.

Fig. 4a and 4b correspond to a disk wind at large distance from the source, where magnetic fields are dominantly toroidal (small i) and centrifugal force balances magnetic force (small G_R), while Fig. 4c and 4d correspond to an accretion disk or inner part of a wind where magnetic fields are poloidal (large i) and centrifugal force is balanced by the gravity from a central object (relatively large G_R). In each frame, solid and dotted lines represent the imaginary and real parts of the frequencies, respectively. Fig. 4a shows the TR mode which splits into two branches in the presence of (arbitrarily small) poloidal magnetic fields (Fig. 4b and 4c). This TR mode is not a generic instability mode because it has a far larger real part (associated with ordinary MHD oscillations), indicating an overstability. With the presence of poloidal field components, there exist two different types of buoyancy modes, namely ATB and PB modes. When the pitch angle of the magnetic field is relatively small, the buoyancy instabilities are driven by the interplay of the centrifugal force with the hoop stress of toroidal fields, so we call these ATB modes. Since, as explained in §6.1.2, the ATB modes need non-zero poloidal fields as well to be unstable, they disappear when $i = 0$. On the other hand, the PB instability modes arise when the fields are predominantly poloidal so that the pressure gradient forces of poloidal fields and the gravity from a central object are main driving forces, similar in character to the Parker instability. ATB and PB are pure instability modes with $\text{Re}(\sigma)=0$, as shown in Fig. 4. These instability modes operate even in the arbitrarily high- k_z limit because of our cold MHD assumption; otherwise sound waves would stabilize short wavelength perturbations, as they do in the Parker instability. Fig. 4d shows that the BH instability mode appears when $G_R \gg 1$, corresponding to dynamically weak magnetic fields in the equilibrium; with reduced G_R (also shown in Fig. 4d), BH is stabilized by radial MHD wave motions when x_R is large. As discussed in §6.1.3 and §7.1, one interesting finding in our work is that the *compressible* axisymmetric BH mode is strongly suppressed even for G_R large when the toroidal field is sufficiently strong; in a cold, Kepler-rotating MHD flow, it is fully stabilized when the pitch angle $i < 30^\circ$ (see §6.1.3).

Fig. 5 shows how the characteristics of unstable/overstable modes change as i and G_R vary for the fixed values of $x_z = 4$, $x_R = 10$, and $q = \zeta = 0$. For a pure toroidal field configuration with $i = 0^\circ$, we observe only overstable TR modes that are almost independent of G_R . As i increases, ATB emerges but is stabilized by rotation with G_R large. When $i = 45^\circ$ and $q = 0$, the buoyancy mode disappears because with these parameters the net force from the background magnetic fields vanishes (cf. eqs. [5], [6], and [42]). When $i > 30^\circ$ the BH mode strengthens as G_R increases. This is because in our normalization higher values of G_R correspond to weaker equilibrium magnetic fields, with which the BH instability operates efficiently. At a pure poloidal configuration of magnetic fields, BH and PB modes remain unstable (Fig. 5d). Dotted lines at very small G_R in Fig. 5c and 5d mark the minimum value of G_R , available for given values of q and i , below which no initial equilibrium exists (cf. eq. [42]).

5.2. Non-Axisymmetric Modes of Instabilities

When non-axisymmetric perturbations are applied, the cold MHD system responds with 3 more modes which are either unstable or overstable, in addition to the axisymmetric modes. We shall refer to these as non-axisymmetric toroidal buoyancy (NTB), geometric poloidal buoyancy (GPB), and poloidal resonance (PR) modes. The PR modes are MHD waves which have non-zero azimuthal wavenumbers and become overstable when there is a radial gradient of the axial field, analogous to the TR modes. In addition to the above modes, systems with toroidal magnetic field configurations and non-zero sound speed are also subject to significant non-axisymmetric magnetorotational instability (NMRI) modes. Unlike the other three non-axisymmetric modes, the NMRI mode arises due to a differential rotation with $d\Omega/dR < 0$, where Ω is an angular velocity of the rotation. More than anything else, the fact that the NMRI in B_ϕ -dominated systems needs a finite sound speed to be unstable distinguishes it from the axisymmetric Balbus-Hawley instability, which can be unstable regardless of temperature for purely axial fields. As we shall discuss later, the basic mechanism for the onset of NMRI is quite different from that of axisymmetric BH instability. We reserve the discussion of NMRI modes for §7, concentrating here on numerical results for our basic cold MHD system.

Fig. 6 shows the unstable and overstable solutions of the dispersion relations for two combinations of selected parameters: Fig. 6a corresponds to a disk wind with small i and small G_R , while Fig. 6b is for the near-disk case with large i and large G_R . We assume a Keplerian rotation and take an arbitrary Ω once again using eq. (42). For all cases, we chose $x_R = 10$, $q = \zeta = 0$, and $m = 1$, and confirmed that changes to these parameters do not appreciably affect the qualitative results. Solid and dotted lines in Fig. 6 represent imaginary and real parts of the normalized wave frequencies, respectively. When $i = G_R = 0$, Fig. 6a shows the presence of unstable NTB and overstable TR modes which are split by the non-axisymmetry. NTB modes are nearly like PB modes in their physical basis and have an almost constant growth rate over a wide range of x_z . But they depend sensitively on the logarithmic gradients of the density and magnetic structures (i.e., q ; see Fig. 7). For an intermediate value of i , both TR and PR modes coexist. At some wavenumber x_z , they combine to simply vanish, but overall they give rise to complicated behavior of $\text{Im}(\sigma)$. When $i = 90^\circ$, we observe three unstable GPB, BH, and PB modes, and overstable PR modes (Fig. 6b). GPB modes are driven by a buoyancy force together with the geometrical effect. Note that the real parts of PR modes are linearly proportional to the vertical wavenumber x_z , as TR modes are, indicating that they are really overstable modes. Since $x_R \gg m$, however, there exists only a small contribution from non-axisymmetric effects to the axisymmetric BH and PB modes (cf. Fig. 4d). Remember that when $m \gg x_R$, the normal mode assumption rapidly breaks down because such high- m modes lose their spatial pattern very quickly; we investigate $m \gg x_R$ cases using different methods in §§7 and 8.

Fig. 7 shows how the characteristics of the buoyancy modes change as x_z , i , and q vary. When $G_R=0$, an initial equilibrium exists only for a limited range of $i < i_{\text{crit}} \equiv \cos^{-1} \sqrt{(1+q)/2}$ from eq. (42), with toroidal field components dominating over poloidal field components. In Fig. 7, therefore,

the unstable modes with $i < i_{\text{crit}}$ correspond to toroidal buoyancy modes, while poloidal buoyancy modes have $i > i_{\text{crit}}$. Generally speaking, with the assumption of extremely cold medium, smaller-scale buoyancy modes with high x_z have larger growth rates. When i is very small, as seen in Fig. 7, ATB modes are stable because they need the aid of poloidal fields to be unstable, while NTB modes become unstable for *all* $i < i_{\text{crit}}$. This reflects the physically different driving mechanisms between ATB and NTB instabilities. PB modes become more unstable with higher q (steeper background gradients), while ATB/NTB modes are more efficient with smaller q . Greater instability is simply associated with higher background magnetic force in the respective cases (cf. the initial equilibrium condition [42]).

The k_R -dependence of the unstable/overstable modes are summarized in Fig. 8. Here we fix $x_z = 2$ for all cases and choose $q = 0.8$, $G_R = 0$, and small i for Fig. 8a and 8c, corresponding to disk wind-like systems, and $q = 0$, $G_R = 5$, and large i for Fig. 8b and 8d, corresponding to accretion disks or disk winds near their sources. The BH instability modes are completely suppressed by MHD waves when $x_R \gtrsim 3$; we will show that this is consistent with the prediction of the asymptotic dispersion relation. All the other modes extend with smaller growth rates to larger x_R , with $\text{Im}(\sigma) \sim x_R^{-1}$, which we will show agrees well with the asymptotic dispersion relations (43), (45), (50), and (52) for the PB, ATB, TR, and NTB modes, respectively. For the PR modes the asymptotic dispersion relation (56), showing $\text{Im}(\sigma) \sim x_R^{-2/3}$, is valid only when $Rk_z \gg m$, which is not consistent with the parameters adopted in Fig. 8d. When $k_R \gg k_z \sim m/R$, one can confirm analytically that the PR modes also behave as $\text{Im}(\sigma) \sim x_R^{-1}$. In the shearing-wavelet point of view with eq. (40), Fig. 8 shows that kinematic shear arising from the background flows ultimately stabilizes both unstable and overstable modes, as k_R grows secularly increases in time. Although the local approximation breaks down if x_R is not large, Fig. 8 indicates that the BH mode exists and may show interesting behavior for small x_R . In addition, Fig. 8 also suggests larger growth rates when x_R is small for other modes, although the assumptions of this section of a radially-local, slowly-changing pattern are not self-consistent when x_R is small. To study dynamical growth of disturbances which occurs when $x_R \ll m$, we use direct integrations of the shearing-sheet equations. We present these results in §8.2 (for the NTB modes) and §§7.2 and 7.3 (for the NMRI modes and generalized MRIs).

6. Mode Classification

The cold MHD system we are investigating has 8 distinct local modes with $\text{Im}(\sigma) > 0$. Some of them (TR and PR) have larger $\text{Re}(\sigma)$ corresponding to overstability, while the others (PB, ATB, BH, NTB, GPB, and NMRI) have negligible $\text{Re}(\sigma)$, indicating pure instability. The NMRI modes do not appear in the numerical solutions because of the cold MHD assumption we made. Detailed discussion of the NMRI modes will be separately given in §7.2. In this section we describe the physical nature of the individual cold-fluid modes and present the respective dispersion relations under some limiting approximations.

6.1. Axisymmetric Modes

6.1.1. Poloidal Buoyancy Mode

Consider a system with pure axial fields. If gravitational forces are large, then they may balance the combined outward radial centrifugal force and pressure gradient force of outward-decreasing $B_{0z}(R)$; otherwise, if $g_R = 0$, then the strength in the magnetic fields must increase outward for an equilibrium to exist. In an initial state, at any point in the system the magnetic pressure force acting outward is balanced by the difference between gravity and the centrifugal force acting inward. If perturbed, a denser fluid element experiences reduced magnetic forces but unchanged centrifugal and gravitational forces per unit mass, and thus it would tend to sink radially inward dragging the field line with it; a lighter fluid element would correspondingly tend to float outward. Then, in a frozen-in-field condition, the neighboring gas finds itself on sloping lines of force and thus slides inward to add its weight and to cause field lines to bend more, expediting the instability. This poloidal buoyancy mode is analogous to the Parker instability (Parker 1966), with the driving force role of external gravity in Parker’s instability replaced by combination of gravity and the centrifugal force in the PB. The PB mode can occur for both axisymmetric and non-axisymmetric disturbances.

Putting $B_{0\phi} = m = 0$ and considering short wavelength perturbations with $v_{Az}^2 k_z^2 \gg \tilde{\omega}^2$ in eq. (38), one can find the dispersion relation for the poloidal buoyancy mode is

$$\tilde{\omega}^2 = - \left(\frac{1+q}{2} \right)^2 \frac{v_{Az}^2 k_z^2}{R^2 (k_z^2 + k_R^2)} = - \left(\frac{|g_R - R\Omega^2|^2}{v_{Az}^2} \right) \frac{k_z^2}{k_z^2 + k_R^2}. \quad (43)$$

Eq. (43) states that there is no preferred length scale as long as k_z is large. However, the inclusion of thermal effects would stabilize the PB mode with shorter wavelengths, as in the Parker instability² Also, sufficiently large $k_R \gg k_z$ stabilizes the mode.

²Also by taking a local approximation and by neglecting density stratification and the effects of thermal and cosmic ray pressures, one can simplify eq. (III.12) of Parker (1966) to get the asymptotic ($\mathbf{k} \rightarrow \infty$) dispersion relation

$$\omega^2 = - \left(\frac{g^2}{v_{A\parallel}^2} \right) \frac{k_{\parallel}^2}{k_{\perp}^2 + k_{\parallel}^2},$$

where g is the gravity perpendicular to the galactic plane, $v_{A\parallel}$ is the Alfvén speed of initial fields parallel to the galactic plane, and k_{\parallel} and k_{\perp} are perturbation wavenumbers in the respective directions parallel and perpendicular to the galactic disk and magnetic field. Comparing the above with eq. (43), we may write $g_{\text{eff}} \equiv g_R - R\Omega^2$ for the PB modes, with wavenumber correspondence $k_z \leftrightarrow k_{\parallel}$ and $k_R \leftrightarrow k_{\perp}$.

6.1.2. Axisymmetric Toroidal Buoyancy Mode

Now consider a system with weak poloidal but strong toroidal field components and negligible gravity. When magnetic fields are predominantly toroidal (i.e., when $i < \cos^{-1} \sqrt{(1+q)/2}$ from eq. [42]), an initial equilibrium state is maintained by the balance mainly between the centrifugal force acting outward, and magnetic hoop stresses which act inward. With sinusoidal density perturbations with k_z imposed on the equilibrium, a heavier blob of material would tend to float radially outward under the action of unchanged centrifugal forces per unit mass but reduced specific magnetic forces; a lighter element would correspondingly tend to sink. The radial motions of the heavier and lighter blobs are in opposite directions and thus cause the poloidal field lines to bend, creating radial perturbed fields.

The azimuthal fluid motion is slightly accelerated by the tension force exerted by the initial toroidal and the perturbed radial fields (cf. $B_{0\phi}B_{1R}/R$ term in eq. [28], associated with spiral magnetic field line projections in the $z=\text{constant}$ plane). This causes the initial poloidal component of field lines to bend now in the azimuthal direction, creating bands of perturbed azimuthal fields with signs alternating in the \hat{z} direction. The resulting total azimuthal fields are distributed in such a way that the heavier (lighter) blob in the initial perturbation has a lower (higher) toroidal field strength. Induced motions due to the vertical magnetic pressure gradient force carry the matter from under dense to over dense regions, closing the loop and amplifying the initial perturbation.

By setting $m = v_{0z} = 0$ and taking the $v_A^2 k_z^2 \gg \tilde{\omega}^2$ limit, we obtain from eq. (38) the following dispersion relation

$$0 = \tilde{\omega}^4 - \left[v_{Az}^2 (k_z^2 + k_R^2) + \kappa^2 - 4\Omega^2 \frac{B_{0z}^2}{B_0^2} \right] \tilde{\omega}^2 - 4\Omega v_{A\phi} v_{Az} F_B k_z \tilde{\omega} - v_A^2 v_{Az}^2 F_B^2 k_z^2, \quad (44)$$

with $F_B = (\cos^2 i - (1+q)/2)/R$. When $v_{A\phi} = 0$ (i.e., with pure poloidal fields), eq. (44) immediately recovers eq. (43), the limiting dispersion relation for PB modes. On the other hand, if $v_{Az} = 0$, there is no unstable ATB mode, clearly demonstrating that ATB modes operate by bending poloidal field lines. From Fig. 5b, we note that ATB modes are stabilized by rotation (larger G_R corresponds to stronger rotation). It can be shown from eq. (44) that when $Rk_z, Rk_R \gg \tilde{\omega}$, the critical wavenumbers are $(k_z^2 + k_R^2)_{\text{crit}} = -(d\Omega^2/d \ln R)/(v_A^2 \sin^2 i)$, below which the system is stable against the ATB modes. For $k_z \gg k_{z,\text{crit}}$, eq. (44) is further reduced to

$$\tilde{\omega}^2 = - \left(\cos^2 i - \frac{1+q}{2} \right)^2 \frac{v_A^2 k_z^2}{R^2 (k_z^2 + k_R^2)} = - \left(\frac{|g_R - R\Omega^2|^2}{v_A^2} \right) \frac{k_z^2}{k_z^2 + k_R^2}. \quad (45)$$

Since ATB instabilities are axisymmetric modes, they can persist without being disturbed by the kinematic growth of k_R due to shear, if $v'_{0z} = 0$.

Among well-known plasma modes, the pinch or sausage mode of a plasma column is most similar to the ATB in overall geometry and effect. Both are axisymmetric and require the radial tension force from predominantly toroidal magnetic fields to drive the instability. For both the

plasma pinch mode and the ATB of cold cylindrical winds, the net effect is that matter tends to be ejected radially in bands alternating with contracting magnetic field loops. However, in pinch modes, the plasma is generally unmagnetized and surrounded by *external* toroidal fields, and axial fields tend to suppress the instability. In the ATB, on the other hand, *internal* toroidal magnetic fields permeate the fluid, and non-zero axial fields are required for instability.

6.1.3. Compressible Balbus-Hawley Mode

In the presence of axial magnetic fields, a differentially rotating disk is unstable to an axisymmetric incompressible perturbation (Balbus & Hawley 1991; see also Velikhov 1959 and Chandrasekhar 1960). Because this Balbus-Hawley instability³ has a rapid growth time (comparable to the local rate of rotation) and exists for arbitrarily weak magnetic field strength, it is believed to provide a powerful mechanism for the generation of the effective viscosity in astrophysical accretion disks. Through numerical simulations, Hawley & Balbus (1991) argued that the roles of compressibility and toroidal fields are not significant as long as the total field strength is subthermal. Also, Blaes & Balbus (1994) studied the effect of toroidal fields on the compressible axisymmetric BH instability and showed that toroidal fields do not modify the instability criterion, while reducing growth rates slightly if $v_{A\phi} < c_s$. We find the striking result that under extremely cold conditions (i.e., $v_A \gg c_s$), compressibility prohibits the axisymmetric BH instability from occurring if the toroidal fields are as strong as the poloidal fields.

By taking the weak magnetic field limit ($\Omega \gg v_A k_R, v_A k_z$) and $m = 0$, we obtain from eq. (38) the following dispersion relation for the compressible axisymmetric BH instability in a cold MHD flow

$$\omega^4 - \omega^2[v_A^2(k_z^2 + k_R^2) + v_{Az}^2 k_z^2 + \kappa^2] + v_A^2 k_z^2 [v_{Az}^2(k_z^2 + k_R^2) + \kappa^2 - 4\Omega^2 \sin^2 i] = 0, \quad (46)$$

and thus from the last term in eq. (46) we obtain the instability criterion

$$v_{Az}^2(k_z^2 + k_R^2) + \kappa^2 - 4\Omega^2 \sin^2 i < 0. \quad (47)$$

With an $\Omega \propto R^{-a}$ rotation profile, eq. (47) implies that if $\sin^2 i < 1 - a/2$, we anticipate no BH instability in a cold flow. For a Keplerian rotation law with $a = 3/2$, for instance, no axisymmetric BH instability occurs if $i < 30^\circ$!; *when the magnetic field strength is superthermal, the inclusion of toroidal fields tends to suppress the growth of the BH instability.* With a steeper rotation profile (as would occur, for example, in winds from boundary layers), there is an increase in the range of i for which a system is BH-unstable.

We defer the full discussion on the BH instability until §7.1, where we explicitly include pressure terms in the dynamical equations.

³Often referred to magnetorotational instability, or briefly, MRI.

6.1.4. Toroidal Resonance Mode

Consider a system having pure toroidal fields without rotation. If the initial fields are homogeneous in space, magnetosonic waves, driven solely by magnetic pressure (with the assumption of the cold medium), would propagate without any interruption in the plane whose normal is perpendicular to the magnetic field direction. In an inhomogeneous medium, however, MHD waves no longer maintain a sinusoidal planform, and the characteristics of the waves change through the interaction with the background medium. The amplitudes of the waves may sometimes increase as they propagate, or sometimes they may become evanescent and decay at a resonance, or even may be trapped between two resonance points (cf. Rae & Roberts 1982). In such a strongly structured medium, the classification of MHD waves is not in general possible.

Our local treatment of MHD waves can provide some insight on the amplification or evanescence of propagating MHD waves in a structured medium. For $\tilde{\omega}_F^2 \rightarrow 0$ and $B_{0z} = \Omega = 0$, the local wave equation (35) can be simplified as

$$\frac{d^2 \xi_R}{dR^2} - \frac{d \ln \tilde{\omega}_F^2}{dR} \frac{d \xi_R}{dR} + \frac{\tilde{\omega}_F^2}{v_{A\phi}^2} \xi_R = 0. \quad (48)$$

Again we define $\xi_R \equiv (\tilde{\omega}_F^2)^{1/2} \Psi$, then eq. (48) takes the form of eq. (16) with $k_R \equiv K(R)$ defined by

$$k_R^2 \equiv \frac{\tilde{\omega}_F^2}{v_{A\phi}^2} - \frac{3}{4} \left(\frac{v_{A\phi}^2 k_z^2}{R \tilde{\omega}_F^2} \right)^2, \quad (49)$$

where $v_{A\phi} \propto R^{-1/2}$ was assumed. Thus, considering limiting cases of k_z and k_R , one can find the dispersion relation for this mode near the resonance frequencies (i.e., $\tilde{\omega} \approx v_{A\phi} k_z$)

$$\tilde{\omega}^2 = \begin{cases} v_{A\phi}^2 k_z^2 [1 + (3/4)^{1/2} e^{\pm \pi i/2} (R k_R)^{-1}], & \text{for } R k_R \gg R k_z \gg 1, \\ v_{A\phi}^2 k_z^2 [1 + (3/4)^{1/3} e^{\pm 2\pi i/3} (R k_z)^{-2/3}], & \text{for } R k_z \gg R k_R \gg 1, \end{cases} \quad (50)$$

showing that the imaginary part of toroidal resonance mode vanishes quickly as $k_R \rightarrow \infty$, while its real part gets bigger as k_z increases. Therefore, it is not adequate to regard TR modes as a true local instability mode. Though the TR mode is not a local instability, it suggests potential for waves to have global instabilities in which the magnetosonic resonance ($\tilde{\omega} = v_{A\phi} k_z$) plays a similar role to the Lindblad resonance in rotating disks. Thus, waves of fixed frequency propagating with a radial component of \mathbf{k} into their magnetosonic resonances may be amplified or reflected.

The modification of traveling waves due to the inhomogeneity of the medium is mediated through the magnetic pressure. A similar effect would occur when hydrodynamic waves propagate into an inhomogeneous medium.

6.2. Non-Axisymmetric Modes

6.2.1. Non-Axisymmetric Toroidal Buoyancy Mode

The non-axisymmetric toroidal buoyancy mode is very similar to the PB mode in its physical mechanism, in spite of the different field geometry. For toroidal-field dominated cases, an equilibrium can exist with the net inward magnetic stresses balancing the outward centrifugal force. When the system is perturbed non-axisymmetrically, the instability would develop similarly to PB modes, as described in §6.1.1. For the B_ϕ -dominated case, however, over-dense regions float outward and under-dense regions sink, because the inward magnetic forces are enhanced when the density drops.

Setting $B_{0z} = v_{0z} = 0$ and assuming $Rk_z \ll m, Rk_R$, one can show that the general dispersion relation (38) is reduced to the following quartic equation in terms of $\tilde{\omega}$

$$0 = \tilde{\omega}^4 - \left[v_{A\phi}^2 \left(\frac{m^2}{R^2} + k_R^2 \right) + \kappa^2 \right] \tilde{\omega}^2 - 4\Omega \frac{m}{R} F_B v_{A\phi}^2 \tilde{\omega} - v_{A\phi}^4 F_B^2 \left(\frac{m}{R} \right)^2, \quad (51)$$

with $F_B = (1-q)/2R$, The negative last term in eq. (51) guarantees the existence of unstable NTB modes. The third term (caused by the coupling of the rotation with the background fields) tends to stabilize NTB modes. Thus, if

$$\frac{m^2}{R^2} + k_R^2 < \frac{(4\Omega^2 - \kappa^2)}{v_{A\phi}^2},$$

there is no unstable NTB mode. Note that for wind equilibria with $B_{0z} = 0$, from eq. (6) the RHS of the above equals $3(1-q)/2R^2$; thus the NTB instability will be present at all m when $1/3 < q < 1$.

In the limit of large m , we obtain the asymptotic dispersion relation for the NTB mode

$$\tilde{\omega}^2 = - \left(\frac{1-q}{2} \right)^2 \frac{v_{A\phi}^2 m^2}{R^2(m^2 + R^2 k_R^2)} = - \left(\frac{|g_R - R\Omega^2|^2}{v_{A\phi}^2} \right) \frac{m^2}{m^2 + R^2 k_R^2}. \quad (52)$$

Here for the second equality, eq. (6) with $i = 0^\circ$ is used. Eq. (52) is akin to eq. (43), the dispersion relation for the PB mode, and to eq. (45), the dispersion relation for the ATB mode, reflecting the common origin in buoyancy forces of all three. In fact, Fig. 7 clearly shows how the various buoyancy modes extend and smoothly join at intermediate pitch angles.

6.2.2. Geometric Poloidal Buoyancy Mode

Now suppose a system with pure vertical fields. When perturbed azimuthally, a fluid element becomes over dense and tends to move inward due to the decreased background magnetic pressure force per unit mass if $0 < q < 1$. This geometrically converging motion of fluid increases density and field strength by factors of $(1-q)$ and $(1-q)/2$, respectively. On the other hand, the magnetic

field enhancement induces diverging motions of the fluid in the azimuthal direction by building up a pressure gradient, tending to lower the density. The net effect of these two processes is a density increase by a factor of $(1 - q)/2$, accelerating the inward motion of the heavier element. When $m \gg Rk_z$, the dispersion relation for this GPB mode is found to be

$$\tilde{\omega}^2 = - \left(\frac{1 - q^2}{4} \right) \frac{v_{Az}^2 m^2}{R^2(m^2 + R^2 k_R^2)}. \quad (53)$$

When $q = 1$, there is no instability. This is because the initial configuration of the density and the field is such that the mass and magnetic flux contained in a thin ring with the thickness dR and the radius R are constant over R , and no gain from the geometrical effect is possible.

6.2.3. Poloidal Resonance Mode

The physical basis for the poloidal resonance mode is quite similar to that of the toroidal resonance mode. The only difference between them is the background field geometry. In the presence of pure axial fields, MHD waves with non-zero m are easily influenced by radial magnetic pressure gradients.

To derive the dispersion relation near the resonance frequencies (i.e., $\tilde{\omega}_F \approx 0$), let us suppose a system with pure axial fields and neglect the vertical velocity shear. The system is also assumed to rotate slowly enough that the effects of rotation may not be important in the wave dynamics (i.e., $mv_{Az} \gg R\Omega$). For $\tilde{\omega}^2 \rightarrow v_{Az}^2(k_z^2 + m^2/R^2)$, we are left from eq. (35) with

$$\frac{d^2 \xi_R}{dR^2} + \frac{d}{dR} \ln \left(\frac{\tilde{\omega}_A^2}{\tilde{\omega}_F^2} \right) \frac{d\xi_R}{dR} + \frac{\tilde{\omega}_F^2}{v_{Az}^2} \xi_R = 0. \quad (54)$$

We now define $\xi_R \equiv (\tilde{\omega}_F^2/\tilde{\omega}_A^2)^{1/2} \Psi$ to simplify eq. (54) into eq. (16) with $k_R \equiv K(R)$ defined by

$$k_R^2 \equiv \frac{\tilde{\omega}_F^2}{v_{Az}^2} - \frac{m^2 v_{Az}^2}{R^2 \tilde{\omega}_F^2} \left(\frac{d \ln \tilde{\omega}_F^2}{dR} \right)^2, \quad (55)$$

where we took the limit of $Rk_z \gg m$ and assumed $v_{Az} \propto R^{-1/2}$. Solving eq. (55) for two limits of k_R , we obtain the dispersion relation near the resonance frequencies

$$\tilde{\omega}^2 = \begin{cases} v_{Az}^2 k_z^2 [1 + e^{\pi i/3} (ma_{\text{sh}})^{2/3} (R^2 k_R k_z)^{-2/3}], & \text{for } Rk_R \gg Rk_z \gg m, \\ v_{Az}^2 k_z^2 [1 \pm e^{\pi i/2} (ma_{\text{sh}})^{1/2} (Rk_z)^{-1}], & \text{for } Rk_z \gg Rk_R \gg m, \end{cases} \quad (56)$$

where $a_{\text{sh}} \equiv 1 \pm 3m\Omega/v_{Az}k_z$, showing again a rapidly declining imaginary part as k_R increases, at which the local approximation is valid. Thus, just like TR modes, PR modes are not strictly local instability modes.

7. Magnetorotational Instability

7.1. Axisymmetric BH Instability

In the preceding section, we briefly discussed the axisymmetric BH instability in a cold, differentially rotating medium and found that the BH instability can be suppressed by the azimuthal component of magnetic fields, if the medium is cold enough. Incompressibility has generally been adopted in the study of the BH instability in an accretion disk on the grounds that in such a system the magnetic fields are subthermal and thus acoustic waves can maintain the incompressible condition over many rotation periods. For magnetocentrally driven winds, however, sound waves play a minor role in controlling the dynamics and thus the incompressible approximation is inapplicable. In addition, since an initial equilibrium is attained through the balance between the centrifugal and magnetic forces (cf. eq. [5]), the Alfvén crossing time scale is comparable to the rotation time scale ($v_A \sim R\Omega$); in this case, the fields are not weak and the unstable range of wavenumbers becomes narrow.

We generalize the previous discussion of the axisymmetric compressible BH instability by explicitly including the thermal pressure terms in the momentum equation and exploring the role of compressibility to the development of the Balbus-Hawley instability. We consider a cylindrical flow threaded by both vertical and azimuthal magnetic fields, ignoring the radial variations in the initial configuration except $\Omega = \Omega(R)$ and neglecting the vertical velocity. We assume the medium is isothermal and take the WKB ($Rk_z \gg 1$) approximation. Through the standard approach to linear analyses, we arrive at the dispersion relation for the compressible version of the BH instability

$$(\omega_A^2 - \kappa^2)f(\omega^2) = k_R^2\omega_A^2((c_s^2 + v_A^2)\omega^2 - c_s^2v_{Az}^2k_z^2) + 4\Omega^2v_{Az}^2k_z^2(\omega^2 - c_s^2k_z^2), \quad (57)$$

where c_s is the isothermal sound speed of the medium, $\omega_A^2 \equiv \omega^2 - v_{Az}^2k_z^2$, and $f(\omega^2)$ is defined by

$$f(\omega^2) \equiv \omega^4 - \omega^2(c_s^2 + v_A^2)k_z^2 + c_s^2v_{Az}^2k_z^4.$$

Eq. (57) is a sixth-order equation for ω with only even terms. When $k_R = 0$, eq. (57) is identical to eq. (64) of Blaes & Balbus (1994) or eq. (99) of Balbus & Hawley (1998). Now let us take the two opposite limits of c_s to obtain the following dispersion relations

$$\omega_A^4 - (\kappa^2 + v_A^2k_R^2 + v_{A\phi}^2k_z^2)\omega_A^2 + (\kappa^2v_{A\phi}^2 - 4\Omega^2v_{Az}^2)k_z^2 = 0, \quad \text{for } c_s \rightarrow 0, \quad (58a)$$

$$(1 + k_R^2/k_z^2)\omega_A^4 - \kappa^2\omega_A^2 - 4\Omega^2v_{Az}^2k_z^2 = 0, \quad \text{for } c_s \rightarrow \infty, \quad (58b)$$

and the corresponding instability criteria⁴

$$v_{Az}^2(k_z^2 + k_R^2) + \kappa^2 - 4\Omega^2 \sin^2 i < 0, \quad \text{for } c_s \rightarrow 0, \quad (59a)$$

$$v_{Az}^2(k_z^2 + k_R^2) + d\Omega^2/d \ln R < 0, \quad \text{for } c_s \rightarrow \infty. \quad (59b)$$

⁴In fact, from eq. (57) the formal instability criterion (59b) is generic for any value of $c_s \neq 0$; it may be written as $v_{Az}^2(k_z^2 + k_R^2) + \kappa^2 - 4\Omega^2 < 0$. However, when $c_s/v_A \ll 1$, growth rates for small i are very low.

Note that eq. (58b) is the same as the original dispersion relation of the incompressible BH instability (eq. [2.9] of Balbus & Hawley 1991 without the Brunt-Väisälä frequency). The instability criterion (59a) in the extremely compressible limit depends explicitly on the local pitch angle, showing that as i departs from 90° the instability becomes gradually confined to smaller values of k_z . For a cold Keplerian flow, no instability occurs when i is smaller than 30° .

To examine what role thermal pressure plays to the growth of the BH instability and why the instability criterion depends on i , we plot the unstable solutions of eq. (57) as functions of $q_A \equiv (\mathbf{k} \cdot \mathbf{v}_A)/\Omega$ ($= k_z v_{Az}/\Omega$ for the axisymmetric case) and $\beta \equiv c_s^2/v_A^2$ in Fig. 9. For the time being, we confine our discussion to the $k_R = 0$ case. When $i = 90^\circ$, the instability criterion from eqs. (59a,b) is $v_A^2 k_z^2 < -d\Omega^2/d \ln R$ and the growth rate is independent of β , implying that the compressibility does not alter the instability (Fig. 9a). This can be understood as follows: when magnetic fields are mainly axial, sound waves propagating along a vertical direction decouple completely from the magnetic fields and are undisturbed by rotation. But transverse MHD waves which are intrinsically incompressible are influenced by rotation to become ultimately unstable for a range of k_z when $d\Omega/dR < 0$. Therefore, $i = 90^\circ$ is a very special case.

On the other hand, when both vertical and azimuthal fields are present, toroidal perturbed fields generated by an initial azimuthal displacement or by sheared motion following a radial perturbation of the initial axial fields tend to cause vertical oscillations, but in a cold assumption, mainly due to the magnetic field gradient terms, $-B_{0\phi}(\partial B_{1\phi}/\partial z)$. This oscillatory vertical motion tries to distribute the perturbed fields as uniformly as possible, thereby tending to suppress the growth of the disturbances. However, the vertical magnetic pressure gradients are not strong enough to create significant vertical motions if thermal pressure is large: a compressed region tends to expand vertically but with little change in the strength of the toroidal fields, thus providing a favorable condition for the development of the BH instability. This explains why higher β cases have higher growth rates at fixed i , and why the growth rate decreases as i decreases at fixed β (Fig. 9b~9d).

Although the instability criterion (59b) is completely independent of the strength of the azimuthal fields provided that $\beta \neq 0$, indicating as noted by Blaes & Balbus (1994) that to all orders, azimuthal fields do not modify the stability criterion, the corresponding growth rates drop progressively as β decreases if $i \neq 90^\circ$. When $\beta \gtrsim 1$, any change of an inclination angle i from 90° does not bring significant reductions in growth rates, implying that the characteristics of the instability are essentially the same as the pure poloidal case. If $\beta \ll 1$, however, we observe dramatic stabilizing effects from toroidal fields, as illustrated in Fig. 9.

A few comments should be devoted to the effect of k_R . Radial wave motions do nothing but add another restoring force to perturbations. This in turn means that thermal pressure has a stabilizing influence on the growth of the BH instability. Thus there are two competing processes of thermal pressure: thermal pressure associated with vertical wave motion promotes the BH instability, while thermal pressure controlling radial motion opposes it. It turns out that for $i \neq 90^\circ$ the former process always dominates. For $i = 90^\circ$, only the latter effect exists, giving higher growth rates for

smaller β , when $k_R \neq 0$.

Notice the stabilizing effect of k_R in eqs. (59). If the background vertical flow has significant shear, the local radial wavenumber would increase with time (cf. eq. [40]), suppressing the instability. Thus when $v'_{0z} \neq 0$, the compressible BH instability will exhibit a transient growth, as must happen to all modes if $k_z v'_{0z} \neq 0$ and/or $m\Omega' \neq 0$.

In conclusion, we have found that compressibility has a stabilizing effect on the axisymmetric BH instability. Even though its effect is small if the sound speed is super-Alfvénic, compressibility must be considered whenever the Alfvén speed is comparable to or even exceeds the thermal sound speed, as is expected in winds and also in disk coronae (cf. Miller & Stone 1999).

The above discussion applies only for axisymmetric perturbations. It was also found that an accretion disk with purely toroidal fields is subject to non-axisymmetric instability (Balbus & Hawley 1992; Terquem & Papaloizou 1996), but we will show in the following section that the physical role of compressibility in that case is completely different, in spite of the same quantitative instability criteria.

7.2. Non-Axisymmetric MRI: Coherent Wavelet Analysis

Balbus & Hawley (1992) found that a differentially rotating disk of incompressible fluid with embedded toroidal magnetic field is unstable to non-axisymmetric perturbations. Adopting shearing sheet coordinates (see below), they integrated a set of the perturbed equations and showed that perturbations with an intermediate azimuthal wavenumber m can exhibit transient, but enormous growth over a time scale of several percent of Ω^{-1} .

An alternative approach was taken by Terquem & Papaloizou (1996) to study a similar instability to that identified by Balbus & Hawley (1992). They solved the problem using the local WKB approximation. They started from a general compressible equation of state, but subsequently they supposed divergence-free poloidal Lagrangian displacements, which made their treatment essentially incompressible. They derived a sufficient condition for the instability which is exactly the same form as that of axisymmetric BH instability (i.e., $d\Omega^2/d\ln R < 0$). Noting that azimuthal shear is the main driving mechanism and bending of the field lines provides a stabilizing restoring force, they suggested the non-axisymmetric instability of toroidal magnetic fields might resemble the original BH instability.

We argue in this work that the underlying physical mechanisms for non-axisymmetric toroidal-**B** MRI (which we refer to as “NMRI”) and axisymmetric poloidal-**B** MRI (which we refer to as “BH”) are in fact quite different from each other. In this section, we analyze the NMRI by looking at “coherent wavelet” solutions in which every physical variable, localized in both space and time, oscillates or grows with the same space-time dependence, and provide quantitative results in detail.

7.2.1. Localization in Space and Time

We begin by considering a shearing, rotating disk with uniform density, and magnetic fields with only an azimuthal component. We ignore any unperturbed vertical motion in the medium. We include thermal pressure effects with an isothermal equation of state to obtain the explicit dependence of the NMRI on the temperature, but neglect effects of cylindrical geometry. This configuration is the same as Balbus & Hawley’s (1992), except that they considered only the incompressible case with the Boussinesq approximation, and allowed for vertical equilibrium gradients yielding buoyant oscillations. Adopting the shearing sheet coordinates $(\tilde{R}, \tilde{\phi}, \tilde{z})$ such that $\tilde{R} = R$, $\tilde{\phi} = \phi - \Omega(R)(t - t_o)$, and $\tilde{z} = z$ (Goldreich & Lynden-Bell 1965; Julian & Toomre 1966; Balbus & Hawley 1992), we consider the time development of an initial plane-wave disturbance which preserves sinusoidal variation in the local rest frame of the equilibrium shearing, rotating flow

$$\chi_1(R, \phi, z, t) = \chi_1(t) e^{im\tilde{\phi} + ik_z\tilde{z} + ik_R(t_o)\tilde{R}}, \quad (60)$$

where $k_R(t_o)$ is a radial wavenumber at a fiducial time $t = t_o$. The linearized form of the MHD eqs. (1)~(4), can be written in dimensionless form as

$$\frac{d\alpha}{d\tau} = -q_R u_{1R} - q_m u_{1\phi} - q_z u_{1z}, \quad (61)$$

$$\frac{du_{1R}}{d\tau} = 2u_{1\phi} - q_m b_R + q_R(\beta\alpha + b_\phi), \quad (62)$$

$$\frac{du_{1\phi}}{d\tau} = -\frac{\kappa^2}{2\Omega^2} u_{1R} + \beta q_m \alpha, \quad (63)$$

$$\frac{du_{1z}}{d\tau} = -q_m b_z + q_z(\beta\alpha + b_\phi), \quad (64)$$

$$\frac{db_R}{d\tau} = q_m u_{1R}, \quad (65)$$

$$\frac{db_\phi}{d\tau} = \frac{d \ln \Omega}{d \ln R} b_R - q_z u_{1z} - q_R u_{1R}, \quad (66)$$

$$\frac{db_z}{d\tau} = q_m u_{1z}, \quad (67)$$

where the dimensionless Lagrangian derivative is denoted by

$$\frac{d}{d\tau} = \frac{1}{\Omega} \frac{\partial}{\partial t} + \frac{\partial}{\partial \phi}. \quad (68)$$

In eqs. (61)~(68), all perturbed variables are dimensionless and defined by $\alpha \equiv \rho_1/\rho_0$, $\mathbf{u}_1 \equiv i\mathbf{v}_1/v_{A\phi}$, $\mathbf{b} \equiv \mathbf{B}_1/B_{0\phi}$, and $\tau \equiv t\Omega$, and dimensionless parameters are $\beta \equiv c_s^2/v_{A\phi}^2$, $q_m \equiv v_{A\phi}m/R\Omega$, $q_z \equiv v_{A\phi}k_z/\Omega$, and

$$q_R(\tau) \equiv \frac{v_{A\phi}k_R(t)}{\Omega} = \frac{v_{A\phi}}{\Omega} \left[k_R(t_o) - m(t - t_o) \frac{d\Omega}{dR} \right] = -mt \frac{v_{A\phi}}{\Omega} \frac{d\Omega}{dR} = -\tau q_m \frac{d \ln \Omega}{d \ln R}, \quad (69)$$

where the third equality holds when $t_o \equiv -k_R(t_o)/m\Omega'$. Eqs. (65)~(67) yield the divergence free condition for the perturbed magnetic fields.

Since q_R has a τ -dependence, the linear system of eqs. (61)~(67) does not form an eigenvalue problem; kinematics of shear wrap a given disturbance by increasing its radial wavenumber linearly with time. In the original shearing sheet formalism, the fate of a system exposed to perturbations is analyzed through direct integrations of linearized equations over time. In doing so, one may observe transient amplification or decay of applied disturbances depending on their stability. One can say that a system is unstable if some physical variables grow sufficiently over certain time scales. The efficiency of instability for a system is identified by computing the response of the system to variation of parameters input to temporal integrations. This approach was adopted by Balbus & Hawley (1992) in their identification of the NMRI.

Here, we instead analyze the NMRI by proceeding one more step from the original shearing sheet formalism to find solutions which are localized in time as well as in space. First, we note that there exist two distinct time scales: the growth time of instabilities determined by the inverse of the dimensionless instantaneous growth rate,

$$\gamma(\tau) \equiv \frac{d}{d\tau} \ln \chi_1(\tau) = \frac{1}{\Omega} \frac{d}{dt} \ln \chi_1(t), \quad (70)$$

and the dimensionless shearing time, $(d \ln q_R / d\tau)^{-1} = q_R |q_m d \ln \Omega / d \ln R|^{-1}$, as a typical time scale of the linear growth of the radial wavenumber. If the shearing time is much longer than the growth time, that is, if $q_m |d \ln \Omega / d \ln R| / (\gamma q_R) \ll 1$ (the “weak shear limit”), the time dependence of q_R in eq. (69) can be neglected, and thus normal mode solutions having an exponential or oscillatory behavior can be sought. Shu (1974) applied this technique to investigate the effects of a differential rotation on the Parker instability. Also, Ryu & Goodman (1992) obtained an algebraic dispersion relation for the convective instability in differentially rotating disks, by assuming that q_R is time-independent.

Because the convective and the Parker instabilities arise from hydrodynamic and magnetic buoyancy effects, respectively, independent of the rotation of a disk, one can always find a regime in which the weak shear limit is applicable. In some cases, however, as for example in the axisymmetric poloidal or the non-axisymmetric toroidal MRIs with weak magnetic fields, the instabilities result directly from a differential rotation with $\Omega' < 0$. In such cases, peak growth rates are of the same order as rotational frequencies (Balbus & Hawley 1998), and thus the weak shear is not a good approximation for these non-axisymmetric instabilities.

However, we can still look for coherent solutions in which *all* perturbed variables vary as $e^{\gamma\tau}$ with time, provided the variation of the instantaneous growth rate $\gamma(\tau)$ over the growth time γ^{-1} is relatively small, i.e.,

$$\left| \frac{d \ln \gamma(\tau)}{d\tau} \right| \ll \gamma(\tau). \quad (71)$$

We refer to the solutions under this approximation as “coherent wavelet solutions” because all physical quantities localized in both space and time grow at the same instantaneous rate. If the condition

(71) holds, the changes in $\gamma(\tau)$ can be neglected over a short time interval, and the set of dynamical equations (61)~(67) constitutes an eigensystem instantaneously. This is equivalent to the WKB method in the time dimension. Since $\gamma^{-1}d\ln\gamma(\tau)/d\tau = -q_m(d\ln\Omega/d\ln R)(d\ln\gamma/d\ln q_R)/(\gamma q_R)$, eq. (71) is satisfied if either $q_m|d\ln\Omega/d\ln R|/(\gamma q_R) \ll 1$ (the weak shear limit), or $|d\ln\gamma/d\ln q_R| \ll 1$ (instantaneous growth rates are relatively insensitive to the radial wavenumber); the condition (71) is less restrictive and in fact is the generalization of the weak shear limit. Of course, we need to check the self-consistency of this coherent wavelet approximation by examining *a posteriori* whether resulting solutions satisfy the condition (71). For incompressible media, Balbus & Hawley (1992) mapped the regime of instability in $[(\mathbf{k} \cdot \mathbf{v}_A)^2, |\mathbf{k}|/k_z]$ space using WKB methods similar to those we adopt.

7.2.2. Coherent Wavelet Dispersion Relation

Upon substituting eq. (70) into eqs. (61)~(67) and applying the approximation (71) so that $d\chi_1/d\tau \rightarrow \gamma\chi_1$, one can form a matrix equation $\gamma Q = \mathcal{M}Q$, where $Q = (\alpha, u_{1R}, u_{1\phi}, u_{1z}, b_R, b_\phi, b_z)^T$ is a column vector and \mathcal{M} is a 7×7 matrix whose components are determined by the coefficients of Q in the right hand sides of eqs. (61)~(67). By solving the condition $\det(\mathcal{M} - \gamma\mathcal{I}) = 0$, where \mathcal{I} is the identity matrix, we obtain a seventh order polynomial in γ . As a further approximation, however, if at least one of the conditions, $q_z \gg q_R$, $\gamma \gg \tau$, or $\gamma\tau \gg 1$, is satisfied, all even order terms that depend linearly on τ and q_m but are independent of q_z , can be neglected compared to the remaining terms. The first two conditions apply when the radial wavenumber is not significant, either because disturbances are highly localized in the vertical direction ($q_z \gg q_R$) or simply because we are looking at modal behaviors at the time $\tau \sim 0$, while the third condition holds when net amplification of perturbations is large. This simplification yields a trivial solution $\gamma = 0$ (this arises from the fact that perturbed magnetic fields, b_R , b_ϕ , and b_z , are linearly dependent via the divergence-free condition) and a third-order polynomial in γ^2 which is the resulting instantaneous dispersion relation for NMRI

$$0 = \gamma^6 + \gamma^4 \left[(1 + \beta)q^2 + q_m^2 + \frac{\kappa^2}{\Omega^2} \right] + \gamma^2 \left[(1 + 2\beta)q^2 q_m^2 + \frac{\kappa^2}{\Omega^2}(q_m^2 + (1 + \beta)q_z^2) \right] + \beta q_m^2 \left[q^2 q_m^2 + \frac{d\ln\Omega^2}{d\ln R} q_z^2 \right], \quad (72)$$

where the amplitude of the total wavenumber defined by $q^2(\tau) \equiv q_R(\tau)^2 + q_m^2 + q_z^2$ is a function of τ through eq. (69). Combining eqs. (69) and (72), one can evaluate a local, instantaneous growth rate at a given time.

With vanishing magnetic fields and thermal pressure, we would obtain from eq. (72) stable epicyclic oscillations. In the limit of strong magnetic fields and no rotation, eq. (72) is immediately reduced to $(\gamma^2 + q_m^2)(\gamma^4 + (1 + \beta)q^2\gamma^2 + \beta q_m^2 q^2) = 0$, the usual dispersion relations for the Alfvén waves and the fast and slow MHD waves in a medium embedded with toroidal magnetic fields. In the

presence of rotation with non-vanishing but weak fields, however, these Alfvén and MHD modes are coupled to exhibit generally complex modal behaviors. They can be stable or unstable depending on the parameters, but it is always a slow MHD wave that becomes unstable because it has the lowest frequency so that there is a plenty of time during which destabilizing forces (centrifugal forces for NMRI) act on it. We have instantaneously growing solutions with real positive values of γ provided that the last term in eq. (72) is negative. Thus, when $\beta q_m \neq 0$, the local, instantaneous instability criterion in terms of the dimensionless variables for the NMRI can be written

$$q_m^2 \left(1 + \frac{q_R(\tau)^2 + q_m^2}{q_z^2} \right) + \frac{d \ln \Omega^2}{d \ln R} < 0, \quad (73)$$

demonstrating that $d\Omega^2/d \ln R = \kappa^2 - 4\Omega^2 < 0$ is indeed a sufficient condition for the instability to arise when the magnetic field strength is negligible (Balbus & Hawley 1992; Foglizzo & Tagger 1995; Terquem & Papaloizou 1996). Eq. (73) recovers the results of Balbus & Hawley (1992) for the instability regime for toroidal-field NMRI. The result of eq. (73) can be compared to the poloidal-field BH instability criterion of eq. (59b). Notice that the NMRI (with $B_{0z} = 0$) vanishes completely as $\beta \rightarrow 0$, while the axisymmetric BH instability still exists even when $\beta = 0$ (see §7.1).

Although they share the same instability criterion, the operating mechanisms for the NMRI of toroidal fields are quite different from the axisymmetric BH instability of poloidal fields. Both arise via destabilization of the slow mode. The NMRI mode, just as the poloidal BH mode, depends on shear to generate azimuthal fields from radial perturbations of the background fields. But there is more to the story. The key mechanism for the NMRI instability lies in the vertical MHD wave motions driven by the gradient of the total (initial plus perturbed) azimuthal fields, as schematically illustrated in Fig. 10. Since we suppose perturbations which are sinusoidal in both vertical and azimuthal directions, the perturbed azimuthal fields are also periodic in both directions. Rapid vertical motions with high k_z , generated by $-B_{0\phi}(\partial B_{1\phi}/\partial z)$ stress, would produce over- and under-dense regions which regularly alternate along the azimuthal direction (Fig. 10a). And then, azimuthal fluid motions are induced, according to the equation of continuity, from over-dense regions to under-dense regions (Fig. 10b). Depending on the direction ($\mp \hat{\phi}$) of these induced motions, the coriolis and/or centrifugal force would alter the paths, radially inward or outward (Fig. 10c). Under the condition of field freezing, these radial motions would produce radial magnetic fields with a small amplitude from the background toroidal fields (Fig. 10d). These radial fields would in turn be sheared out to generate (positive or negative) perturbed azimuthal fields, due to the differential rotation of the background flows. When $d\Omega/dR < 0$, the resulting azimuthal fields from initial and perturbed ones would be distributed (Fig. 10e) such that they reinforce the applied initial vertical perturbations (Figs. 10a and 10f), implying the MRI; the entire system would just oscillate with rotation-modified MHD frequencies if $d\Omega/dR > 0$. This explains how the NMRI operates.

When k_z is large, the stabilization of the NMRI occurs when a magnetic tension from radially bent field lines exceeds the centrifugal or coriolis force (Figs. 10b and 10c). Shear Alfvén waves with radial polarization can suppress the instability if the field lines are sufficiently strong or if the azimuthal wavenumber is large enough, as expressed by the dimensionless parameter q_m^2 outside

the parentheses in eq. (73). When $q_z \ll q_R$, on the other hand, MHD waves propagating along the radial direction stabilize the NMRI, as indicated by the terms inside parentheses in eq. (73); $q_R(\tau)$ clearly reflects the stabilizing effect of the background shear.

The maximum instantaneous growth rate is achieved when $q_R \approx 0$. In this case, eq. (73) implies instability if

$$q_m^2 < q_{m,\text{crit}}^2 \equiv \frac{1}{2} \left[-q_z^2 + \sqrt{q_z^4 - 4q_z^2 \frac{d \ln \Omega^2}{d \ln R}} \right].$$

Note that $q_{m,\text{crit}}^2 \rightarrow -d \ln \Omega^2 / d \ln R$, for $q_z \gg 1$, while $q_{m,\text{crit}}^2 \rightarrow q_z \sqrt{-d \ln \Omega^2 / d \ln R}$, for $q_z \ll 1$. Numerical solutions of eq. (72) with $q_R = 0$ are presented in Fig. 11. As both eq. (73) and Fig. 11 show, the maximum growth rates for toroidal-field background states are attained when $q_z \rightarrow \infty$, which is a sharp contrast to the axisymmetric poloidal-field BH instability that has fastest growing mode at moderate q_z 's (cf. Fig. 9 and see also discussion in Balbus & Hawley 1998). But both forms of the MRI have the same maximum growth rates at the same $q_A \equiv (\mathbf{k} \cdot \mathbf{v}_A) / \Omega$. Fig. 11b shows how growth rates depend on the sound speed. As the sound speed increases, the medium becomes more unstable. This reflects the incompressible nature of the NMRI. Even though the marginally critical wavenumber is independent of temperature (for $\beta \neq 0$), the virulence of the instability is greatly inhibited as β decreases. For $q_m \ll 1$, one can find from eq. (72) the temperature dependence of the limiting growth rate

$$\gamma = q_m \sqrt{-\frac{\beta}{\kappa^2(1+\beta)} \frac{d\Omega^2}{d \ln R}}, \quad (74)$$

or $\gamma = q_m \sqrt{3\beta/(1+\beta)}$ for a Keplerian rotation. Eq. (74) gives slopes of the growth rates for small q_m (Fig. 11). For magnetocentrifugally driven winds which are as cold as $\beta < 0.01$, the NMRI is not expected to play a significant role; the growth rate in dimensional units is $\sqrt{3}c_s m/R$.

When the medium is incompressible ($\beta \rightarrow \infty$), eq. (72) allows the analytic expression for the instantaneous growth rate for pure toroidal-field background states,

$$\gamma^2 = \begin{cases} \frac{q_z^2}{2q^2} \frac{\kappa^2}{\Omega^2} \left[\sqrt{1 + 16 \frac{q^2 q_m^2}{q_z^2} \frac{\Omega^4}{\kappa^4}} - 1 \right] - q_m^2, & \text{if } \frac{q^2 q_m^2}{q_z^2} + \frac{d \ln \Omega^2}{d \ln R} < 0, \\ 0. & \text{otherwise,} \end{cases} \quad (75)$$

When $q_z \gg 1$, one can derive the maximum growth rate $\gamma_{\text{max}} = |d \ln \Omega / d \ln R| / 2$, which is achieved when $q_{m,\text{max}}^2 = -(d \ln \Omega^2 / d \ln R) / 2 - \gamma_{\text{max}}^2$. It can be shown from eq. (72) or (75) that $d\gamma^2/d\tau \sim q_m^3 q_R / q^2 \rightarrow 0$ as $q_z \rightarrow \infty$. This proves that the coherent wavelet approximation is self-consistent for the NMRI with high q_z .

7.2.3. Comparison With the Shearing Sheet Formalism

In order to compare the coherent wavelet solutions for toroidal-field NMRI with the results from the shearing sheet approximation, we directly integrate eqs. (61)~(67) over time, with given

sets of initial conditions. In Fig. 12, we display the time evolution of all perturbed variables for $q_m = 0.1$, $q_z = 1$, and $\beta = 100$, which are the same parameters as chosen for Fig. 3 of Balbus & Hawley (1992). We adopt a Keplerian rotation profile in what follows. The initial amplitudes are 0.1 for every variable except $b_R = 0.01$ and $b_z = 0.4$, and the initial $\tilde{\tau}$, where the orbit number $\tilde{\tau} \equiv \tau/2\pi = t\Omega/2\pi$, is allowed to be determined from the divergence free condition of the initial, perturbed magnetic fields. When $\tilde{\tau} < -20$, the system responds with MHD wave motions before they start to grow. During this relaxation stage, fast MHD modes having large $|q_R|$ are nearly longitudinal acoustic waves, affecting u_{1R} and α , while $u_{1\phi}$ and b_ϕ are mostly influenced by transverse slow modes. As time increases, $|q_R|$ gradually decreases, permitting rotational shear to affect the overall dynamics. Once the condition (73) is satisfied, shear drives the slow modes to be unstable, following the process illustrated in Fig. 10. Even though the growth of disturbances shows a transient nature due to the kinematic growth of q_R , the net amplification is about 9 orders of magnitude, a bit higher than Balbus & Hawley’s result. This is because the integration interval in Balbus & Hawley covered a slightly smaller part of the unstable time range. At later time when q_R has a large value, the system exhibits stable oscillations with the slow MHD wave frequency. Fig. 12 also shows the predicted amplification magnitude (thick solid line) from the coherent wavelet approximation (see below).

In Fig. 13, we plot the numerical growth rates for each variable calculated from Fig. 12 based on the direct numerical integrations in the shearing sheet formalism, together with the growth rate of the corresponding coherent wavelet solution. Here, a dimensionless instantaneous growth rate $\tilde{\gamma}$ as a function of $\tilde{\tau}$ is defined through $10^{\tilde{\gamma}\tilde{\tau}} = e^{\gamma\tau}$, (or $\tilde{\gamma}(\tilde{\tau}) = 2\pi\gamma(\tau) \log e$). Note that the heavy solid line for $\tilde{\gamma}$ drawn from eq. (72) fits well with various curves computed from the direct numerical integrations. The instantaneous growth rates are almost symmetric with respect to their maxima near $\tilde{\tau} = 0$, as expected. Growth of the modes occurs only when $|\tilde{\tau}| < 18.3$, which is in good agreement with the results of the direct integrations, demonstrating the validity of the coherent wavelet approximation.

We define a dimensionless amplification magnitude as

$$\Gamma(\tilde{\tau}) \equiv \int_{-\infty}^{\tilde{\tau}} \tilde{\gamma}(\tilde{\tau}') d\tilde{\tau}' = \log e \int_{-\infty}^{\tau} \gamma(\tau') d\tau'. \quad (76)$$

Then, $\Gamma(\tilde{\tau})$ is an order of magnitude measurement of the amplification of an unstable mode during the time interval $(-\infty, \tilde{\tau})$. The total amplification is given by $10^{\Gamma(\infty)}$. When eq. (75) is substituted, the analytic evaluation of the integral in eq. (76) is not an easy task. In view of a shape of $\tilde{\gamma}(\tilde{\tau})$ (Fig. 13), we further approximate $\tilde{\gamma}$ with a simple form

$$\tilde{\gamma} = \begin{cases} \tilde{\gamma}_o(1 - |\tilde{\tau}|/\tilde{\tau}_c)^{1-q_m/2}, & \text{if } |\tilde{\tau}| < \tilde{\tau}_c, \\ 0, & \text{otherwise,} \end{cases} \quad (77)$$

where

$$\tilde{\gamma}_o \equiv \sqrt{2\pi} \log e \left\{ \frac{q_z^2}{q_m^2 + q_z^2} \frac{\kappa^2}{\Omega^2} \left[\sqrt{1 + 16 \frac{(q_m^2 + q_z^2) q_m^2 \Omega^4}{q_z^2 \kappa^4}} - 1 \right] - 2q_m^2 \right\}^{1/2}, \quad (78a)$$

and the termination epoch of growth $\tilde{\tau}_c$ is defined by

$$\tilde{\tau}_c \equiv \frac{1}{2\pi q_m} \left| \frac{d \ln \Omega}{d \ln R} \right|^{-1} \sqrt{- \left(\frac{d \ln \Omega^2}{d \ln R} \right) \frac{q_z^2}{q_m^2} - q_m^2 - q_z^2}. \quad (78b)$$

Notice that eq. (77) is valid only if $\tilde{\tau}_c$ is real, that is, only if the condition (73) is satisfied. From eqs. (76) and (77), the total amplification magnitude is easily found to be

$$\Gamma(\infty) = \frac{4\tilde{\gamma}_o \tilde{\tau}_c}{4 - q_m}, \quad (79)$$

which is illustrated with solid contours in Fig. 14. Also shown with dotted contours are the direct results from numeral integration of eq. (75), which are in excellent agreement with $\Gamma(\infty)$. The thick contour is the locus of $\tilde{\tau}_c = 0$, demarcating the stable and unstable regions: the system is stable at the right hand side of the thick contour. In the $q_m - q_z$ plane, the total amplification tends to be greater as q_z becomes larger and as q_m becomes smaller. This is because the NMRI with $B_{0z} = 0$ acquires maximum instantaneous growth rates at $q_z = \infty$ (Fig. 11a) and because the shearing time is longer with smaller q_m (cf. eq. [78b]). For comparison, we also include in Fig. 14 the results from the shearing sheet equations for four parameter sets: $(q_m, q_z) = (0.03, 0.1), (0.1, 1), (1, 10),$ and $(\sqrt{2}, 100\sqrt{2})$, and $\beta=100$ for all cases: these are marked with dots on $q_m - q_z$ plane, labeled by the respective exact and estimated (in parentheses) amplification magnitudes. Note that all of the estimated amplification magnitudes are within 5% of the results of direct shearing sheet integrations. This indicates that eq. (79) is an excellent analytic estimate for the amplifications of incompressible NMRI modes.

7.3. Generalized MRI

Motivated by the success of the coherent wavelet method in finding the solutions of the NMRI with purely toroidal background fields, we now generalize both the axisymmetric BH and NMRI instabilities by considering non-axisymmetric perturbations applied to the rotating medium threaded by both vertical and azimuthal magnetic fields. We include the effect of thermal pressure and allow the angular velocity Ω to be a function of R , but ignore any other radial variations in the initial state. We adopt the shearing sheet coordinates as before, and linearize eqs. (1)~(4). After applying perturbations in the form of eq. (60), we assume that the perturbations evolve with time as $e^{\gamma(t)t}$ with the coherent wavelet condition (i.e., $d \ln \gamma(t)/dt \ll \gamma(t)$). Following the same procedure as §7.2, we obtain the general instantaneous dispersion relation for the MRI (now written in dimensional form)

$$\begin{aligned} 0 = & \gamma^6 + \gamma^4 [(c_s^2 + v_A^2)k^2 + \kappa^2 + (\mathbf{k} \cdot \mathbf{v}_A)^2] \\ & + \gamma^2 \left[(2c_s^2 + v_A^2)(\mathbf{k} \cdot \mathbf{v}_A)^2 k^2 + \kappa^2 \left(c_s^2 k_z^2 + v_{A\phi}^2 \left(\frac{m^2}{R^2} + k_z^2 \right) \right) + (\mathbf{k} \cdot \mathbf{v}_A) k_z v_{Az} \frac{d\Omega^2}{d \ln R} \right] \\ & + c_s^2 (\mathbf{k} \cdot \mathbf{v}_A)^2 \left[(\mathbf{k} \cdot \mathbf{v}_A)^2 k^2 + \frac{d\Omega^2}{d \ln R} k_z^2 \right], \end{aligned} \quad (80)$$

where $k^2 \equiv k_R^2(t) + m^2/R^2 + k_z^2$ with the radial wavenumber defined by $k_R(t) = -mtd\Omega/dR$ when we choose $t_o = -k_R(t_o)/m\Omega'$. When either $m = 0$ (axisymmetric case) or $v_{Az} = 0$ (pure toroidal field case), eq. (80) becomes identical respectively with eq. (57) for the BH modes or eq. (72) for the NMRI modes.

From eq. (80), we obtain the instantaneous instability criteria for the generalized MRI modes

$$v_A^2 k^2(t)(\mathbf{k} \cdot \mathbf{v}_A)^2 + \kappa^2 v_{A\phi}^2 \left(\frac{m^2}{R^2} + k_z^2 \right) + (\mathbf{k} \cdot \mathbf{v}_A) v_{Az} k_z \frac{d\Omega^2}{d \ln R} < 0, \quad \text{for } c_s = 0, \quad (81a)$$

$$(\mathbf{k} \cdot \mathbf{v}_A)^2 \left(1 + \frac{k_R^2(t) + m^2/R^2}{k_z^2} \right) + \frac{d\Omega^2}{d \ln R} < 0, \quad \text{for } c_s \neq 0, \quad (81b)$$

which are obviously the generalizations of eqs. (59) and (73). It can also be shown that when $i = 90^\circ$, both equations (81a) and (81b) become identically $v_{Az}^2(k_R^2(t) + m^2/R^2 + k_z^2) + d\Omega^2/d \ln R < 0$. With an $\Omega \propto R^{-a}$ rotation profile, eq. (81a) gives the sufficient condition for the instability in an extremely cold medium: $\sin i > (4 - 2a)/(4 - a)$. Keplerian flows for example become unstable only if $i \gtrsim 24^\circ$, indicating that cold, B_ϕ -dominated media are not subject to the generalized non-axisymmetric MRI disturbances, just as we found earlier that axisymmetric BH modes are also stable in cold flows for small i . We remark that the case with $a \rightarrow 2$, as potentially possible in MHD winds from boundary layers, can just barely satisfy the cold medium instability criterion for $i \rightarrow 0$. Note that unlike the NMRI mode with $v_{Az} = 0$, maximum growth rates in the $c_s \neq 0$ case are not achieved as $k_z \rightarrow \infty$. In fact, high- k_z or high- m disturbances are efficiently stabilized by Alfvén and/or MHD waves whenever *both* poloidal and toroidal fields are present. However small they may be, therefore, inclusion of poloidal fields would yield a different result from the case with pure toroidal fields (this point was previously noted by Balbus & Hawley 1998). Again the stabilizing effect of kinematic shear appears through the time dependence of $k_R^2(t)$, when $m \neq 0$.

Fig. 15a shows how the compressible BH modes are stabilized by azimuthal magnetosonic waves. Here, we confine consideration to the radial wavenumber $k_R = 0$. As $q_m (= v_A m/R\Omega)$ increases, both the growth rates and the ranges in $q_z (= v_A k_z/\Omega)$ of unstable modes decrease. This is because if $q_m \neq 0$, azimuthally displaced material feels relatively stronger restoring forces due to both thermal and magnetic pressures of the medium as well as stronger tension forces from bent field lines. Non-axisymmetric poloidal-field BH instability modes become stabilized with increasing values of m . When $q_m > \sqrt{-d \ln \Omega^2/d \ln R}$ ($= \sqrt{3}$ for a Keplerian rotation), the instability is strictly cut off, even when the effect of kinematic shear is not taken into account.

We remark that the role of temperature of the medium to the BH instability is different between axisymmetric (with $q_m = 0$ and $i \neq 90^\circ$; see Fig. 9) and non-axisymmetric (with $q_m \neq 0$ and $i = 90^\circ$; see Fig. 15) cases. When $i = 90^\circ$, as already explained in §7.1, the axisymmetric BH instability with $q_m = 0$ is independent of β , because only Alfvén and sound waves exist and they do not interact with each other. When $q_m = 0$ and $i \neq 90^\circ$, magnetic pressure induces vertical MHD wave motions which tend to stabilize the system when β is small. If $\beta \gg 1$, however, the vertical wave motions become nearly acoustic, leaving the toroidal component of perturbed fields

unaffected and permitting higher growth rates. When $q_m \neq 0$ and $i = 90^\circ$, on the other hand, the coupling of thermal pressure with magnetic pressure occurs through azimuthal MHD motions, and the growth rate depends only weakly on β .

Fig. 15b shows loci of equi-growth rate on the $q_z - q_m$ plane for $i = 10^\circ$ and $\beta = 0.01$ (dotted contours) and $\beta = 100$ (thin solid contours). For $0 < q_m < 1.17$, there exist upper and lower critical vertical wavenumbers, $q_{z,u}$ and $q_{z,l}$ such that the system is unstable with $q_{z,l} < q_z < q_{z,u}$. When $q_z > q_{z,u}$, disturbances are stabilized by MHD waves propagating mainly along vertical direction, while perturbations with $q_z < q_{z,l}$ approach stable Alfvén waves. Each contour has a slope of $\sim -\tan i$ ($= -0.18$ for $i = 10^\circ$) at both ends. Note that dotted contours with lower β are labeled with much smaller growth rates than solid ones with higher β , even though they are similar in shape. Compared to Fig. 9 or Fig. 15a, this implies that the NMRI instability with a toroidal field configuration is more sensitive to temperature than the axisymmetric/non-axisymmetric BH instability with poloidal fields.

When $\beta \rightarrow \infty$, from eq. (80) we have the instantaneous growth rates for the generalized MRI modes

$$\gamma^2 = \frac{\kappa^2 k_z^2}{2k^2} \left[\sqrt{1 + 16(\mathbf{k} \cdot \mathbf{v}_A)^2 \frac{k^2 \Omega^2}{k_z^2 \kappa^4}} - 1 \right] - (\mathbf{k} \cdot \mathbf{v}_A)^2, \quad (82)$$

for $(\mathbf{k} \cdot \mathbf{v}_A)^2 k^2 / k_z^2 + d\Omega^2 / d \ln R < 0$, which is also a generalization of eq. (75). With weak magnetic field strength, one can show from eq. (82) that $\gamma^{-3} d\gamma^2 / dt \sim -mk_R(\mathbf{k} \cdot \mathbf{v}_A) / (\Omega k_z^2) \rightarrow 0$ as $(\mathbf{k} \cdot \mathbf{v}_A) / \Omega \rightarrow 0$. Thus, we see that for the generalized MRIs, the coherent wavelet approach is self-consistent in the weak field limit. When the field strength is moderate, on the other hand, we obtain $d\gamma^2 / dt \sim m\Omega' k_R (\mathbf{k} \cdot \mathbf{v}_A)^2 / k^2$. Since $\gamma \sim \Omega \sim (\mathbf{k} \cdot \mathbf{v}_A)$ in this case, the coherent wavelet condition is met only when $m|\Omega'| \ll k_R \gamma$ (the weak shear limit). Of course, the predominantly toroidal-field case that becomes unstable with $k_z \gg 1$ also satisfies the coherent wavelet condition, since k^2 becomes arbitrarily large without increasing the $(\mathbf{k} \cdot \mathbf{v}_A)$ -term, as discussed in §7.2.2.

Comparing eq. (75) with eq. (82), we note that the incompressible MRI can be generalized simply by replacing the dimensionless azimuthal wavenumber q_m with $(\mathbf{k} \cdot \mathbf{v}_A) / \Omega$. Therefore, we can write the net amplification magnitude for the generalized incompressible MRI as

$$\Gamma(\infty) = \frac{4 \log e}{4 - q_A} \gamma_0 t_c \quad (83)$$

where the dimensional peak growth rate γ_0 and the cut-off time of the instability t_c are defined by

$$\frac{\gamma_0^2}{\Omega^2} \equiv \frac{\kappa^2 \cos^2 \theta}{2\Omega^2} \left[\sqrt{1 + 16 \frac{q_A^2}{\cos^2 \theta} \frac{\Omega^4}{\kappa^4}} - 1 \right] - q_A^2 \quad (84)$$

and

$$t_c \equiv \frac{1}{\sin \theta} \left| \frac{d\Omega}{d \ln R} \right|^{-1} \sqrt{-\frac{d \ln \Omega^2 \cos^2 \theta}{d \ln R} \frac{q_A^2}{\kappa^4}} - 1, \quad (85)$$

respectively. The net amplification can thus be completely determined by the two parameters: the dimensionless wavenumber $q_A \equiv (\mathbf{k} \cdot \mathbf{v}_A)/\Omega$ projected in the direction of initial equilibrium magnetic fields, and the angle $\theta \equiv \tan^{-1}(m/Rk_z)$ of the wavenumber vector with respect to the vertical axis. Note that $\gamma_o \rightarrow 0$ with vanishing q_A , while $t_c \rightarrow \infty$ as $\theta \rightarrow 0$, indicating that low- m instabilities show higher net amplifications than high- m disturbances as long as $q_A \neq 0$. The total amplification magnitudes, eq. (83), are plotted in Fig. 16 with thin solid contours. For comparison, we also plot the numerical results from eqs. (76) and (82) with dotted contours. We assume a Keplerian rotation profile. The heavy curve with $q_A^2 = 3 \cos^2 \theta$ draws the locus of the marginal stability. In the limit of a weak magnetic field strength (i.e., $q_A \rightarrow 0$), it can be shown from eqs. (83)~(85) that $\Gamma(\infty) = (2 \log e)\Omega/(\kappa \tan \theta)$, inversely proportional to θ (for $\theta \ll 1$) but independent of q_A , as illustrated in Fig. 16. Also shown in Fig. 16 are the results from the direct temporal integrations of shearing-sheet equations with $\beta = 100$ as filled circles (for $i = 90^\circ$), filled triangles (for $i = 30^\circ$), and open circles (for $i = 0^\circ$), labeled by the respective exact and estimated (in parentheses) amplification magnitudes. These two results agree very well, implying that the coherent wavelet approach indeed provides excellent approximations to the solutions for amplification of generalized MRIs.

From Fig. 16, it is apparent that it is the locally near-axisymmetric (in the sense $m/Rk_z = \tan \theta \ll 1$) disturbances that experience maximum amplification, with the amplification magnitude only weakly dependent on $q_A = (\mathbf{k} \cdot \mathbf{v}_A)/\Omega$ within the unstable regime ($q_A \lesssim 1$). The increase in amplification factor with Rk_z/m predicted from linear theory may in part explain the larger amplitudes of power spectra for modes with larger $\hat{\mathbf{k}} \cdot \hat{\mathbf{z}}$ measured from nonlinear simulations of the saturated MRI (cf. Hawley, Gammie, & Balbus 1995). In addition, for the case of pure toroidal fields, Fig. 16 suggests only low amplification factors unless k_z is very large, which may help explain why Hawley, Gammie, & Balbus (1995) found lower magnetic field saturation amplitudes in cases with initial $B_z = 0$.

8. Summary and Discussion

8.1. General Conclusions Based on Linearized Analysis

Through linear analyses of the ideal MHD equations, we have explored the stability of shearing, rotating flows to a wide range of (primarily local) disturbances. The chief motivation for this study is to characterize the internal instabilities that could develop in disk winds that emanate from an extended region of a differentially rotating protostellar disk around a young star. The dynamics of such winds has inspired intensive theoretical effort because they may be responsible for observed YSO jets and outflows. In our analysis, we include both results based on generic density, magnetic field, and flow profiles, and results which adopt as initial equilibrium configurations the power-law asymptotic solutions of self-confined cylindrically symmetric winds presented by Ostriker (1997): $\rho \propto R^{-q}$, $B_\phi \propto B_z \propto R^{-(1+q)/2}$, and $v_\phi \propto v_z \propto R^{-1/2}$. For most of our analysis

(§§2-6), the flows were assumed to be cold enough that thermal effects can be ignored compared with magnetic forces. To make contact with other studies of shear-induced MHD instabilities in rotating disks, we also consider stability of specific models which include non-zero thermal pressure (§7). For the lowest-order “fundamental” modes, we employ a normal-mode analysis with free Lagrangian boundary conditions to find eigenvalues and eigenfunctions of both stable and unstable modes (§3). For higher-order modes, we employ three different local techniques to study growth of unstable disturbances: In §§4-6, we present numerical and analytic solutions of dispersion relations obtained from normal mode analyses in the $Rk_R \gg 1$ WKB limit. These are exact for $m\Omega' + k_z v'_{0z} = 0$ disturbances and are valid for a limited time for weakly-shearing circumstances where $k_R \gg m|\Omega'/\Omega|, k_z|Rv'_{0z}/v_{0z}|$ (see also §8.2 below). In §7, we employ temporal integrations of the shearing-sheet equations to study MRI modes (which are cut off for $Rk_R \gg 1$). We also introduce, in §7.2, a “coherent wavelet” formalism which adapts modal analyses for situations where shear is considerable (i.e., small Rk_R/m); the coherent wavelet analysis is equivalent to a WKB approach in the temporal domain. We include a comparison of results from the shearing-sheet and coherent-wavelet techniques applied to MRIs, in §7.2.3.

Applying these techniques we have identified a total of nine different unstable or overstable families of disturbances that occur for a wide range of flow parameters: five (FM, BH, ATB, PB, and TR) of them are axisymmetric and the other four (NTB, GPB, PR, and NMRI) are non-axisymmetric. Table 1 summarizes the properties of these modes. The main general conclusions drawn from the analysis in this work can be summarized as follows:

(1) Systems having a primarily azimuthal magnetic field, for example, disk winds far from their source, are susceptible to the fundamental (FM), axisymmetric (ATB) and non-axisymmetric (NTB) toroidal buoyancy, non-axisymmetric magnetorotational instability (NMRI) and toroidal resonance (TR) modes. Unstable fundamental modes (see §3.2) are concentrated in the central parts of jets, and occur in B_ϕ -dominated flows when the logarithmic gradient of the magnetic field is steeper than ≈ -0.75 (cf. eqs. [24] and [25]). Growth rates of unstable FM are comparable to inner-wind Alfvén frequencies. Long wavelength modes with large amplitudes at large radii are all stable, for power-law wind profiles. The TR mode (see §6.1.4) is an overstability, with growth suppressed when k_R increases through shear of the vertical velocity, simply becoming oscillatory MHD waves. The axisymmetric toroidal buoyancy mode (ATB; §6.1.2) is activated initially by the buoyancy force and subsequently by bending poloidal magnetic fields. In geometrical form, it is locally similar to the sausage mode of a plasma column confined by toroidal fields, and leads to radial mixing. Because growth rates are larger on smaller scales, ATB can contribute to the generation of local turbulence in disk winds. The non-axisymmetric toroidal buoyancy mode (NTB; see §6.2.1) is much like the Parker instability, but with the centrifugal force replacing the role of external gravity. Although the normal-mode analysis for NTB has the largest temporal validity at small m/Rk_R , the instantaneous growth rate increases with increasing m/Rk_R (cf. eq. [52] and Fig. 8c). We thus return to the NTB in §8.2, below, applying time-dependent techniques to study the $Rk_R/m \ll 1$ limit. Because the NTB is present whenever radial magnetic forces are non-zero, it

may be important in promoting radial mixing. Both of the toroidal buoyancy instabilities require non-zero magnetic forces in the equilibrium state. The rarefied and cold conditions of disk winds do not favor the development of the NMRI (see §7.2.2 and §7.3). Like the original (poloidal field) magnetorotational (BH) instability, NMRI requires $d \ln \Omega^2 / d \ln R < 0$, but also requires a relatively incompressible medium, as is provided by the relatively dense and warm ($c_s \gtrsim v_A$) conditions in an accretion disk. We show the NMRI vanishes in the limit of $c_s/v_A \rightarrow 0$. We further discuss perturbations in cold, B_ϕ -dominated flows in §§8.2 and 8.3, below.

(2) Systems having primarily axial magnetic fields, for example, accretion disks or winds very near their origin, are susceptible to the Balbus-Hawley (BH), poloidal buoyancy (PB and GPB), and poloidal resonance (PR) modes. The well-known axisymmetric Balbus-Hawley instability (BH; see §6.1.3 and §7.1) is the most efficient member of the family of magnetorotational instabilities (MRIs; see §7.3). It will work to produce channel flows, eventually generating fully-developed MHD turbulence through coupling to non-axisymmetric disturbances in the non-linear stage. Driven by background magnetic pressure and the centrifugal force, the axisymmetric poloidal buoyancy mode (PB; see §6.1.1) requires a gradient in the magnetic field strength to be unstable. If the field distribution is steep enough, the poloidal buoyancy modes would also work effectively to generate radial mixing and turbulence over much smaller scales than the BH instability. Because of their overstable characteristics, the impact on the system of poloidal resonance modes (PR; see §6.2.3) would be best evaluated with a global rather than local formalism. Configurations with shallower background magnetic gradients ($q < 1$) are also subject to a non-axisymmetric poloidal buoyancy instability (GPB; see §6.2.2) which arises in part from geometric effects.

(3) In distinction to the original, incompressible, axisymmetric BH instability, we found that the compressible axisymmetric BH mode is strongly stabilized by the presence of an azimuthal magnetic field if the medium has substantially sub-Alfvénic sound speeds. For example, in a cold rotating flow with $\Omega \propto R^{-3/2}$, the axisymmetric BH instability would be completely suppressed if the local pitch angle $i \equiv \tan^{-1}(B_z/B_\phi)$ is less than 30° (cf. eq. [47]). In an incompressible medium (as provided by a disk with $c_s \gtrsim v_A$), faster sound waves preserve perturbed toroidal fields from being dispersed by MHD wave motions, thereby providing a favorable condition for the BH instability. When the field configuration is purely poloidal, the compressible BH instability is identical with its incompressible counterpart, independent of temperature (cf. eqs. [58] and [59]).

(4) Even though they share the same instability criterion (cf. eqs. [59b] and [73]), the operating mechanisms for the NMRI of purely toroidal \mathbf{B} -fields is entirely different from the axisymmetric BH instability of primarily poloidal \mathbf{B} -fields. In the NMRI (see §7.2), vertical MHD wave motions driven by magnetic pressure play an essential role in the feedback loop for induced radial disturbances, while the axisymmetric BH instability tends to be stabilized by vertical wave motions. Faster sound speeds produce higher growth rates in both instabilities, but for different reasons: in the NMRI by activating azimuthal fluid motions preceded by the vertical MHD wave motions; in the BH instability by maintaining the perturbed azimuthal fields generated by shear (when $B_{0\phi} \neq 0$). Because of their non-axisymmetric nature, the NMRI has a transient growth, stabilized by

the growth of k_R from kinematic azimuthal shear. For the NMRI mode, we show explicitly by comparison to direct temporal integrations of the shearing sheet equations that the growth rate at $k_R = 0$ can be used to provide a good estimate of the net amplification magnitude (see §7.2.3).

(5) The coherent wavelet formalism we develop (§7.2) may be used to compute instability criteria and net amplification factors for generalized MRI disturbances with arbitrary magnetic field and wavevector orientations (§7.3). Eq. (80) gives the instantaneous dispersion relation for generalized MRIs. For strongly compressible flows ($c_s/v_A \rightarrow 0$), instability does not occur in B_ϕ -dominated configurations (cf. eq. [81a]); in this case, flows with an $\Omega \propto R^{-3/2}$ rotation law can be unstable only when the magnetic pitch angle $i > 24^\circ$. Because MHD disk winds generally have very small pitch angles, this result has the important implication that such *winds will not be subject to the development of strong internal turbulence that occurs as a consequence of nonlinear MRIs in disks*. The absence of MRIs in cold, B_ϕ -dominated winds may be crucial in enabling them to propagate over large distances from their sources. High- k_z and/or high- m modes of the generalized MRI are stabilized by MHD waves, which is a sharp contrast with the NMRI of *purely toroidal* fields in which maximum growth rates are attained at $k_z \rightarrow \infty$. For incompressible flows, the amplification factor for all MRIs can be written analytically in terms of $q_A = (\mathbf{k} \cdot \mathbf{v}_A)/\Omega$ and $\theta = \tan^{-1}(m/Rk_z)$ (eqs. [83]~[85]); within the unstable regime ($q_A < |d \ln \Omega / d \ln R|^{1/2}$, from eq. [81b]), the amplification is $\sim \exp[2\Omega/(\kappa \tan \theta)]$, favoring “locally-axisymmetric” disturbances.

8.2. Effect of Shear on Dynamical Growth of Buoyancy Instabilities

Apart from the results of §7 where we adopted the shearing sheet formulation of the dynamical equations to study MRIs, the results in this work have been elicited on the basis of the local normal mode analyses. As described in §4, these modes may have a limited range of temporal validity, due to the effects of background shear. For axisymmetric disturbances with negligible vertical shear (i.e., $m\Omega' + k_z v'_{0z} \rightarrow 0$), the results presented in §5 and §6 are acceptable for all time; the modes with pure imaginary ω will show an exponential growth without interruption over arbitrarily long time until nonlinearity sets in. However, for non-axisymmetric disturbances, or for flows with non-negligible vertical shear, unstable modes identified in §5 and §6 are not purely growing. As time evolves, the differential velocities build up the radial wavenumber through the kinematic shear (cf. eq. [40]), which in turn tends to stop the further growth of disturbances. This can be seen directly through the suppression of instabilities in the local analysis when k_R is large (cf. Fig. 8). The characteristic time for the wave pattern to change by a fraction ϵ is $t = \epsilon k_R / |m\Omega' + k_z v'_{0z}|$; over this interval, the disturbance will be amplified by a factor $\exp(\epsilon k_R \text{Im}(\tilde{\omega}) / |m\Omega' + k_z v'_{0z}|)$. When $k_R \gg m/R, k_z$, Fig. 8 shows that $\text{Im}(\tilde{\omega}) \propto k_R^{-1}$, so that the net amplification factor is nearly independent of k_R . Since, however, $\text{Im}(\tilde{\omega})$ is not larger than $\sim |m\Omega' + k_z v'_{0z}| k_R^{-1}$, only order-unity amplification can be expected for disturbances which are consistent with the requirements for quasi-steady normal mode analysis.

Because the normal-mode dispersion relations indicate larger values of growth rates when

Rk_{R}/m is small (which is however not self-consistent with the WKB treatment), it is desirable to extend investigation to allow for Rk_{R}/m small. The coherent wavelet formalism used for the MRI in §7 suggests that when $m \gg 1$ (or $Rk_z \gg 1$ for $v'_{0z} \neq 0$ cases), this can be done by regarding k_{R} as a time-dependent variable according to eq. (40) and using the asymptotic dispersion relations of §6 (i.e., eq. [43] for PB, eq. [45] for ATB, eq. [52] for NTB, and eq. [53] for GPB). To verify this argument, we specifically consider the NTB modes (which are one of the chief instabilities in B_ϕ -dominated winds) and compare the results with the shearing sheet temporal integrations. For the latter, we set $B_z = 0$ and integrate eqs. (26)~(31) in time, setting all of the coefficients to constant values. The resulting instantaneous growth rates and time evolutions of variables are plotted in Fig. 17 as functions of the normalized time $\tau = t\Omega$. We omitted the k_{R} -dependent term in eq. (26) in order to remove rapid oscillations arising from a phase mismatch between the density and radial velocity; the amplitude evolution is independent of this term. We also neglected the vertical velocity shear and selected $q = k_{\text{R}}(0) = k_z = 0$, $R\Omega = 0.1v_{\text{A}\phi}$, and $m = 100$. As initial conditions, we chose 0.1 for every variable except $b_{\text{R}} = 0.01$ and integrated the system of the linearized equations. Various curves are computed from direct numerical integrations of shearing sheet equations, while the heavy solid lines are drawn from the normal mode solution, eqs. (52) and (86) (see below), after taking allowance for the time dependence of k_{R} . The rapid fluctuations of the perturbed variables for $\tau < 0$ are due to MHD waves with high $|k_{\text{R}}|$, disappearing after variables grow substantially. Again, most of growth occurs over a relatively short period of time near $k_{\text{R}} \sim 0$. Note an excellent agreement between the results from two different approaches; we have also obtained similar results with integration from other initial conditions. This confirms that our normal mode results can also be applied to high- m disturbances if k_{R} is allowed to vary with time.

Using eq. (52) with $k_{\text{R}}(t)$ from eq. (40), we integrate $\tilde{\omega}$ over time to estimate the net amplification for the NTB modes

$$\frac{\chi_1(t)}{\chi_1(0)} = \exp \int_0^t \text{Im}(\tilde{\omega}) dt = \left[\frac{3}{2}\Omega t + \sqrt{1 + \left(\frac{3}{2}\Omega t\right)^2} \right]^{(1-q)v_{\text{A}\phi}/3R\Omega}, \quad (86)$$

where we put $v'_{0z} = k_{\text{R}}(0) = 0$ and assume a Keplerian rotation. Thus instead of an exponential growth, at later time of evolution we have the power-law growth due to the kinematic shear. This behavior is distinct from the MRI modes, which are strictly stable for large enough k_{R} . However, the continued local growth of buoyancy perturbations is offset by the role of kinematic shear in mixing phases of disturbances. Considering waves on $z=\text{constant}$ plane in a square with sides L , the maximum averaged contrast in any variable relative to the mean value is $(\lambda/L)\chi_1(t)$, where λ is the local wavenumber of the waves. With $\lambda \sim k_{\text{R}}(t)^{-1}$ and using eqs. (6) and (86), the average contrast for the NTB modes evolve with time as $\sim (\Omega t)\sqrt{2^{(1-q)/3}-1}$, vanishing as $t \rightarrow \infty$ for $0 < q < 1$. From eq. (86), amplification factors are essentially scale-free. Although there may be a significant growth of the NTB modes on large scales, their dynamical effect on small scales is limited by the phase mixing due to shear.

In the presence of vertical shear, the evolution of ATB modes is also affected by the kinematic growth of k_R although they are axisymmetric modes. The net amplification of the ATB modes follows a power-law growth as that of the NTB mods does. In fact, eq. (86) with Ω replaced by $2v'_{0z}/3$ gives the temporal behavior of the net amplification for the ATB modes.

8.3. Discussion of Applications to Protostellar Winds

In order for a disk wind to overcome the gravitational barrier due to a central object and to be centrifugally launched from the surface of a Keplerian disk, the poloidal components of field lines should thread the disk at an angle of 30° or more from the axis (Blandford & Payne 1982). Once material starts to flow outward along such field lines, it is accelerated primarily in the radial direction by the centrifugal force or by the pressure gradient in the toroidal field. Beyond the Alfvén surface where the local, poloidal component of the flow velocity is equal to that of the Alfvén wave velocity, the magnetic field is not strong enough to play a role of “a rigid wire”, and the inertia of gas becomes important, winding up the field lines to be progressively more toroidal. In this process, the azimuthal flow velocity decreases below the corotation value. With the increase in the azimuthal component of the magnetic field, the associated hoop stress provides the collimation of the outflow and causes the streamlines to bend upward. The radial flow velocity of the outflow is still positive, although it decreases gradually, eventually becoming zero at the cylindrical asymptotic limit. The power-law solutions (with $v_R = B_R = 0$) we adopted for many specific cases represent the asymptotic limit of each streamline.

Ostriker (1997) presented self-similar steady solutions for disk winds with cylindrical asymptotics and gave the asymptotic fluid and Alfvén speeds and the location of the asymptotic streamlines, characterized by q together with R_A/R_1 or R_0/R_1 , where R_0 , R_A , and R_1 denote the radii of the footpoint, the Alfvén surface, and the asymptote of each given streamline, respectively. Typical numerical values for those solutions are $\Omega = 0.2\Omega_0$, $v_{A\phi}/R = 0.42\Omega_0$, and $v_{A\phi}/v_z = 6$ for $q = 0.5$, and $\Omega = 0.1\Omega_0$ and $v_{A\phi}/R = 0.45\Omega_0$ for $q = 0.9$, where Ω_0 is the Keplerian rotation rate at the streamline footpoint.

Using these values we can estimate the growth times of the global fundamental mode and the fastest growing (with k_R near 0) toroidal buoyancy modes. The foregoing analysis suggests that these disturbances will play the most significant dynamical role, given the ineffectiveness of MRIs in cold, B_ϕ -dominated flows. We define the time to grow by Γ orders of magnitude as t_Γ . For FM, $t_{\Gamma,FM} = \Gamma/(|\omega| \log e)$, so from Fig. 2 and eq. (25) we have for $q = 0.9$

$$t_{\Gamma,FM} \sim \frac{14\Gamma}{\Omega_{0,i}} = 25 \Gamma \text{ days} \left(\frac{M}{M_\odot} \right)^{-1/2} \left(\frac{R_{0,i}}{0.1 \text{ AU}} \right)^{3/2}.$$

For ATB and NTB, from eqs. (45) and (52), we have for $i \rightarrow 0$ and $q = 0.5$

$$t_{\Gamma,ATB} \sim \frac{10^\Gamma}{0.21\Omega_0} = 24 \times 10^\Gamma \text{ yrs} \left(\frac{M}{M_\odot} \right)^{-1/2} \left(\frac{R_0}{10 \text{ AU}} \right)^{3/2} \quad \text{and}$$

$$t_{\Gamma, \text{NTB}} \sim \frac{10^{1.4\Gamma}}{3\Omega_0} = 1.7 \times 10^{1.4\Gamma} \text{ yrs} \left(\frac{M}{M_\odot} \right)^{-1/2} \left(\frac{R_0}{10 \text{ AU}} \right)^{3/2},$$

respectively. Here, M is the mass of the central star and $\Omega_{0,i}$ is the angular speed of a disk at the footpoint $R_{0,i}$ of the innermost streamline of winds. The fact that the growth of the FM by a factor 10^Γ occurs within $\sim \Gamma$ times the rotation period of the disk at the inner radius, far shorter than the lifetime of winds ($\sim 10^4 - 10^5$ yrs), suggests that the FM mode is dynamically important in the evolution of the disk winds. When q is small, the radial turbulent mixing of the wind, caused by both axisymmetric and non-axisymmetric toroidal buoyancy modes over a relatively short time, is likely to cascade down into arbitrarily smaller scales to dissipate when the microscopic processes such as magnetic reconnection are included. The released energy in the dissipation processes may heat up the flow, potentially making a significant contribution to the heating of protostellar winds and jets. Because the growth rates of buoyancy modes are proportional to the equilibrium magnetic forces (cf. eqs. [45] and [52]), winds that have approached a force-free magnetic configuration will not be subject to the ATB and NTB instabilities.

The global fundamental mode affects only the inner region of the disk winds (e.g., the central tenth for the model shown in Fig. 3). The logarithmic density gradient $\partial \ln \rho / \partial \ln R$ changes relative to the equilibrium value by $\partial(\rho_1/\rho_0)/\partial \ln R$. Fig. 3 shows that as a consequence of the fundamental mode, the very central region becomes more steeply stratified, a surrounding concentric region less steeply stratified, and the balance (most of the wind) remains nearly unchanged. Thus, the FM tends to enhance jetlike structure in the central parts of winds. In addition, because of their tendency to compress interior gas via the FM mechanism, disk winds may help to collimate any interior flows into narrow, fast jets, even when the disk winds themselves have relatively slow motion (cf. Ostriker 1997).

What do the present results imply about the likely radial extent of protostellar winds? First, we note that observed optical jets are unlikely to be isolated structures, because if so they would be significantly overpressured relative to the ambient medium: Since magnetocentrifugal jet models typically predict internal Alfvén speeds comparable to their flow speeds in the range $150 \sim 400 \text{ km s}^{-1}$, they have strong internal magnetic pressure $P_{\text{wind}} = B_\phi^2/8\pi \sim \rho_w v_A^2/2 \sim 2.8 \times 10^{-7} \text{ ergs cm}^{-3}$, which is about 6 orders of magnitude greater than the gas pressure of ambient medium, $P_{\text{ext}} = c_s^2 \rho_{\text{ext}} \sim 1.3 \times 10^{-13} \text{ ergs cm}^{-3}$. Here as reference values we adopted $\rho_w = 350 m_{\text{H}} \text{ cm}^{-3}$, $\rho_{\text{ext}} = 200 m_{\text{H}} \text{ cm}^{-3}$, $v_A = 310 \text{ km s}^{-1}$, and $c_s = 0.2 \text{ km s}^{-1}$ with m_{H} being the mass of a hydrogen atom (Hartigan et al. 1999). Thus the pressure imbalance at the outer boundary of the jet would cause either the wind as a whole or only its surface layer to expand until a new balance is attained. Based on the results of this paper, if the magnetic field at the base of the wind is stratified less steeply than R^{-1} , then perturbations of the outer parts of the wind are stable. As a consequence, only the surface layers of such winds would expand in order to achieve a pressure-balanced condition with the ambient medium. If, on the other hand, the wind’s magnetic field is stratified more steeply than R^{-1} at its base, no equilibrium is even possible; the wind would expand as a whole to fill the entire 4π steradians, with the inner parts having higher density observable as a narrow optical

jet (cf. Shu et al. 1994; Shang et al. 1998). Numerical simulations presently underway (Lee et al. 2000) support previous work indicating that protostellar winds with a wide-angle component are better able to produce observed molecular outflow structures than purely jetlike winds (see also Li & Shu 1996; Ostriker 1997, 1998; Matzner & McKee 1999) but further studies are required to determine just how distributed in angle the wind momentum should be - i.e., to discriminate between “fully-expanded” and “surface-expanded” models. Recent observations (see, e.g., Richer et al. 2000) showing a correlation in molecular outflow kinematics with age - with extremely high velocity, highly-collimated flows seen only in the youngest sources - may indicate an underlying temporal evolution from more-collimated to more-expanded protostellar winds.

We acknowledge a stimulating report from an anonymous referee, and helpful comments from N. Turner and S. Balbus.

REFERENCES

- Abramowitz, M., & Stegun, I. A. 1965, *Handbook of Mathematical Functions* (New York: Dover)
- Appert, K., Gruber, R., & Vaclavik, J. 1974, *Phys. Fluids*, 17, 1471
- Appl, S., & Camenzind, M. 1992, *A&A*, 256, 354
- Bachiller, R. 1996, *ARAA*, 34, 111
- Balbus, S. A., & Hawley, J. F. 1991, *ApJ*, 376, 214
- Balbus, S. A., & Hawley, J. F. 1992, *ApJ*, 400, 610
- Balbus, S. A., & Hawley, J. F. 1998, *Rev. Mod. Phys.*, 70, 1
- Blaes, O. M., & Balbus, S. A. 1994, *ApJ*, 421, 163
- Blandford, R. D., & Payne, D. G. 1982, *MNRAS*, 199, 883
- Chandrasekhar, S. 1960, *Proc. Natl. Acad. Sci.*, 46, 253
- Curry, C., & Pudritz, R. E. 1996, *MNRAS*, 281, 119
- Dubrulle, B., & Knobloch, E. 1993, *A&A*, 274, 667
- Foglizzo, T., & Tagger, M. 1995, *A&A*, 301, 293
- Goldreich, P., & Lynden-Bell, D. 1965, *MNRAS*, 130, 125
- Hardee, P. E., Cooper, M. A., Norman, M. L., & Stone, J. M. 1992, *ApJ*, 399, 478
- Hartigan, P., Morse, J. A., Tumlinson, J., Raymond, J., & Heathcote, S. 1999, *ApJ*, 512, 901

- Hartigan, P., Bally, J., Reipurth, B., and Morse, J. A. 2000, in *Protostars and Planets IV*, ed. V. Mannings, A. P. Boss, & S. S. Russell (Tucson: University of Arizona Press), in press
- Hartmann, L., & MacGregor, K. B. 1982, *ApJ*, 259, 180
- Hawley, J. F., & Balbus, S. A. 1991, *ApJ*, 376, 223
- Hawley, J. F., Gammie, C. F., & Balbus, S. A. 1995, *ApJ*, 440, 742
- Julian, W. H., & Toomre, A. 1966, *ApJ*, 146, 810
- Königl, A., & Pudritz, R. E. 2000, in *Protostars and Planets IV*, ed. V. Mannings, A. P. Boss, & S. S. Russell (Tucson: University of Arizona Press), in press
- Lada, C. J. 1985, *ARAA*, 23, 267
- Li, Z. Y., & Shu, F. H. 1996, *ApJ*, 472, 211
- Lee, C. F., Stone, J. M., Ostriker, E. C., & Mundy, L. G. 2000, in preparation
- Lin, D. C. N., Papaloizou, J. C. B., & Kley, W. 1993, *ApJ*, 416, 689
- Matzner, C. D., & McKee, C. F. 1999, *ApJ*, 526, 109
- Miller, K. A., & Stone, J. H. 1999, *ApJ*, submitted
- Morse, P. M., & Feshbach, H. 1953, *Methods of Theoretical Physics* (New York: McGraw-Hill) pp 719-725
- Nagar, N. M., Vogel, S. N., Stone, J. M., & Ostriker, E. C. 1997, *ApJ*, 482, L195
- Norman, C., & Silk, J. 1980, *ApJ*, 238, 158
- Ostriker, E. C. 1997, *ApJ*, 486, 291
- Ostriker, E. C. 1998, in *Accretion Processes in Astrophysical Systems*, ed. S. Holt, & T. Kallman (Woodbury NY:AIP press) p484
- Ouyed, R., & Pudritz, R. E. 1997, *ApJ*, 484, 794
- Parker, E. N. 1966, *ApJ*, 145, 811
- Pudritz, R. E., & Norman, C. A. 1986, *ApJ*, 301, 571
- Rae, I. C., & Roberts, B. 1982, *MNRAS*, 201, 1171
- Richer, J. S., Shepherd, D. S., Cabrit, S., Bachiller, R., and Churchwell, E. 2000, in *Protostars and Planets IV*, ed. V. Mannings, A. P. Boss, & S. S. Russell (Tucson: University of Arizona Press), in press

- Reipurth, B., Bally, J., & Devine, D. 1997, *AJ*, 114, 2708
- Roberts, B. 1985, in *Solar System Magnetic Fields*, ed. E. R. Priest (Dordrecht: D. Reidel Publishing Company) p37
- Rosen, A., Hardee, P. E., Clarke, D. A., Johnson, A. 1999, *ApJ*, 510, 136
- Ross, D. W., Chen, G. L., & Mahajan, S. M. 1982, *Phys. Fluids*, 25, 652
- Ryu, D., & Goodman, J. 1992, *ApJ*, 388, 438
- Shang, E., Shu, F. H., & Glassgold, A. E. 1998, *ApJ*, 493, L91
- Shu, F. H. 1974, *A&A*, 33, 55
- Shu, F. H. 1992, *The Physics of Astrophysics. II. Gas Dynamics* (Mill Valley: Univ. Science Books)
- Shu, F. H., Adams, F. C., & Lizano, S. 1987, *ARAA*, 25, 23
- Shu, F. H., Lizano, S., Ruden, S., & Najita, J.. 1988, *ApJ*, 328, L19
- Shu, F. H., Najita, J. R., Ostriker, E. C., Wilkin, F., Ruden, S., & Lizano, S. 1994, *ApJ*, 429, 781
- Shu, F. H., Najita, J. R., Shang, H., & Li, Z. Y. 2000, in *Protostars and Planets IV*, ed. V. Mannings, A. P. Boss, & S. S. Russell (Tucson: University of Arizona Press), in press
- Stone, J. M., Gammie, C. F., Balbus, S. A., & Hawley, J. F. 2000, in *Protostars and Planets IV*, ed. V. Mannings, A. P. Boss, & S. S. Russell (Tucson: University of Arizona Press), in press
- Terquem, C., & Papaloizou, J. C. B. 1996, *MNRAS*, 279, 767
- Velikhov, E. 1959, *Sov. Phys.-JETP*, 36, 995

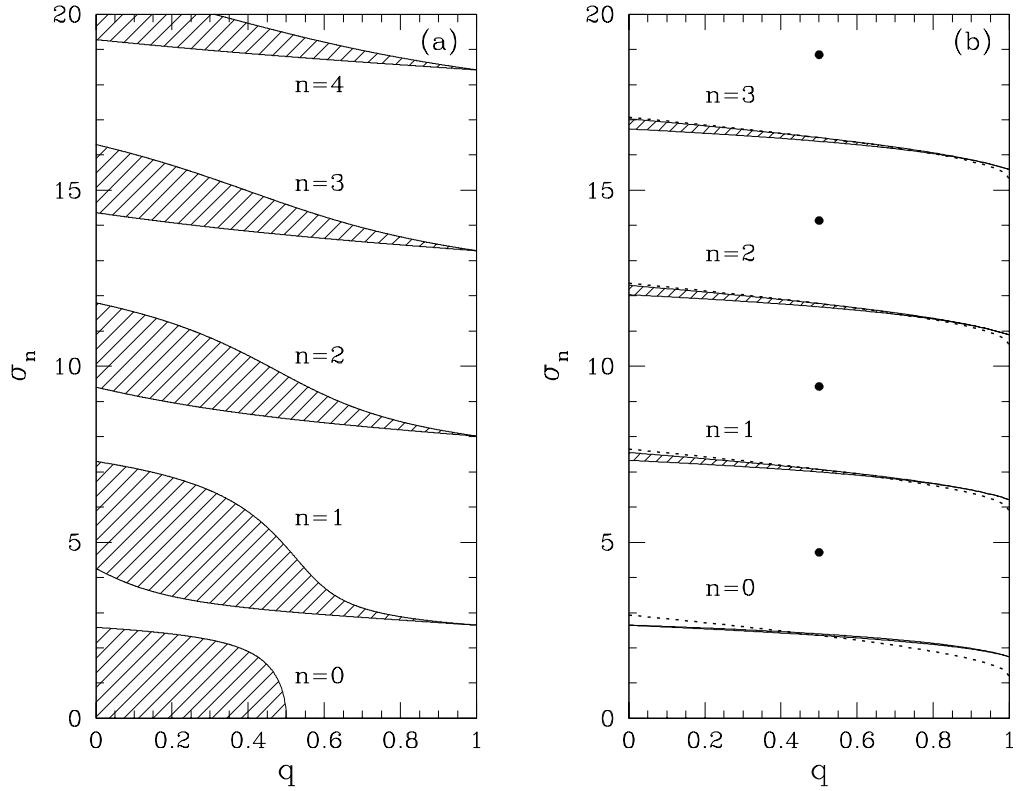


Fig. 1.— Eigenvalues $\sigma = \omega R_e / v_A(R_e)$ of stable global fundamental modes for (a) $r_i = 0.1$ and (b) $r_i = 10^{-4}$ are plotted as functions of q (R_e is the radius of the outer boundary, R_i is the radius of the inner boundary, and $r_i \equiv R_i / R_e$). Each shaded envelope is filled with eigenfrequencies having the same n but different $i < i_{\max}$. Since i_{\max} is a decreasing function of q , having $i_{\max} = 0$ when $q = 1$, the envelopes narrow in width as q increases. Eigenvalues with $r_i = 0.1$ are more sensitive to q and i than those with $r_i = 10^{-4}$. Mode conversion (see text) occurs when a cylindrical wind has a narrow thickness (r_i near 1). Dotted lines in (b) represent asymptotic eigenvalues with $r_i \ll 1$, which are in good agreement with numerical solutions. Also shown are the eigenvalues for the case with $q = 0.5$ and $i = 0^\circ$ as filled circles. The upper boundary of each envelope corresponds to $i = 0^\circ$.

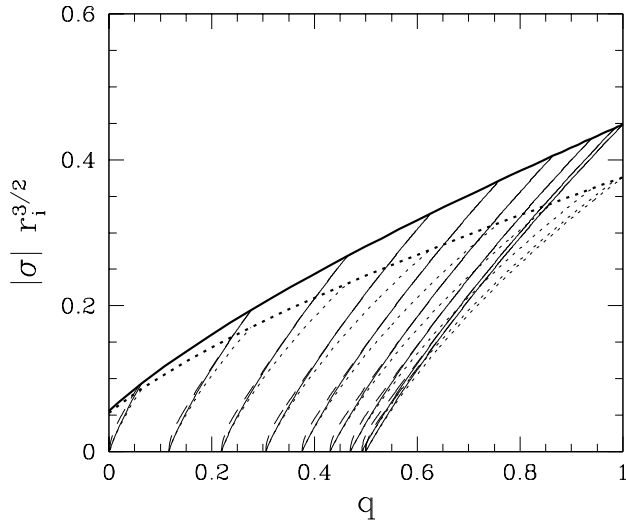


Fig. 2.— Eigenvalues $|\sigma| r_i^{3/2} = |\omega| R_i / v_A(R_i)$ of unstable global fundamental modes. Solid lines ($r_i = 10^{-4}$) and dashed lines ($r_i = 10^{-1}$) are the exact results computed from eqs. (20b) and (22). Drawn as dotted lines, the approximate, analytic solutions (eq. [25]) follow the exact values fairly well when $|\sigma|$ is relatively small. The various curves represent different pitch angles of the equilibrium magnetic field configuration: $i = 0^\circ, 5^\circ, \dots, 35^\circ, 40^\circ$ from right to left. The uppermost thick lines correspond to the maximum pitch angle, i_{\max} . Note that $|\sigma| r_i^{3/2}$ is almost independent of r_i .

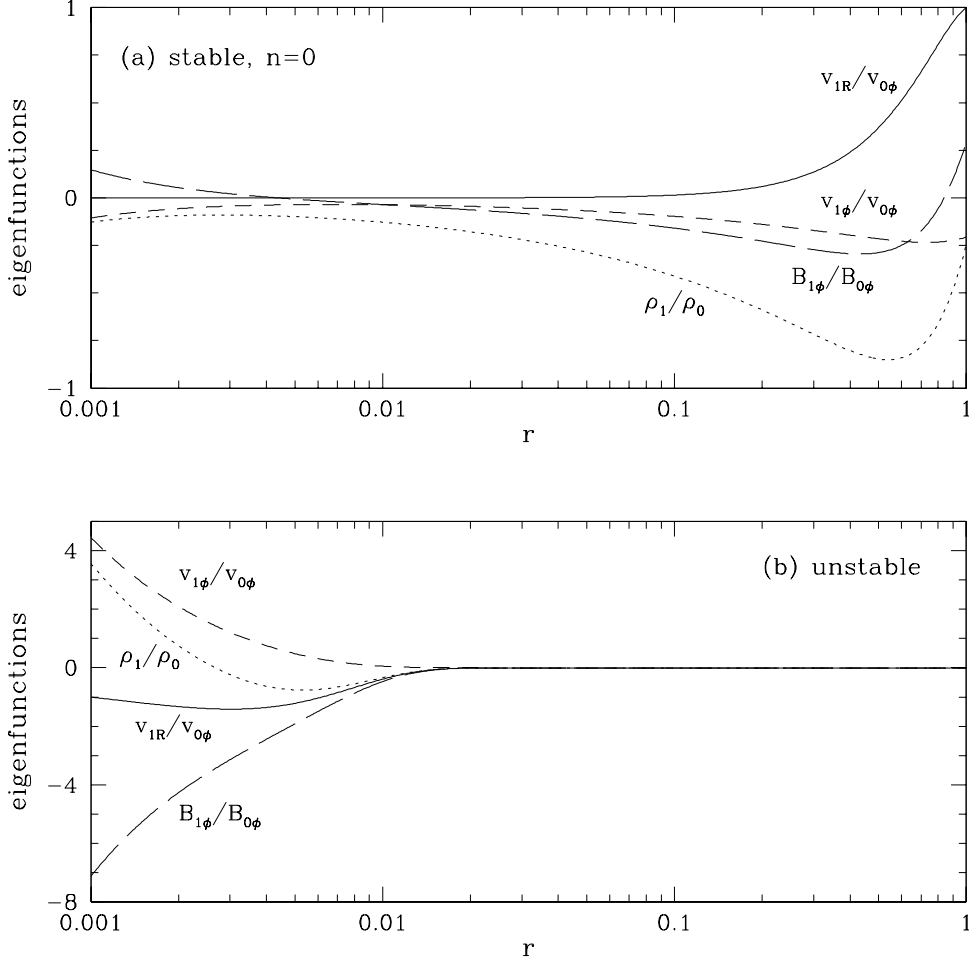


Fig. 3.— Examples of normalized (a) stable and (b) unstable fundamental modes with $i = 0^\circ$ and $r_i = 10^{-3}$. We choose $q = 0.4$, $\sigma_0 = 2.42$, and $v_{1R}/v_{0\phi} = 1$ at $r = 1$ for the stable modes, and $q = 0.6$, $|\sigma|r_i^{3/2} = 0.11$, $v_{1R}/v_{0\phi} = -1$ at $r = r_i$ for the unstable modes. Stable eigenfunctions dominate the outer region, while unstable ones affect only the inner part of the system.

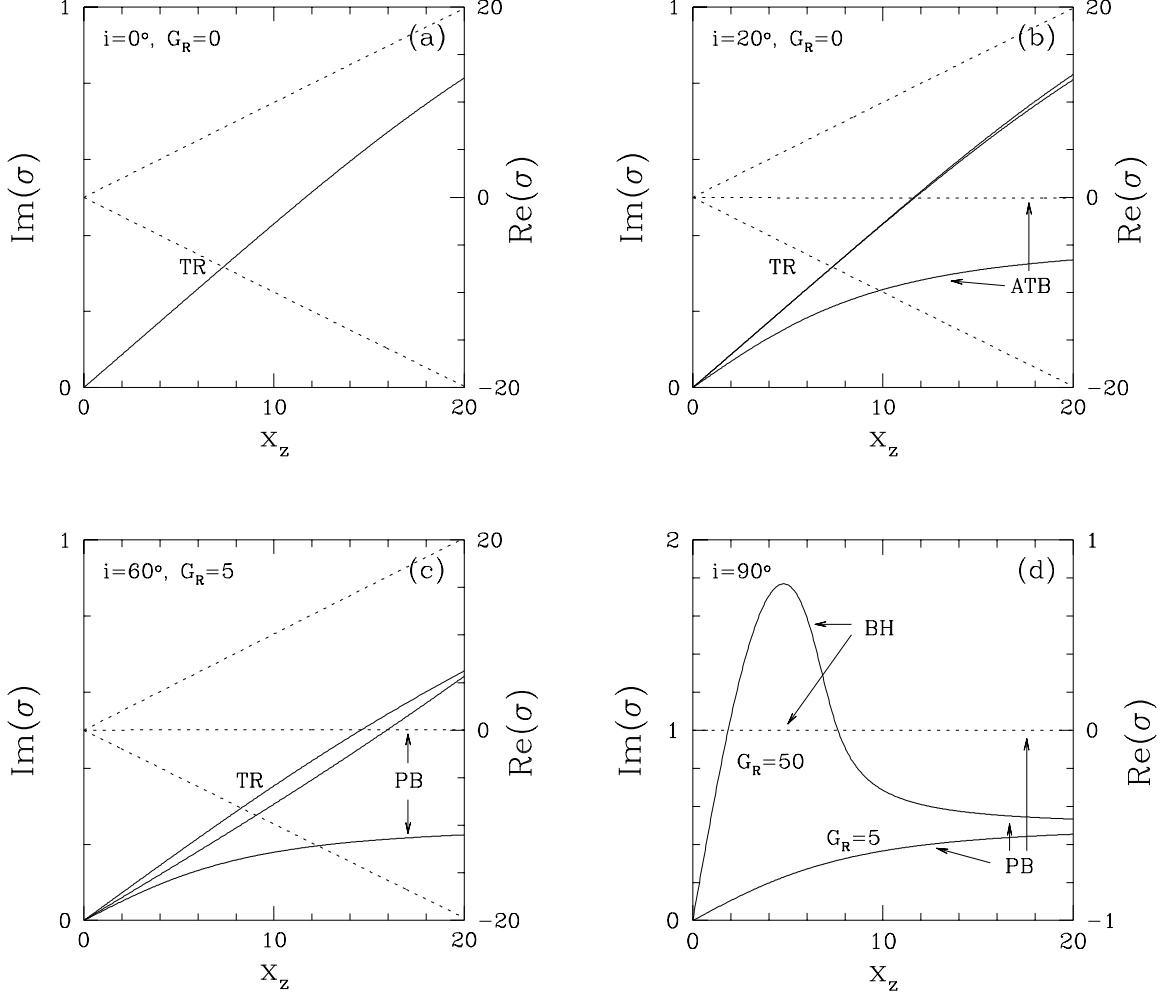


Fig. 4.— Normalized frequencies $\sigma \equiv \tilde{\omega}R_o/v_A(R_o)$ of unstable and overstable modes of axisymmetric perturbations are plotted against the normalized vertical wavenumber $x_z = k_z R_o$. For all 4 cases, $x_R = 10, q = \zeta = 0$ are adopted. In each frame, solid and dotted lines represent imaginary and real parts of the solution frequencies, respectively. (a) When $i = 0$, only the toroidal resonance mode (TR) exists, which is overstable with larger real parts. (b) and (c) The TR splits into two branches with the inclusion of poloidal fields. Axisymmetric buoyancy modes begin to appear; with relatively small i , the axisymmetric toroidal buoyancy mode (ATB) exists, whereas the poloidal buoyancy mode (PB) operates with predominant poloidal fields. (d) For a pure poloidal configuration, only BH and PB modes exist. The BH is dominant at a relatively larger wavelength region with a higher growth rate when magnetic field is weak (larger G_R).

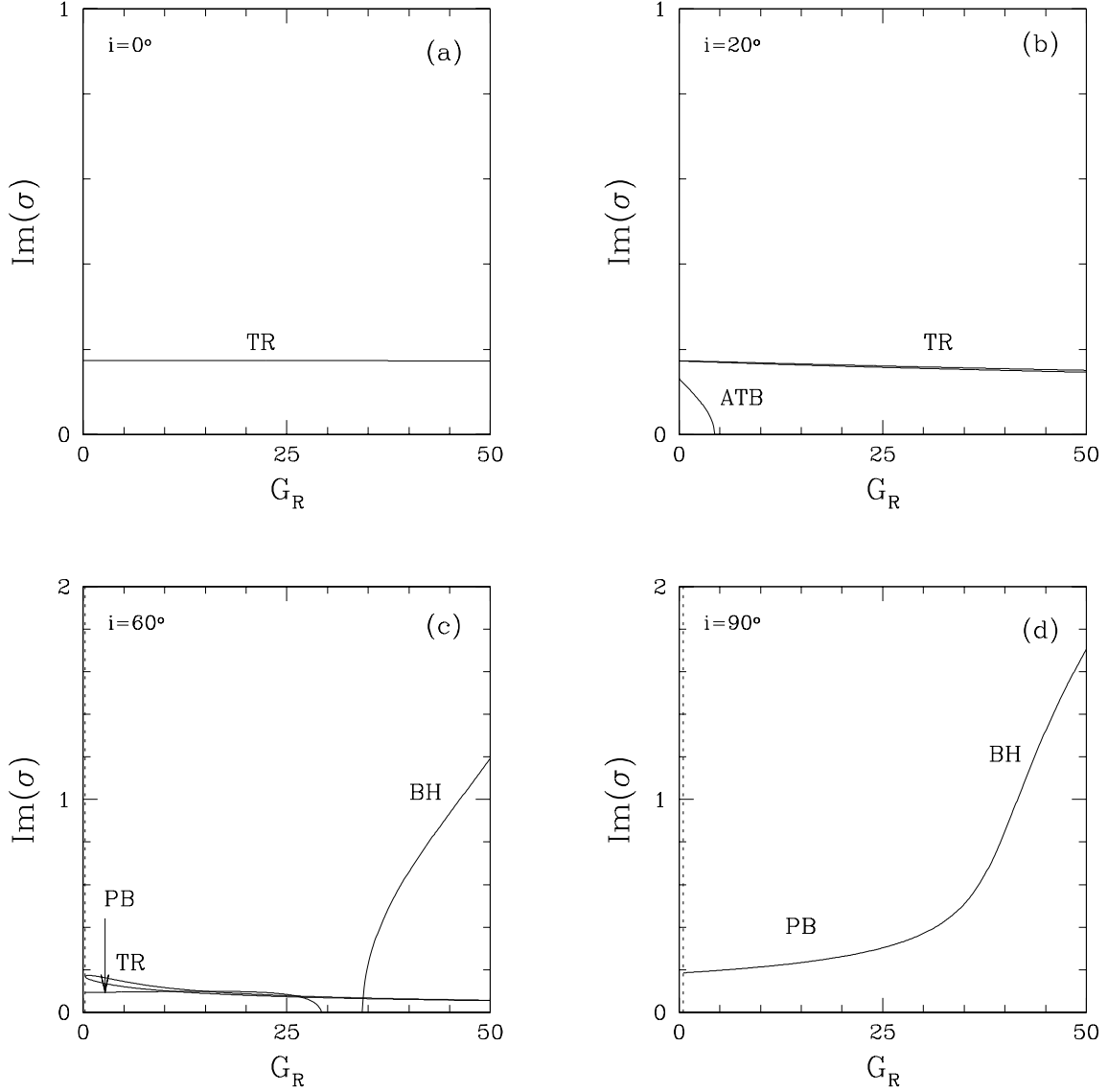


Fig. 5.— Changes of axisymmetric unstable and overstable modal growth rates with G_R and i . Normalized vertical wavenumber is fixed as $x_z \equiv k_z R_o = 4$. A rotation profile $\Omega \propto R^{-3/2}$ is assumed and $x_R = 10$, $q = \zeta = 0$ are taken. ATB and PB modes need to have smaller G_R to be unstable. Note that as G_R increases, corresponding to a weak field regime, only the BH mode prevails. Dotted lines in the frames (c) and (d) mark the minimum value of G_R , available for given q and i , below which no initial equilibrium exists. For details, see text.

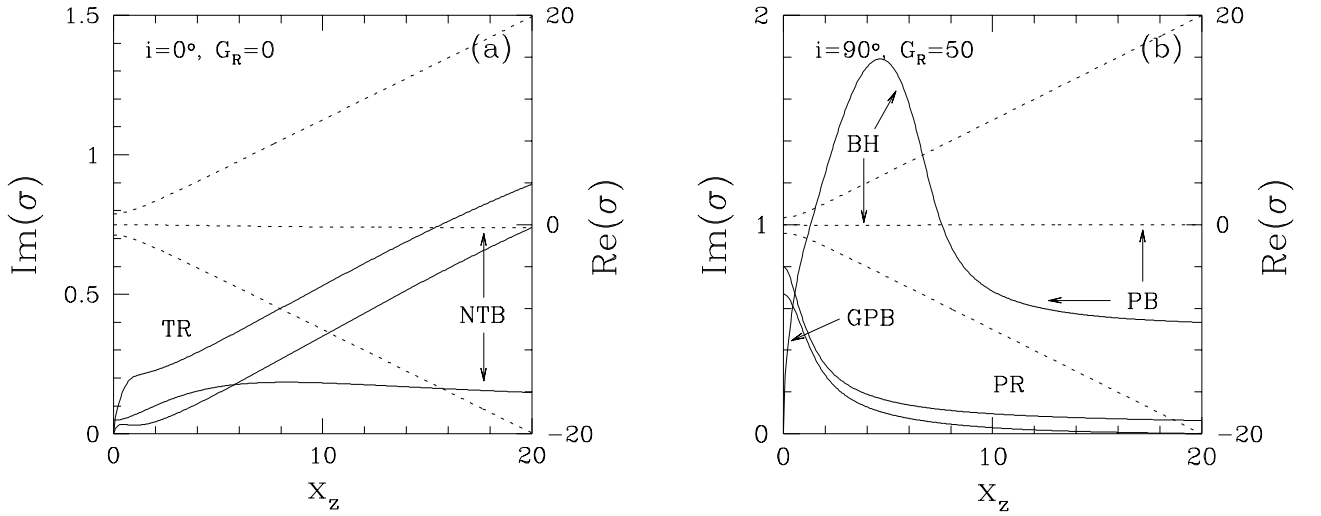


Fig. 6.— Frequencies of unstable and overstable modes for non-axisymmetric perturbations with $m = 1$ are plotted against the normalized vertical wavenumber. For both frames, $x_R = 10$, $q = \zeta = 0$ are adopted and an $\Omega \propto R^{-3/2}$ rotation profile is assumed. Solid and dotted lines represent imaginary and real parts of the normalized wave frequencies, respectively. (a) In a toroidal configuration, only TR and NTB exist, with TR being split by the non-axisymmetric effect. NTB has a nearly constant growth rate independent of x_z . Note that the real part of TR increases linearly with x_z , while that of NTB is nearly zero. (b) When i is high, GPB begins to appear. PB is almost unchanged by the non-axisymmetry. Like TR, PR is also an overstable mode with a larger real part proportional to x_z .

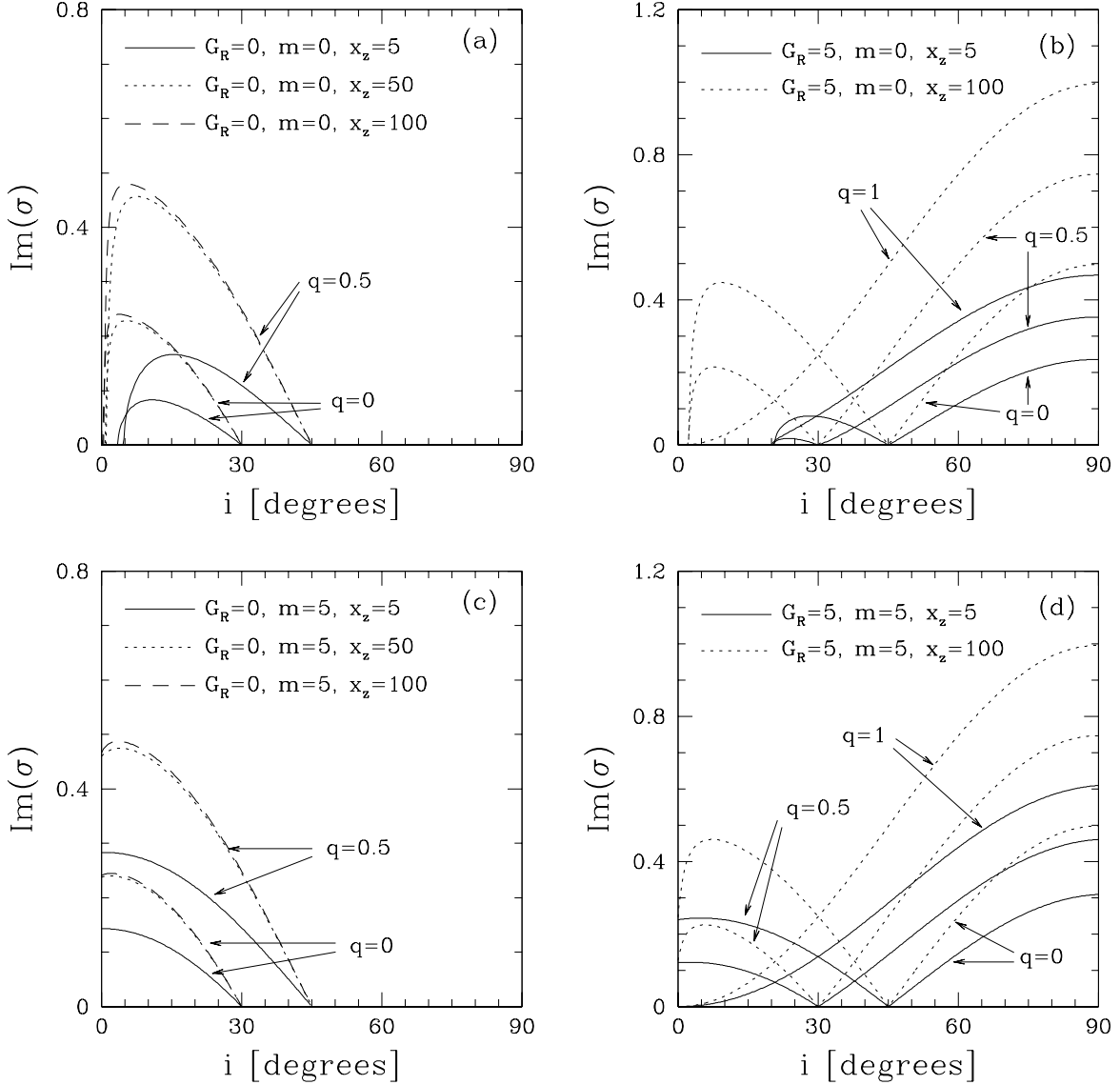


Fig. 7.— Effects of i and q on the (a and b) axisymmetric and (c and d) non-axisymmetric buoyancy mode frequencies. A rotation profile $\Omega \propto R^{-3/2}$ is assumed, and $x_R = 10$, $\zeta = 0$, and $G_R = 5$ are adopted. In all four frames, the unstable modes with $i < i_{\text{crit}} \equiv \cos^{-1} \sqrt{(1+q)/2}$ correspond to toroidal buoyancy modes, whereas poloidal buoyancy modes have $i > i_{\text{crit}}$. Note that at $i = 0$, no unstable ATB mode exists while its maximum growth rates are achieved at $i \rightarrow 0$ as $x_z \rightarrow \infty$.

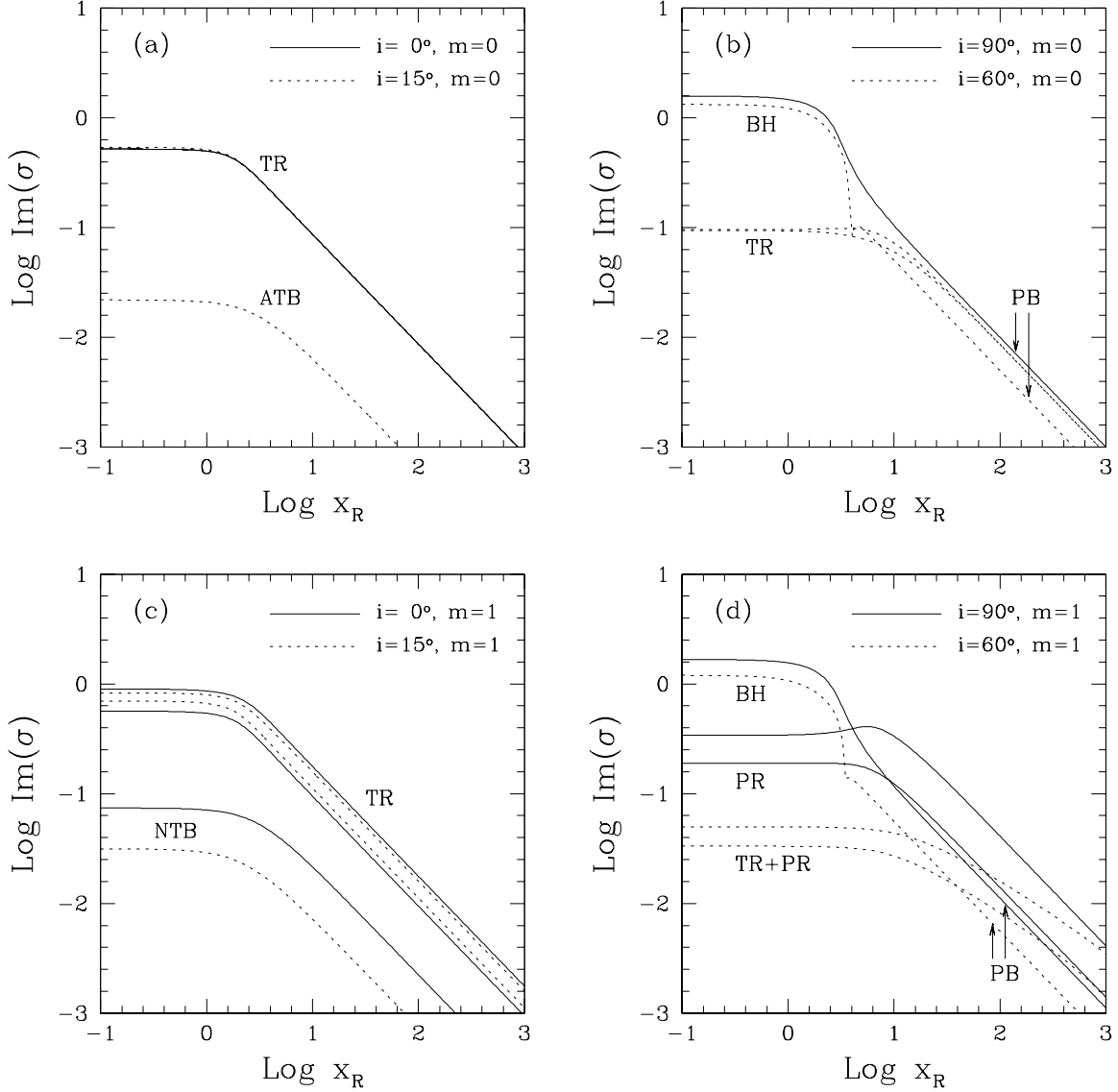


Fig. 8.— Effects of changing $k_R \equiv x_R/R_o$ on the unstable/overstable axisymmetric (a and b) and non-axisymmetric (c and d) modes. A rotation profile $\Omega \propto R^{-3/2}$ is assumed, and $x_z = 2$ and $\zeta = 0$ for all cases; $q = 0.8$, $G_R = 0$ for left frames and $q = 0$, $G_R = 5$ for right frames are adopted. BH modes cease to exist when $x_R \gtrsim 3$, but all the other modes follow $\text{Im}(\sigma) \sim x_R^{-1}$ at $x_R \gg 1$, which is in good agreement with the asymptotic dispersion relations presented in the text. Since kinematic shear causes k_R to increase linearly with time, the growth of perturbations would occur in a power-law fashion rather than an exponential one at later time of evolution.

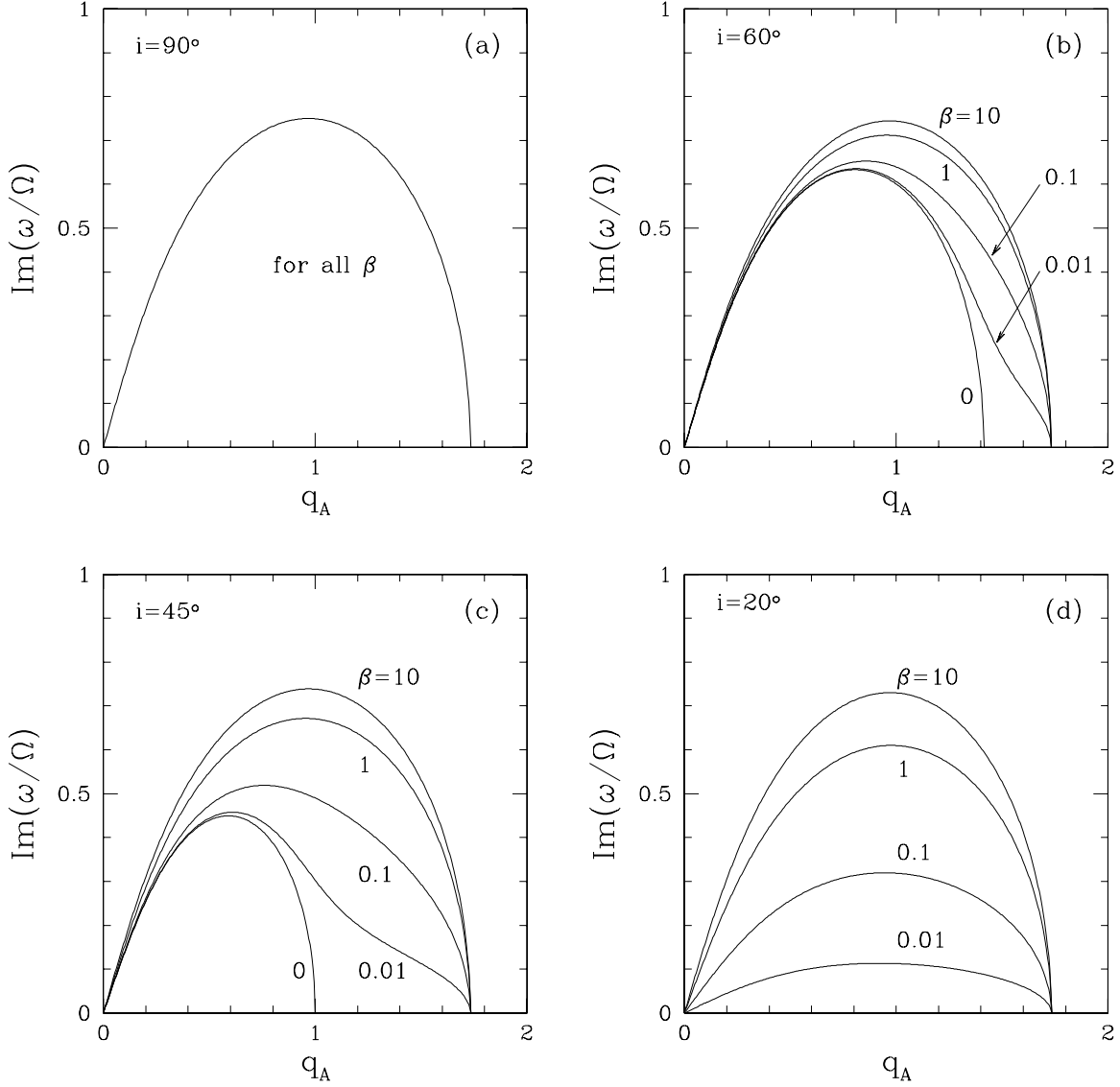


Fig. 9.— Temperature effect of the compressible BH instability. The abscissa is the normalized wavenumber $q_A \equiv (\mathbf{k} \cdot \mathbf{v}_A)/\Omega$ ($= k_z v_{Az}/\Omega$ for $m = 0$). A rotation profile $\Omega \propto R^{-3/2}$ is assumed and no radial perturbation is considered ($k_R = 0$). Curves with different $\beta \equiv c_s^2/v_A^2$ show how thermal effects modify the BH instability. For $i = 90^\circ$, the BH growth rate is independent of β , while β has a significant impact on the growth rates when $i \neq 90^\circ$. In a cold MHD limit ($\beta = 0$), no BH mode is expected if $i < 30^\circ$.

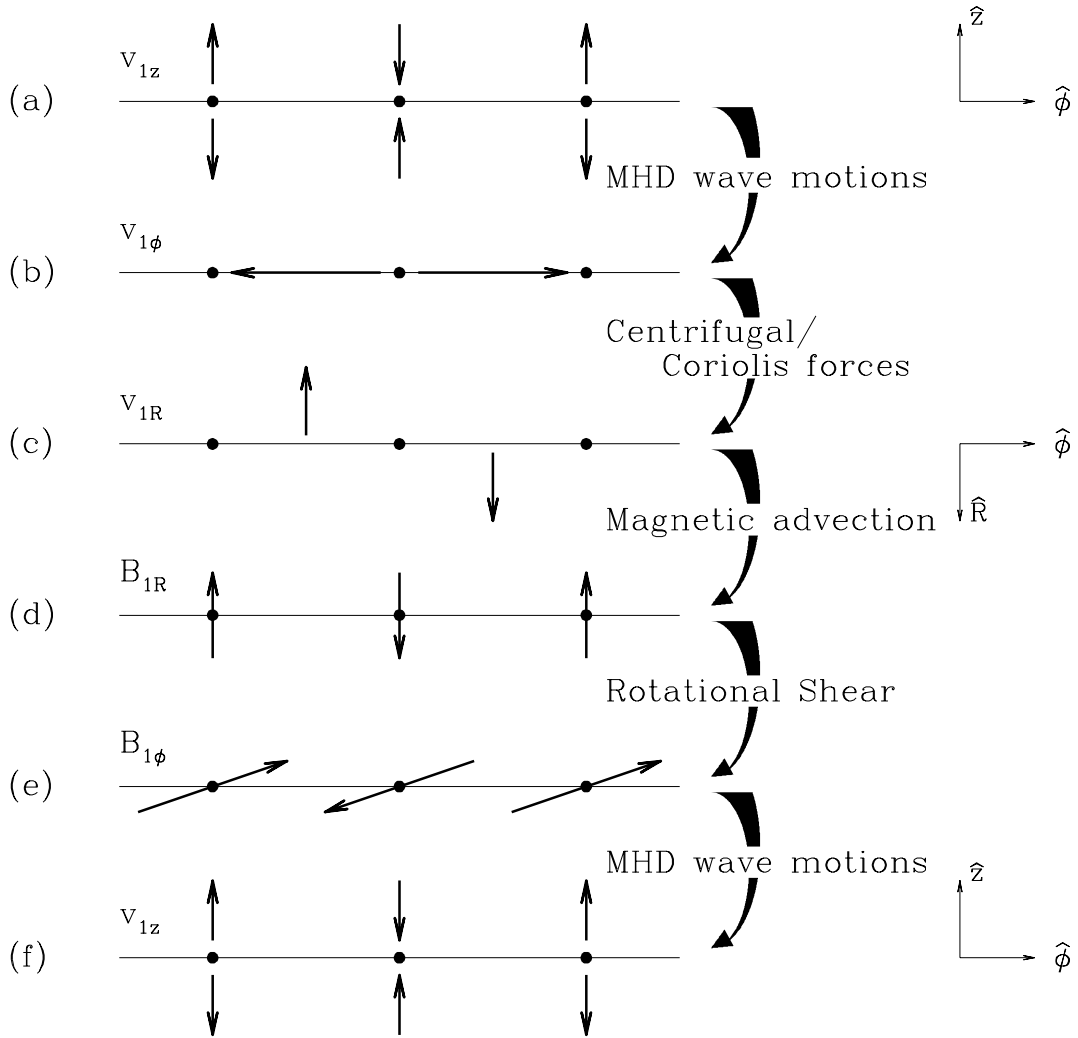


Fig. 10.— Schematic diagram showing the development of the NMRI with pure toroidal fields. Magnetic fields, thermal pressure, and differential rotation with $d\Omega/dR < 0$ all work in cooperation to amplify applied disturbances. See text for the detailed explanation.

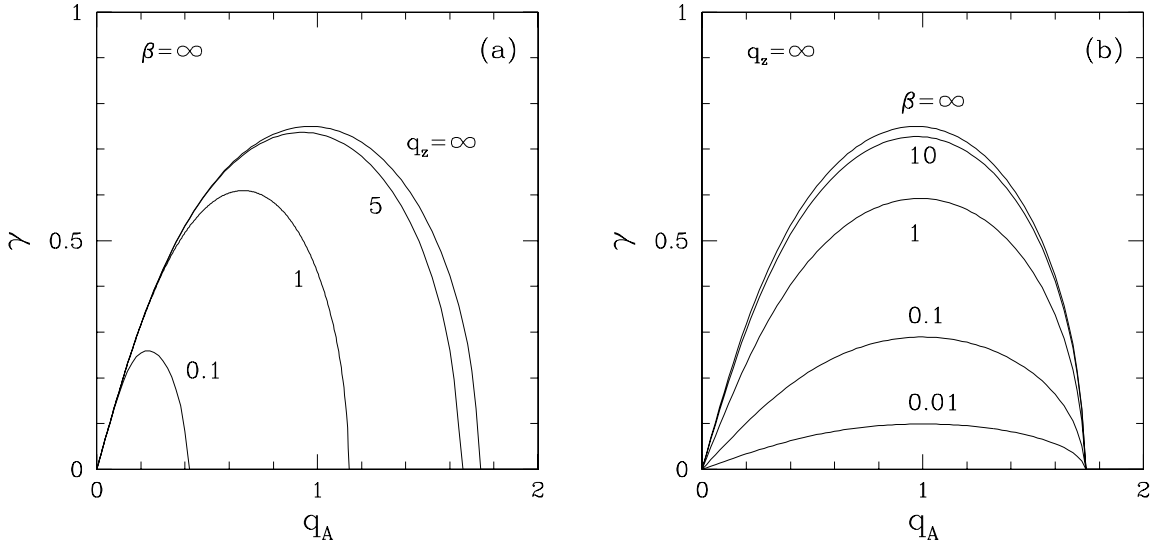


Fig. 11.— Non-axisymmetric magnetorotational instability of toroidal magnetic fields. Here, we define $q_A \equiv (\mathbf{k} \cdot \mathbf{v}_A)/\Omega$ ($= v_{A\phi} m/R\Omega \equiv q_m$ in the text for $v_{Az} = 0$), $q_z \equiv v_A k_z/\Omega$ ($= v_{A\phi} k_z/\Omega$ for $i = 0^\circ$), and $\beta \equiv c_s^2/v_{A\phi}^2$. Rotation with $\Omega \propto R^{-3/2}$ is assumed. The NMRI instability becomes more unstable with (a) higher q_z and (b) higher sound speed. The critical wavenumber q_m is independent of β , but the maximum growth rates are sensitive to temperature for $\beta \gtrsim 10$. For $q_m \ll 1$, $\gamma = q_m \sqrt{3\beta/(1+\beta)}$. Eventually at $\beta = 0$, no NMRI is expected.

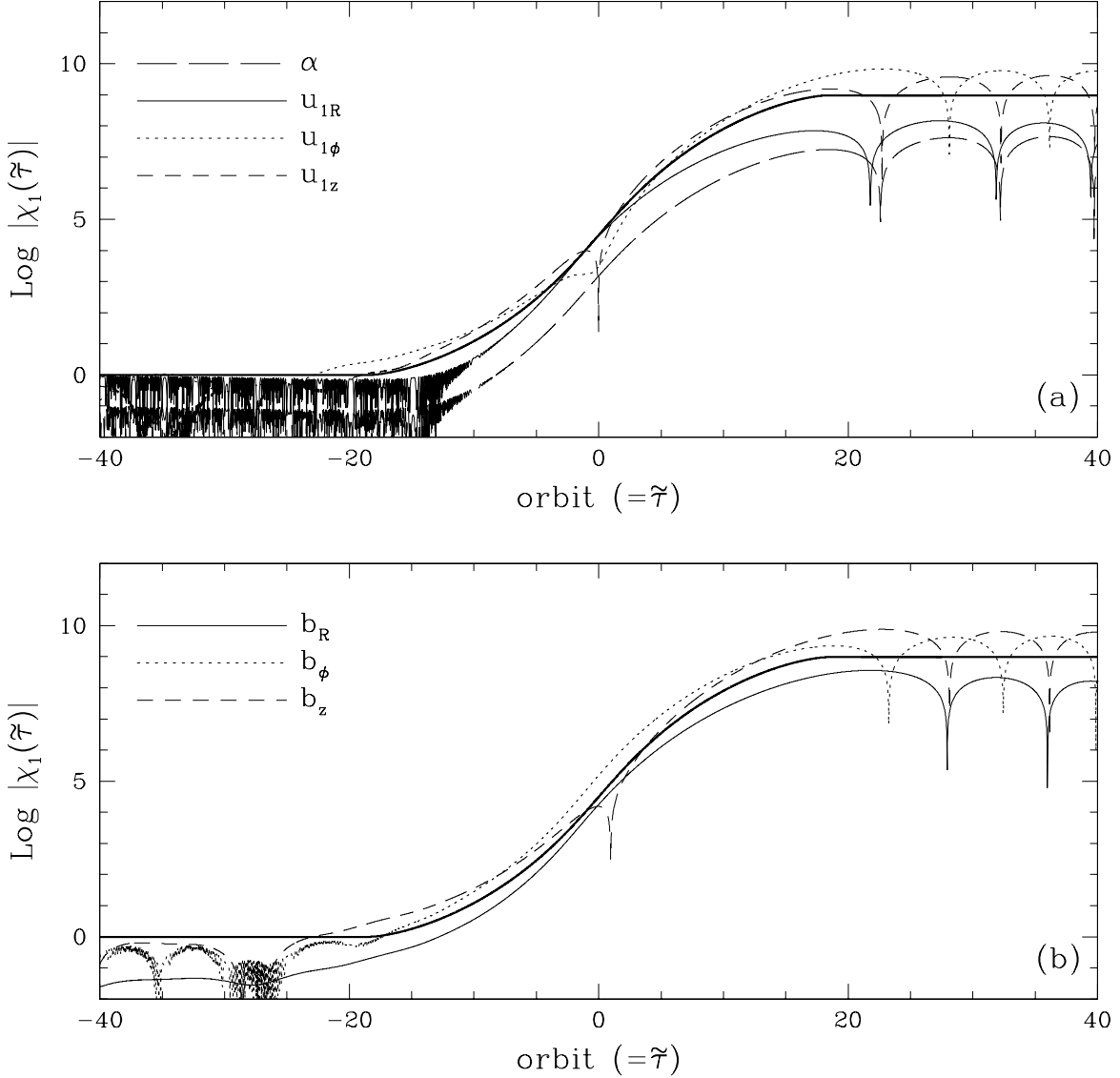


Fig. 12.— An exemplary run of the NMRI shearing sheet equations for $q_m = 0.1$, $q_z = 1$, and $\beta = 100$. We choose the initial conditions as $b_R = 0.01$, $b_z = 0.4$, and 0.1 for the other variables, and integrate the system of equations from $\tilde{\tau} = -42.44$ with which the initial perturbed magnetic field is divergence free. Overall evolution can be divided into three stages: initial relaxation phase ($\tilde{\tau} < -20$), instability phase ($|\tilde{\tau}| < 20$), and stable oscillation phase ($\tilde{\tau} > 20$). Most of growth occurs when $|\tilde{\tau}|$ is relatively small. Although kinematic growth of the radial wavenumber eventually stops the further growth of disturbances, the net amplification is tremendous. The coherent wavelet solution (eq. [76]) represented by thick solid lines in (a) and (b) is in excellent agreement with the shearing sheet results.

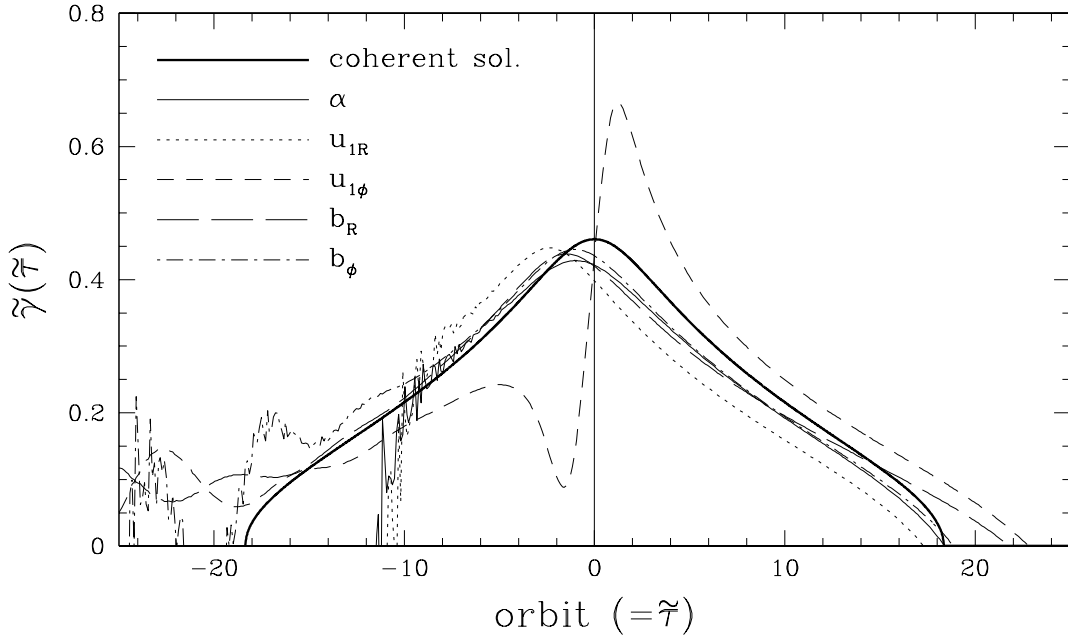


Fig. 13.— Instantaneous growth rates $\tilde{\gamma}(\tilde{\tau})$ for the NMRI with pure toroidal fields are plotted against the orbit $\tilde{\tau}$ ($\equiv t\Omega/2\pi$) for $q_m(= v_{A\phi}m/R\Omega) = 0.1$, $q_z(= v_{A\phi}k_z/\Omega) = 1$, and $\beta = 100$. The thick curve representing the coherent wavelet solution agrees fairly well with the behaviors of various curves for individual variables from the direct numerical integration of the shearing sheet equations. The NMRI shows only a temporary growth, but the net amplification is about 9 orders of magnitude in this example. Kinematic shear increases q_R with time so that eventually it suppresses the instability completely at orbit $\tilde{\tau} \simeq 18.3$. $\tilde{\gamma}(\tilde{\tau})$ is symmetric with respect to $\tilde{\tau} \sim 0$ and the coherent solution can well be fitted with eq. (77).

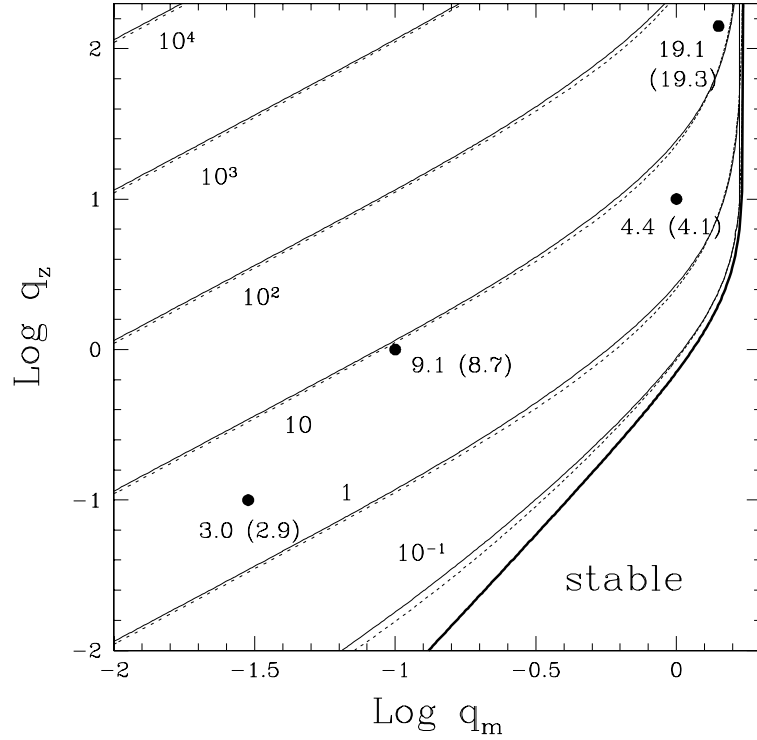


Fig. 14.— The total amplification magnitude $\Gamma(\infty)$ of the NMRI with pure toroidal magnetic fields is drawn on the $q_m - q_z$ plane. Solid contours are computed from the approximate analytic estimate, eq. (79), while dotted contours represent the results from direct numerical evaluation of eqs. (75) and (76). Four dots correspond to the results of the direct temporal integrations of the shearing sheet equations: the adapted parameters are $\beta = 100$ and $(q_m, q_z) = (0.03, 0.1)$, $(0.1, 1)$, $(1, 10)$, and $(\sqrt{2}, 100\sqrt{2})$ from lower-left to upper-right. The numbers labeling a dot is the exact and estimated (in parentheses) total amplification magnitudes. Note that the analytic estimate predicts the true amplification magnitude very closely. $\Gamma(\infty)$ has a higher value with larger q_z and smaller q_m . The heavy contour corresponds to the locus of the marginal stability.

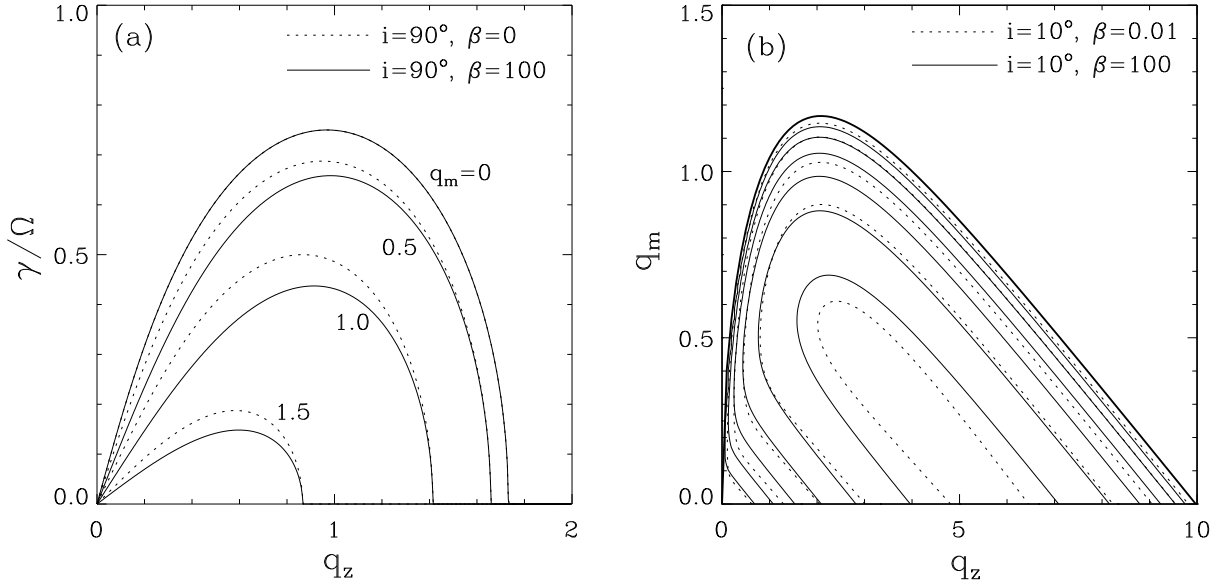


Fig. 15.— Growth rates of the generalized MRI are drawn as functions of $q_z \equiv v_A k_z/\Omega$ and $q_m \equiv v_A m/R\Omega$, (a) for $i = 90^\circ$ and (b) for $i = 10^\circ$. We put $k_R = 0$ in both frames. In frame (b), solid contours corresponding to $\beta = 100$ show $\gamma/\Omega = 0.7, 0.6, \dots, 0.2$, from inside to outside, while dotted contours corresponding to $\beta = 0.01$ show $\gamma/\Omega = 0.1, 0.08, \dots, 0.02$, from inside to outside. As q_m increases, both growth rates and unstable ranges of q_z decrease. Eventually, if $q_m > 1.73$ for $i = 90^\circ$ or $q_m > 1.17$ for $i = 10^\circ$, the generalized MRI is completely suppressed by MHD wave motions. When $i = 90^\circ$, thermal pressure tends to reduce the growth rates by activating azimuthal wave motions if $q_m \neq 0$; however, the similarity between the $\beta = 0, 100$ curves in (a) shows its effect is not significant. The uppermost thick curve in (b) represents the locus of the marginally critical wavenumbers (cf. eq. [81b]) above which no instability can be expected.

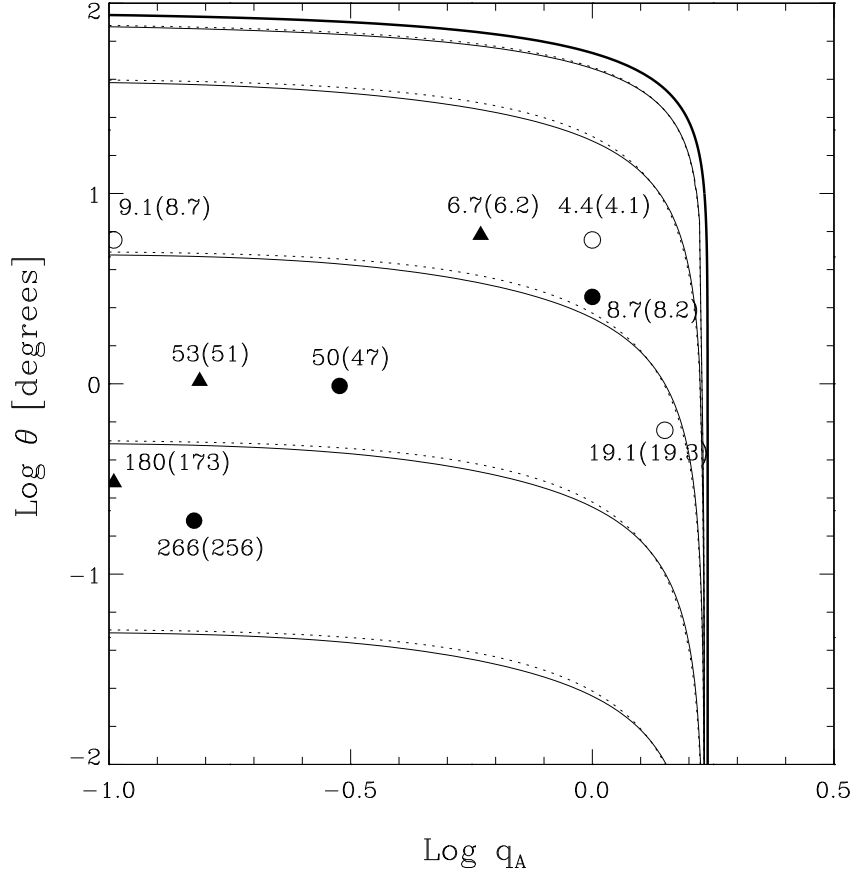


Fig. 16.— The total amplification magnitude $\Gamma(\infty)$ of the generalized incompressible MRI is drawn as a function of $q_A \equiv (\mathbf{k} \cdot \mathbf{v}_A)/\Omega$ and $\theta \equiv \tan^{-1}(m/Rk_z)$. Thin solid contours are computed from the approximate analytic estimate, eq. (83), while dotted contours represent the results from numerical evaluation of eqs. (76) and (82). Both types of contours show $\Gamma(\infty) = 10^3, 10^2, 10^1, 1, 0.1$, from bottom to top. We adopt a Keplerian rotation profile. The results of the direct temporal integrations of the shearing sheet equations with $\beta = 100$ are shown with different symbols. Open circles corresponding to $i = 0^\circ$, adopted from Fig. 14, are for $(q_m, q_z) \equiv v_A(m/R, k_z)/\Omega = (0.1, 1), (1, 10),$ and $(\sqrt{2}, 100\sqrt{2})$, filled circles corresponding to $i = 90^\circ$ for $(q_m, q_z) = (5 \times 10^{-4}, 0.15), (0.005, 0.3),$ and $(0.05, 1)$, and filled triangles with $i = 30^\circ$ for $(q_m, q_z) = (0.001, 0.2), (0.005, 0.3),$ and $(0.1, 1)$, from left to right. The numbers labeling each symbol is the exact and estimated (in parentheses) total amplification magnitudes. $\Gamma(\infty)$ has a higher value with smaller θ but nearly independent of $q_A \ll 1$. The heavy curve represents the locus of the marginal stability.

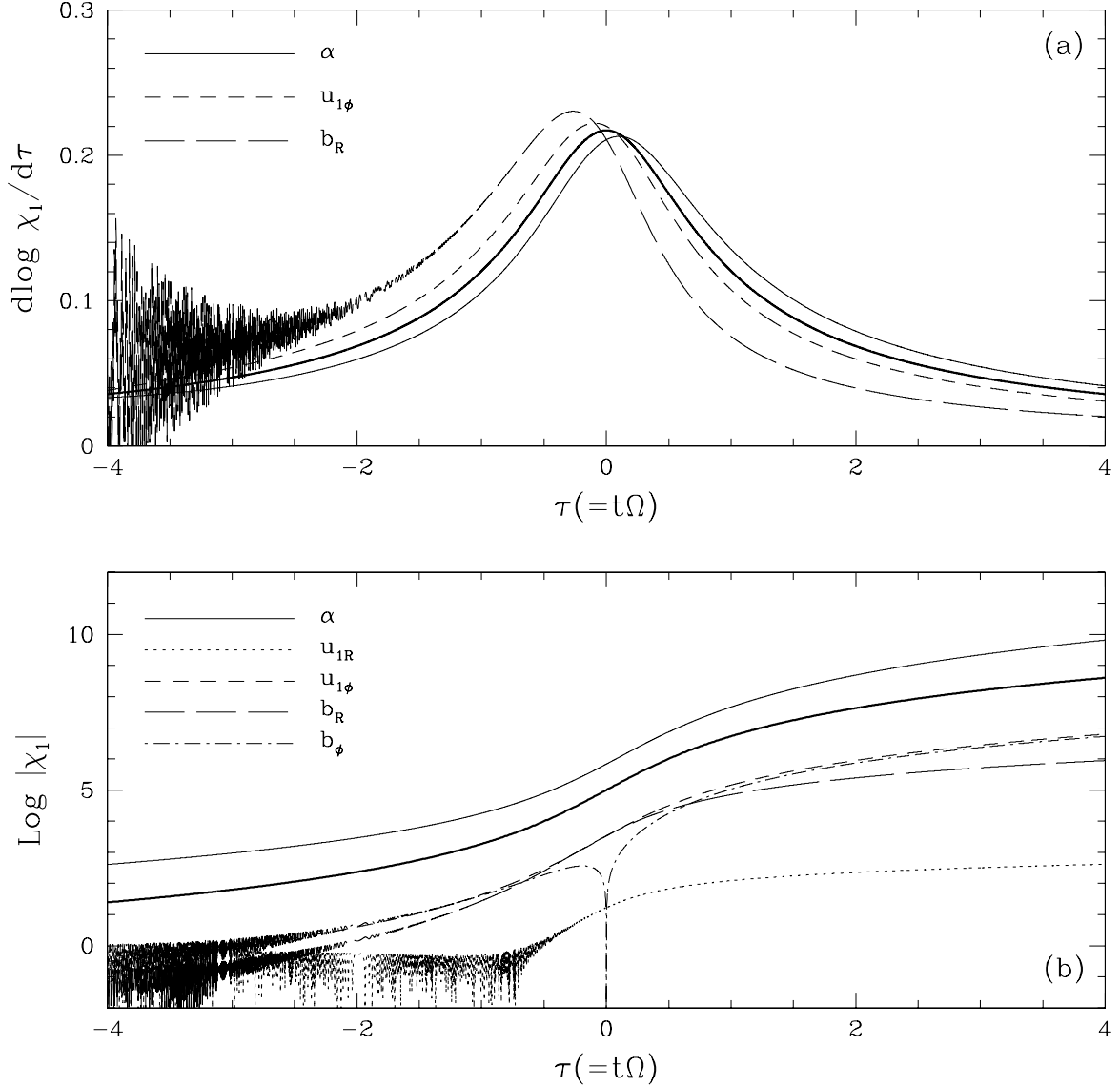


Fig. 17.— (a) Instantaneous growth rates and (b) evolutionary behaviors of physical variables are displayed for the non-axisymmetric toroidal buoyancy modes with $q = 0$, $R\Omega = 0.1v_{A\phi}$, and $m = 100$. As initial conditions, we choose 0.1 for all variables except $b_R = 0.01$. Various curves are computed from the direct temporal integrations of the shearing sheet equations. Thick solid lines, drawn from the normal mode solution, eq. (52), and its time integration, eq. (86), with $k_R(t) = -mt\Omega'$ provide excellent predictions of the numerical results. A Keplerian rotation is assumed and vertical shear is neglected. The most significant growth of the NTB modes occurs when k_R is small. With increasing k_R , the growth rate is gradually reduced. The rapid oscillations for $\tau < 0$ is due to MHD waves associated with high $|k_R|$, which are smoothed out as disturbances grow.

Table 1. Summary of the unstable/overstable mode properties.

Type	Geometry of Perturbation	Physical Mechanism	Magnetic field Configuration	Stability Character
FM	$m = k_z = 0$	global mode	toroidal	unstable
ATB		buoyancy	toroidal	unstable
PB	$m = 0$	Parker	poloidal	unstable
BH	$k_z \neq 0$	MRI	poloidal	unstable
TR		resonance	toroidal	overstable
NTB		Parker	toroidal	unstable
PR	$m \neq 0$	resonance	poloidal	overstable
GPB	$k_z \neq 0$	geometric	poloidal	unstable
NMRI		MRI	toroidal	unstable